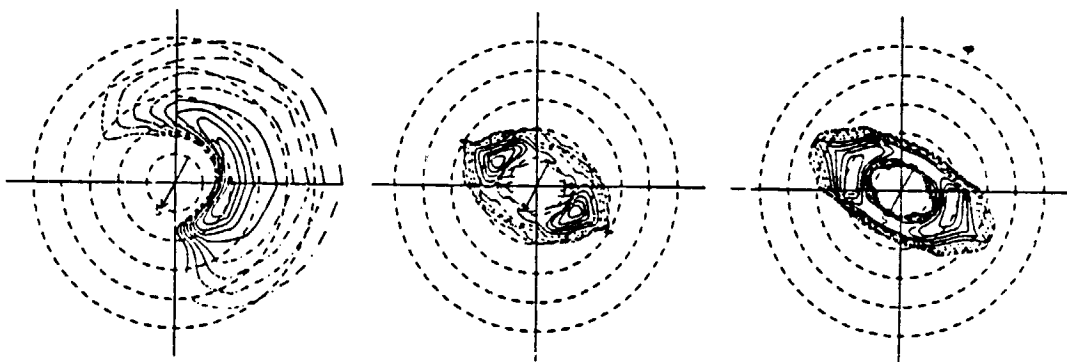# Max-Planck-Institut für Meteorologie

## REPORT No. 19



## EUROPEAN SPACE AGENCY CONTRACT REPORT

## DEVELOPMENT OF A SATELLITE SAR IMAGE SPECTRA AND ALTIMETER WAVE HEIGHT DATA ASSIMILATION SYSTEM FOR ERS--1

AUTHORS

K. Hasselmann
S. Hasselmann
E. Bauer
C. Brüning
S. Lehner
H. Graber
P. Lionello

# ESA STUDY CONTRACT REPORT

No ESA Study Contract Report will be accepted unless this sheet is inserted at the beginning of each volume of the Report

| ESA CONTRACT NO<br><br>6875 / 87 / HGE I (SC) | SUBJECT     Development of a satellite SAR image spectra and altimeter wave height data assimilation system for ERS-1 | | NAME OF CONTRACTOR<br><br>MPI |
|---|---|---|---|
| * ESA CR( ) No: 1 | * STAR CODE | No. of Volumes     1<br>This is Volume No:   1 | CONTRACTOR'S REFERENCE |

ABSTRACT

A study on the applicability of ERS-1 wind and wave data for wave models is carried out using the WAM third generation wave model and SEASAT altimeter, scatterometer and SAR data.

A series of global wave hindcasts is made for the surface stress and surface wind fields derived by Atlas et al. (1987) by assimilation of scatterometer data for the full 96-day SEASAT and also for two wind field analyses for shorter periods produced by Anderson et al. (1987) (by assimilation with the higher resolution ECMWF T63 model) and by Woiceshyn et al. (1987) (by subjective analysis methods). It is found that wave models respond very sensitively to inconsistencies in wind field analyses and therefore provide a valuable data validation tool.

Comparisons between SEASAT SAR image spectra and theoretical SAR spectra derived from the hindcast wave spectra by Monte Carlo simulations yielded good overall agreement for 32 cases representing a wide variety of wave conditions. It is concluded that SAR wave imaging is sufficiently well understood to apply SAR image spectra with confidence for wave studies if supported by realistic wave models and theoretical computations of the strongly nonlinear mapping of the wave spectrum into the SAR image spectrum. A new, closed nonlinear integral expression for this spectral mapping relation is derived which avoids the inherent statistical errors of Monte Carlo computations and may prove to be more efficient numerically.

A theoretical framework is developed for the assimilation of arbitrary wave data in models in which the wind and wave fields are modified simultaneously in accordance with the constraints imposed by the wave model. As a first step, a simplified wave data assimilation exercise is carried out in which only the wave field is modified.

The work described in this report was done under ESA contract. Responsibility for the contents resides in the author or organisation that prepared it.

Names of authors:

Klaus Hasselmann            Susanne Lehner
Susanne Hasselmann      Hans Graber
Eva Bauer                  Piero Lionello
Claus Brüning

| ** NAME OF ESA STUDY MANAGER<br>      E Oriol<br>DIV:      OEE | ** ESA BUDGET HEADING<br><br>65-512 | |
|---|---|---|

* Sections to be completed by ESA

** Information to be provided by ESA Study Manager

Max-Planck-Institut für Meteorologie
Bundesstrasse 55, 2000 Hamburg 13, FRG
Report No. 19

# EUROPEAN SPACE AGENCY CONTRACT REPORT

# DEVELOPMENT OF A SATELLITE SAR IMAGE SPECTRA AND ALTIMETER WAVE HEIGHT DATA ASSIMILATION SYSTEM FOR ERS-1

AUTHORS:
K. Hasselmann [1]
S. Hasselmann [1]
E. Bauer [2]
C. Brüning [3]
S. Lehner [4]
H. Graber [5]
P. Lionello [6]

ESRIN CONTRACT NO:
6875 / 87 / HGE I (SC)

ESRIN STUDY MANAGER:
E. ORIOL

[1] Max-Planck-Institut für Meteorologie, Hamburg

[2] Institut für Meereskunde, University of Hamburg

[3] European Centre for Medium Range Weather Forecasts, Reading

[4] formerly Deutsche Forschungs- und Versuchsanstalt fur Luft- und
Raumfahrt e.V., Oberpfaffenhofen

[5] Woods Hole Oceanographic Institution, Woods Hole

[6] Laboratorio per lo Studio della Dinamica delle Grandi Masse, Venezia

## Acknowledgements

## Contents

## Abstract

A study on the applicability of ERS-1 wind and wave data for wave models is carried out using the WAM third generation wave model and SEASAT altimeter, scatterometer and SAR data. A series of global wave hindcasts are made using as input driving fields.

(i)     the six-hourly averaged surface stress fields derived by Atlas et al (1987) for the full 96-day SEASAT period 7 July - 10 October 1978 by assimilation of scatterometer data with conventional meteorological data using the Goddard Laboratory of Atmospheres 4° x 5°, 9 level atmospheric model,

(ii)    the 1000 mb wind field from the same GLA analysis for August, 1978,

(iii)   the 1000 mb wind field derived by Anderson et al. (1987) for the period September 6 - 17, 1978, using more sophisticated assimilation techniques and the higher resolution T63 (1.875° X 1.187°, 19 layer) model of the European Centre for Medium Range Weather Forecasts, and

(iv)    a subjectively analysed scatterometer wind field produced by Woiceshyn et al (1987) for the period September 6 - 20

The four hindcasts are intercompared and verified against altimeter wave height and wave buoy data. In the northern hemisphere the hindcasts agree reasonably well with each other and with the observations. However, strong deviations between the hindcast for the GLA stress field and the other three hindcasts are found in the high wind belts in the southern hemisphere This is tentatively attributed to the six-hourly averaging applied in the computation of the surface stress fields.

It is concluded that wave models provide a very sensitive mechanism for identifying inconsistencies in wind field analyses The simultaneous operation of a wave model in conjunction with an atmospheric model in a joint wind and wave data assimilation system therefore provides a valuable data validation tool.

Comparisons are also made between SEASAT SAR image spectra and theoretical SAR spectra derived from the hindcast wavespectra by Monte Carlo simulations Good overall agreement is found for 32 cases representing a wide variety of wave conditions In most cases the input wave spectrum is strongly distorted in the SAR spectrum by nonlinear motion effects The linear treatment of motion effects (in terms of a velocity bunching transfer function) was found to yield unrealistic monotonically increasing wave spectra in all cases (including swell fields) It is concluded that SAR wave imaging is sufficiently well understood to apply SAR image spectra

with confidence for wave studies. However, SAR data can be meaningfully interpreted only in conjunction with a realistic wave model and detailed computations of the mapping of the two-dimensional ocean wave spectrum into the SAR image spectrum.

A new, closed nonlinear integral expression for this spectral mapping relation is derived which avoids the inherent statistical errors of the Monte Carlo approach. The method may also prove to be more efficient numerically. This is an important consideration in view of the extensive computations required for the analysis of the global SAR spectral data set produced by the ERS-1 AMI instrument operating in the wind/wave mode

A theoretical framework is developed for the simultaneous assimilation of arbitrary wave data (e.g. wave heights, buoy spectra or SAR image spectra) in numerical weather prediction and wave models. Both wind and wave fields are modified simultaneously in accordance with the constraints imposed by the wave model. The explicit integration of the adjoint wave equation required in the general formulation of the problem is avoided by using an approximate (diagonal) Green function, the elements of which are already computed as part of the wave model's implicit integration scheme

An example of a simplified wave data assimilation scheme is presented in which only the wave field is modified. The assimilated wave data are the global SEASAT altimeter wave heights for August, 1978. A considerable improvement in the wave forecast is achieved in the tropics and northern hemisphere, where most of the wave energy consists of swell. However, the errors are only partially reduced in the principal generating regions of the higher latitude southern hemisphere, where the unmodified surface stress field regenerates incorrect windseas. These deficiencies would presumably be remedied in a joint wind/wave assimilation scheme

# 1    Introduction

## 1 1    Background

The present study contract represents a complementary investigation to a previous ESA two-part study on the feasibility of developing and implementing a comprehensive data assimilation system for the near real time analysis of ERS-1 wind and wave data. It should therefore be viewed in the context of these study contracts (ESRIN Contract No. 6297/86/HGE-I(SC), Part I, Anderson et al., 1987, Part II, Janssen et al., 1988). The work carried out in these three studies must also be seen in a broader perspective within the framework of a longer term international programme to use ERS-1 wind and wave data, together with conventional weather network data and other in situ data, to compute the global fields of all fluxes at the air/sea interface on a continual, operational basis, beginning 1991 These activities are coordinated in the Global Assimilation Programme for Air/Sea Fluxes by the JSC/CCCO Working Group on Air/Sea Fluxes (cf Appendix). In the following a brief summary is given of earlier work which has provided the basis for the studies carried out in the three ESA contracts and for the planning of the Global Assimilation Programme for Air/Sea Fluxes

## 1.2    Need for a data assimilation system

The extensive oceanographic surface data which will be provided by the suite of sensors on ERS-1 open exciting new opportunities to the oceanographic community But the preparation for the effective use of these data also poses a severe challenge This is well illustrated by SEASAT The wave hindcasts presented in this study and in the companion study contract (Part II, P Janssen et al, 1988) represent the first application of SEASAT data to a global ocean wave hindcast – fully nine years after the launch of SEASAT! The computation of the surface stress fields used in these hindcasts for the 96-day period during which the SEASAT scatterometer was operating was only completed, with considerable effort and perseverance, eight years after launch (Atlas et al., 1987) The analysis was based on an off-line data assimilation system using the non-operational, relatively low resolution GLA (Goddard Laboratory of Atmospheres) atmospheric model These data processing problems would have been still more apparent if SEASAT had flown, as planned, for several years rather than three months Although SEASAT provided an impressive demonstration of the great scientific and operational potential of ocean satellites, it also clearly revealed the problems the scientific community faces in using satellite data if provisions are not made for the timely implementation of an effective

operational data assimilation system capable of processing all incoming satellite and conventional data in a single quasi real-time operation.

It should be stressed that the main delays in the production of the level III final SEASAT data set were not caused by the processing of the raw data or the provision of appropriate algorithms, but by the last, most complex element of the data processing chain: the data assimilation system. The assimilation systems used by Atlas et al. (1987) and Anderson et al. (1987) can furthermore still be viewed only as a first step. Ideally, such a system should combine all the wind and wave data provided by the satellite with all relevant data from other sources to construct simultaneously global fields of the surface wind and sea state. Both in the GLA system and in the more sophisticated ECMWF (European Centre for Medium Range Weather Forecasts) data assimilation system, wave information was not used in constructing the wind field. Another important feature of an effective assimilation system is that it should be implemented in an operational global wind and wave forecasting environment. Although evidence of deficiences in the SEASAT scatterometer data had already been pointed out earlier (Woiceshyn et al., 1987), the present study, together with the previous ESA assimilation studies, revealed many further sources of error and data inconsistencies. These can be routinely identified and corrected only by carrying out a complete data assimilation and data validation cycle within a quasi-operational setting, using state-of-the-art, high resolution atmospheric circulation and global wave models.

1 3    Previous work

The scientific community has long been aware of the potential but also the difficulties of implementing an effective ocean satellite data assimilation system. Accordingly, since the early conception of ERS-1 it has been preparing a programme and some of the necessary tools for the development and implementation of a comprehensive, quasi real-time, operational data assimilation system for the satellite.

The first step in this programme was the development of a realistic global wave model. While the ERS-1 community had access to the world's foremost global atmospheric model and atmospheric data assimilation system at the ECMWF, a global wave model of similar capability did not exist. The only global wave models in operation in the early eighties were first or second generation models, whose basic shortcomings have been identified in the Sea Wave Modelling Project (The SWAMP Group, 1985). In recognition of these deficencies, the WAM (Wave Modelling) Group

2

was formed to develop a third generation ocean wave model. One of the main motivations of the WAM Group was to apply the model later for ERS-1

The development of the WAM model involved an extensive series of investigations, including improved computations of the nonlinear transfer which governs the evolution of the windsea spectrum (Hasselmann and Hasselmann, 1981, 1985), the application of the improved nonlinear transfer computations to study the energy balance of the wave spectrum and derive improved representations of the input and dissipation source functions (Komen et al., 1984), and the development of simpler parameterizations of the nonlinear transfer applicable in a global wave model (Hasselmann et al., 1985) This work was partly supported by ESA through Study Contract N° 6875/87/HGE-I (SC)  Finally, it required the translation of these research results into a reliable numerical global wave model (Hasselmann and Hasselmann, 1985 - WAM-Report). The model has been implemented at the Max-Planck-Institute and ECMWF, where it is used in a quasi-operational mode (Janssen et al., 1988)  It has now been extensively tested in a series of hindcast cases and in quasi-operational forecasts. A detailed presentation of the model and its application to ten hindcast studies is given in WAMDIG (1988). The model has meanwhile been distributed together with a users' manual (Hasselmann, 1987) to more than twenty groups  The cycle 1 version of the model runs on both a CRAY XMP (ECMWF) and a CYBER 205 (MPI) vector computer (an improved cycle 2 has recently been completed)

Another important task which has been addressed is the interpretation and application of SAR wave images  The incorporation of SAR wave data in the general data assimilation system poses a number of problems  While SEASAT provided impressive evidence that waves can be imaged from a spaceborne SAR at 800 km height, the interpretation of SAR wave images has long been a subject of intense debate  In the last years a reasonable consensus has emerged on the imaging mechanism as such (cf Section 4 1)  The principal backscattering mechanism in the range of incidence angles of the SAR on ERS-1 is Bragg backscattering by short ripples in the 5 - 10 cm wave length range  The SAR is able to image long ocean waves because the Bragg backscattering by the short ripples is modulated by the longer waves  The modulation is caused by three processes: hydrodynamic interactions, changes in the local angle of incidence by the long wave tilt variations, and variations in the long wave orbital velocity  The last process gives rise to Doppler shifts in the backscattered signal which produce azimuthal displacements of the apparent positions of the backscattering elements in the SAR image plane (velocity bunching)  Whereas the hydrodynamic and tilt modulation can be regarded as linear processes, at least to first

3

order, the velocity bunching process can become strongly nonlinear. For steep windseas the nonlinearity can even result in a complete loss of the wave image through azimuthal smearing.

One of the main tasks in preparing for the application of ERS-1 SAR wave data was therefore to develop nonlinear transformation algorithms relating the SAR image spectrum to the surface wave spectrum. Significant progress in this question has been made by Bruening and Alpers (1985) and Bruening et al. (1988). The authors computed the nonlinear mapping from the surface wave spectrum to the SAR image spectrum by direct Monte Carlo simulations. Unfortunately, this method is too costly in computer time to be routinely applied to all ERS-1 SAR wave data collected in the SAR wave mode. However, in the course of the present study a new closed, nonlinear integral expression has been derived describing the mapping of the surface wave spectrum into the SAR image spectrum. It is hoped that computations of this integral transform can be carried out sufficiently rapidly to be routinely applied for the assimilation of ERS-1 SAR image spectra. The computation also has the advantage of avoiding the statistical scatter which arises in Monte Carlo simulations. However, it should be stressed that effective methods for the inverse mapping from the SAR spectrum to the wave spectrum have not yet been developed. Such techniques will presumably involve some form of iteration, which implies that in practice SAR image spectra can be usefully assimilated only if first guess wave spectra are available from a wave model.

With the development and implementation of a reliable third generation global wave model and the clarification of the relation between the ocean wave spectrum and the SAR image spectrum, important first steps for the implementation of an ERS-1 wind and wave data assimilation system have now been completed. However, further major tasks still need to be undertaken.

General overviews of the complete data assimilation problem have been given in several position papers prepared by working groups and individual discussants in a number of recent ESA workshops (cf. Proc. Conf. Alpbach and Schliersee). A comprehensive summary may be found in the Global Data Assimilation Programme for Air/Sea Fluxes (an excerpt is given in the Appendix). The relation of this programme to the present study contract is discussed in the next section.

1

## 1.4 The Global Data Assimilation Programme for Air/Sea Fluxes (GDAP)

This programme has been initiated by the JSC/CCCO[1] Working Group on Air/Sea Fluxes, in response to the needs of the WOCE[2] and TOGA[3] scientific community, to provide continuous, gridded, global fields of all physical fluxes at the air/sea interface (momentum, sensible and latent heat, water, and solar and infra-red radiation). The fluxes determine the coupling between the atmosphere and the ocean, the understanding of which is an essential component of the WOCE and TOGA programmes.

The goal of the GDAP is to provide continuous 6 hourly, 1° x 1° global flux fields, beginning in the early nineties with the deployment of ERS-1, the first of the next generation ocean satellites. In developing the programme, the JSC/CCCO Working Group on Air/Sea Fluxes has drawn heavily on the contributions of other working groups, such as the Working Group on Numerical Experimentation (WGNE) and the JSC Working Group on Radiation, which are providing important contributions to special aspects of the overall programme.

The programme is sub-divided into two phases (cf. Appendix): a preparatory phase, from 1988 - 1990, and an implementation phase, from 1991 onwards. Principal assimilation centres are to be established in Europe, at the European Centre for Medium Range Weather Forecasts and in the U S , at the National Meteorological Center, with further assimilation systems at other national weather centres.

Within the two programme phases, fourteen major tasks are identified. It should be noted that the present ESA study contracts address only a small sub-set of these tasks (projects 4 3, 4 10, 4 12 – cf Appendix) The impact of the ESA study contracts on the overall programme and the inferences which may be drawn from these investigations for the future development of the programme are discussed briefly in Section 8 (Conclusions).

-----------------------------------------------------------------------------------

[1] Parent bodies of the Working Group on Air-Sea Fluxes are the Joint Scientific Committee (JSC) of the World Climate Research Programme and the Committee on Climatic Changes and the Ocean (CCCO)

[2] World Ocean Circulation Experiment

[3] Tropical Ocean/Global Atmosphere Project

## 1.5 Relation of present study contract to previous ESA data assimilation study contracts

The common purposes of the previous ESA study contract, Part I (Anderson et al., 1987) and Part II (Janssen et al., 1988), and the present contract were

- to establish the general feasibility of using a combined wind and wave data assimilation system for the analysis of ERS-1 wind and wave data,

- to gather experience in the operation of such systems through experiments with SEASAT data,

- to define more clearly the requirements for the implementation of a wind and wave data assimilation system in time for the launch of the ERS-1, and

- to investigate the value of applying a wind and wave data assimilation system in support of measurement campaigns and during the ERS-1 calibration and validation phase.

Within this general framework, the individual study contracts addressed the following tasks:

Part I - Wind Scatterometer Data (Anderson et al., 1987)

- investigation of methods of assimilating wind scatterometer data together with the FGGE data set using the ECMWF higher resolution forecast model and operational assimilation system,

- validation of the SEASAT scatterometer data,

- intercomparison of scatterometer winds with ship winds,

- investigation of the impact of scatterometer winds on the analysis and forecast,

- intercomparison of different scatterometer dealiasing algorithms.

6

<u>Part II</u> - Use of scatterometer and altimeter data in wave modelling and assimilation
(Janssen et al., 1988)

- application of ECMWF wind fields produced in Part I to a global wave hindcast,

- intercomparison of global wave hindcasts produced by wind fields from the
  ECMWF data assimilation system (Part I) and by wind fields obtained at JPL by
  subjective analysis of SEASAT scatterometer data (Woiceshyn et al., 1987),

- comparison of global wave hindcast with wave buoy data and SEASAT altimeter
  data,

- wave data assimilation experiments using altimeter data

<u>Present Contract</u> - SAR image spectra and altimeter wave height data assimilation
system for ERS-1.

Most of the numerical experiments in Parts I and II of the study contract were
carried out for the 11-day period September 6 - 17, 1978. This limitation was imposed
by the expense of the atmospheric data assimilation exercise and the limited period
covered by the subjectively analyzed JPL wind data set. In contrast, most of the
investigations of this study contract were carried out for the full 96-day period July 7 -
October 10, 1978, for which the SEASAT scatterometer was operating. The global
wind and surface stress fields for this period were kindly provided by the Goddard
Laboratory of Atmospheres. They were produced by a data assimilation exercise
(Atlas et al., 1987) similar to that carried out by ECMWF, but using the significantly
coarser resolution GLA model ($4° \times 5°$, 9 layers, as compared with $1.875° \times 1.875°$, 19
layers for the ECMWF model).

The following investigations were carried out.

- global wave hindcast for the full 96-day SEASAT period using the GLA surface
  stress field as driving field.

- intercomparison of assimilated wind fields and altimeter wind speeds for this
  period,

- intercomparison of the G_A surface wind and surface stress fields with the ECMWF and JPL fields for the common period of overlap, September 6 - 17, 1978,

- intercomparison of the global wave hindcasts for the three wind fields for the same common period,

- intercomparison of the 96-day global wave hindcast with SEASAT altimeter wave heights, wave buoys and SEASAT SAR image spectra,

- comparison of theoretical relation between surface wave spectra and SAR wave image spectra with measured SEASAT wave image spectra,

- development of a new theoretical integral transformation expression describing the nonlinear mapping from a surface wave spectrum into a SAR image spectrum,

- an example of wave data assimilation for the month of August, 1978,

- development of general methods for the assimilation of wave data in wave models,

- recommendations for future actions,

- definition of requirements for the future implementation of a general data assimilation system for ERS-1 wind and wave data.

The results of these investigations are presented, in the order listed, in the following sections.

## 2 Global wave hindcast for the 95-day SEASAT period

To test the impact of the simultaneous use of satellite wind and wave data in a wave model, a global wave hindcast was carried out for the full SEASAT scatterometer period July 7 - October 10, 1978, using as input the global surface stress field of Atlas et al. (1987) (the wave model requires surface stresses rather than the surface winds as input). The stress field was constructed through the assimilation of SEASAT scatterometer wind data and conventional atmospheric data using the GLA atmospheric model. The global hindcast was carried out on the CYBER 205 at the MPI using the WAM third generation model, which is described in detail in WAMDIG (1988) (see also Part II of the previous ESA study contract, Janssen et al., 1988)

In this section we compare the model hindcast with the SEASAT altimeter wave heights and wave buoy data. A detailed comparison with SAR wave data is given later in Section 5, following a presentation of SAR imaging theory in Section 4.

### 2.1 Comparison with averaged SEASAT altimeter wave height fields

Figures 2.1 - 2.5 show (approximately) monthly averaged fields for the GLA wind stress, hindcast significant wave height and direction (Custer diagram), sub-divided into the contributions for the total wave field, windsea and swell, and the SEASAT altimeter wave heights (provided by JPL). The averaging periods (cf. Table 1) are the same as the periods selected by Mognard et al. (1983) (except for a data gap of 10 days at the end, in October, due to a faulty tape; other gaps are due to missing altimeter data).

The separation of the total wave spectrum $F(f,\theta)$ into windsea and swell contributions in Figs 2.3, 2.4 was based on the criterion

$$\left( \frac{1.2 \cdot 28 \cdot u_* \cos(\theta - \theta_w)}{c} - 1 \right) \quad \begin{cases} > 0 : \text{windsea component} \\ \\ < 0 : \text{swell component} \end{cases} \qquad (2.1)$$

where $c$ = phase velocity, $\theta$ = wave propagation direction, $\theta_w$ = wind direction

July (cf. Figs 2.1 - 2.5, Panels a)

11.07.1978, 00:00 - 17.07.1978, 16.00
    and
24.07.1978, 10:00 - 31.07.1978, 00:00

August (cf Figs 2.1 - 2.5, Panels b)

01.08.1978, 00:00 - 28.08.1978, 07.00

September (cf Figs 2.1 - 2.5, Panels c)

06.09.1978, 00:00 - 07.09.1978, 00:00
    and
15.09.1978, 00:00 - 30.09.1978, 00:00

**Table 1:** Averaging periods for SEASAT altimeter wave heights and model hindcast wave heights shown in Figs 2.1 - 2.5
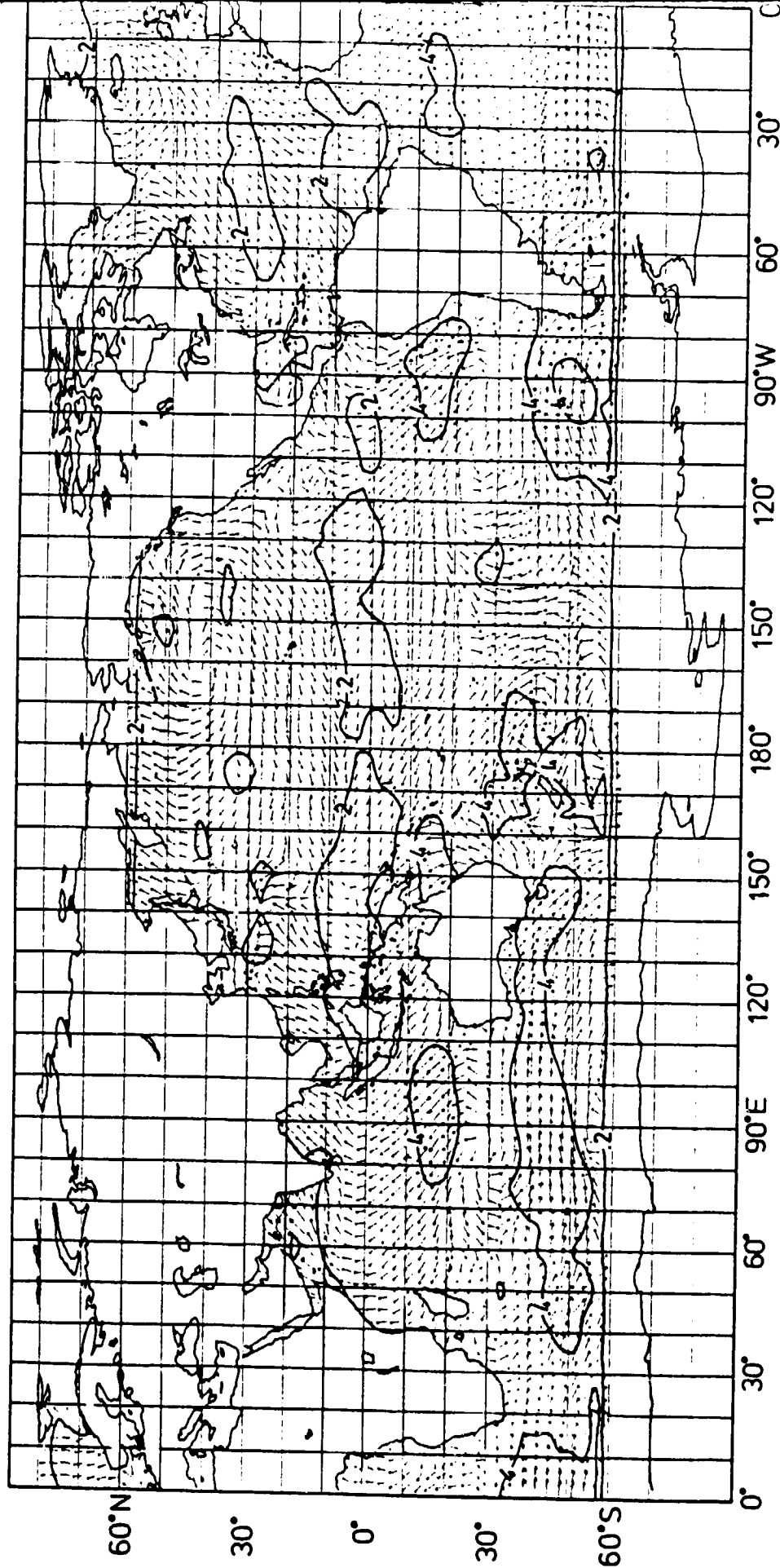
Fig 2 1 a    Averaged GLA surface stress fields (direction and magnitude, indicated by isolines and length of arrows), for July 1978 (averaging periods are given in Table 1)
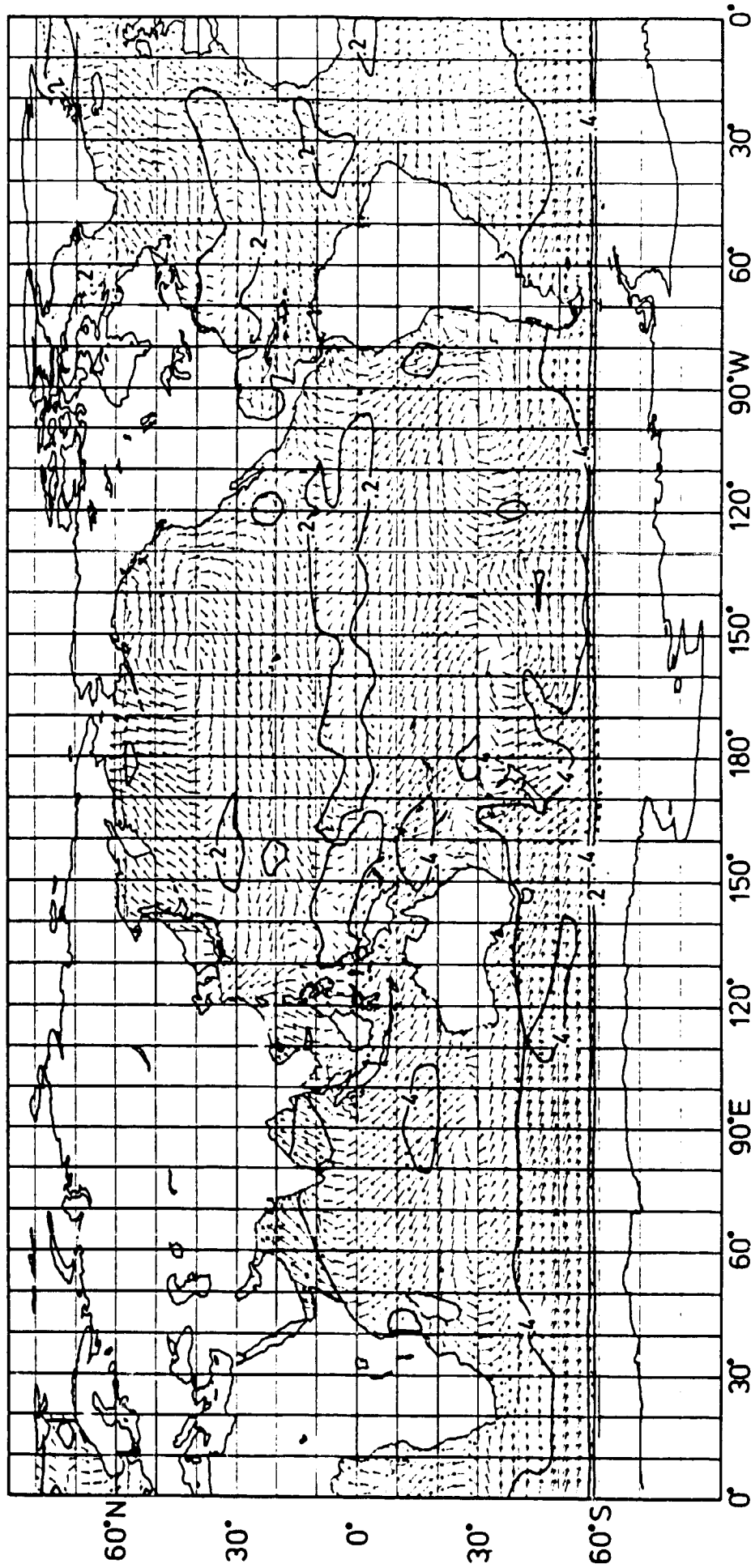
11

Fig. 2.1 b    Averaged GLA surface stress fields (direction and magnitude, indicated by isolines and length of arrows), for August 1978 (averaging periods are given in Table 1)
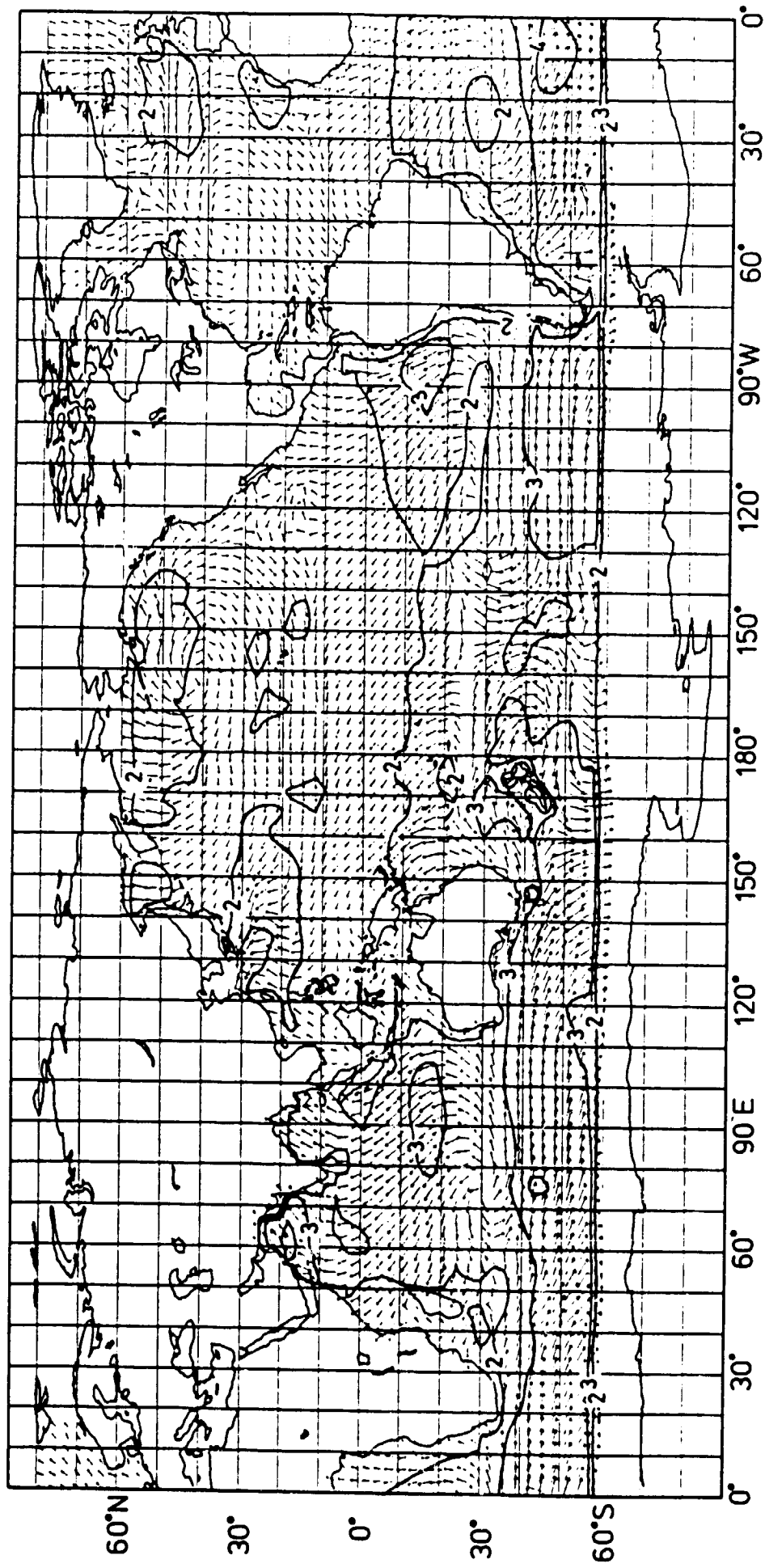
Fig 2 1c   Averaged GLA surface stress fields (direction and magnitude, indicated by
isolines and length of arrows), for September-October 1978 (averaging
periods are given in Table 1).

13

Fig 2 2 a

Averaged significant wave height and mean direction for the hindcast total wave field for July 1978 (averaging periods are given in Table 1). Wave heights are indicated by isolines and lengths of wave direction arrows
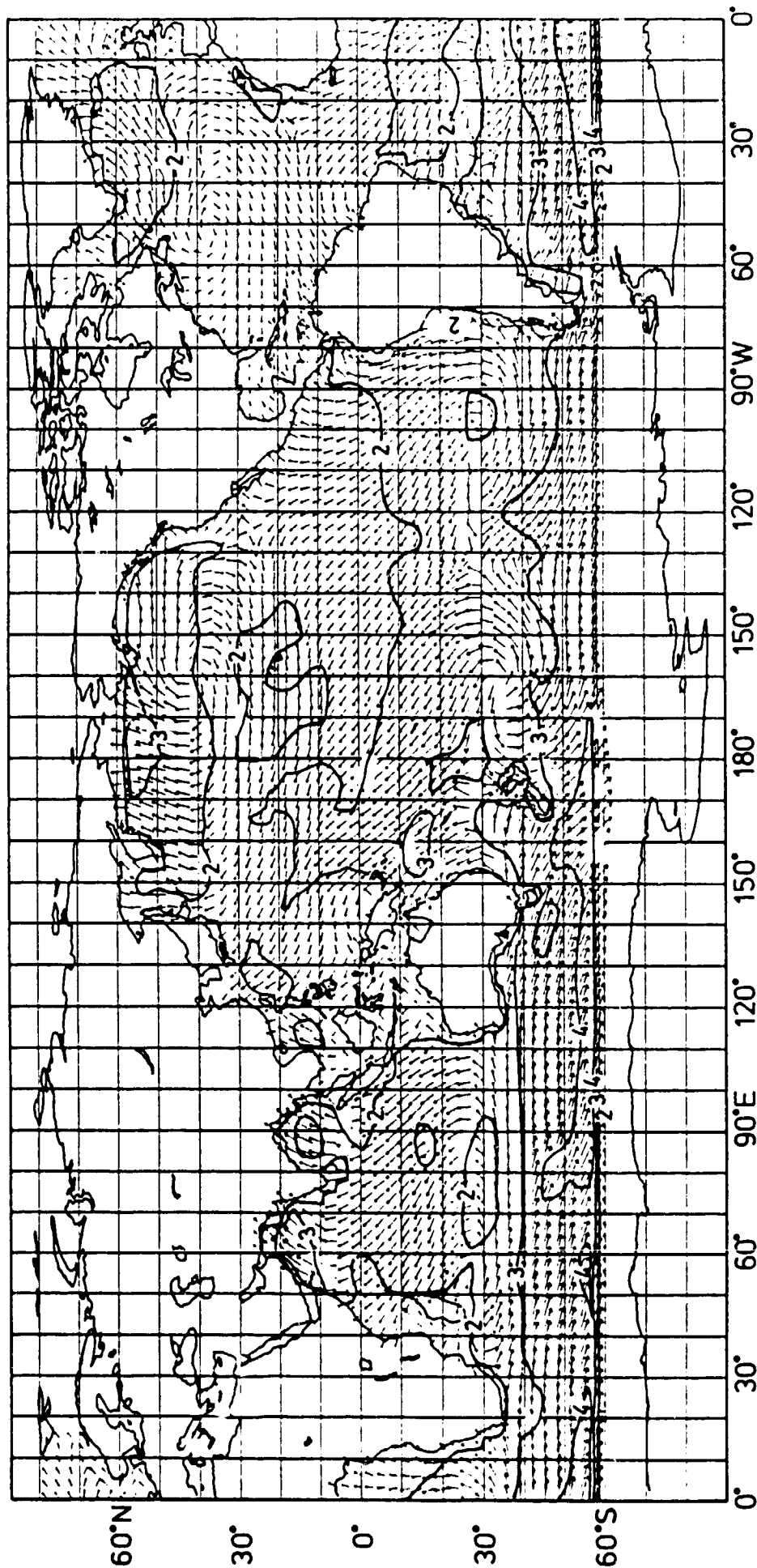
14

Fig 2 2 b    Averaged significant wave height and mean direction for the hindcast total wave field for August 1978 (averaging periods are given in Table 1). Wave heights are indicated by isolines and lengths of wave direction arrows
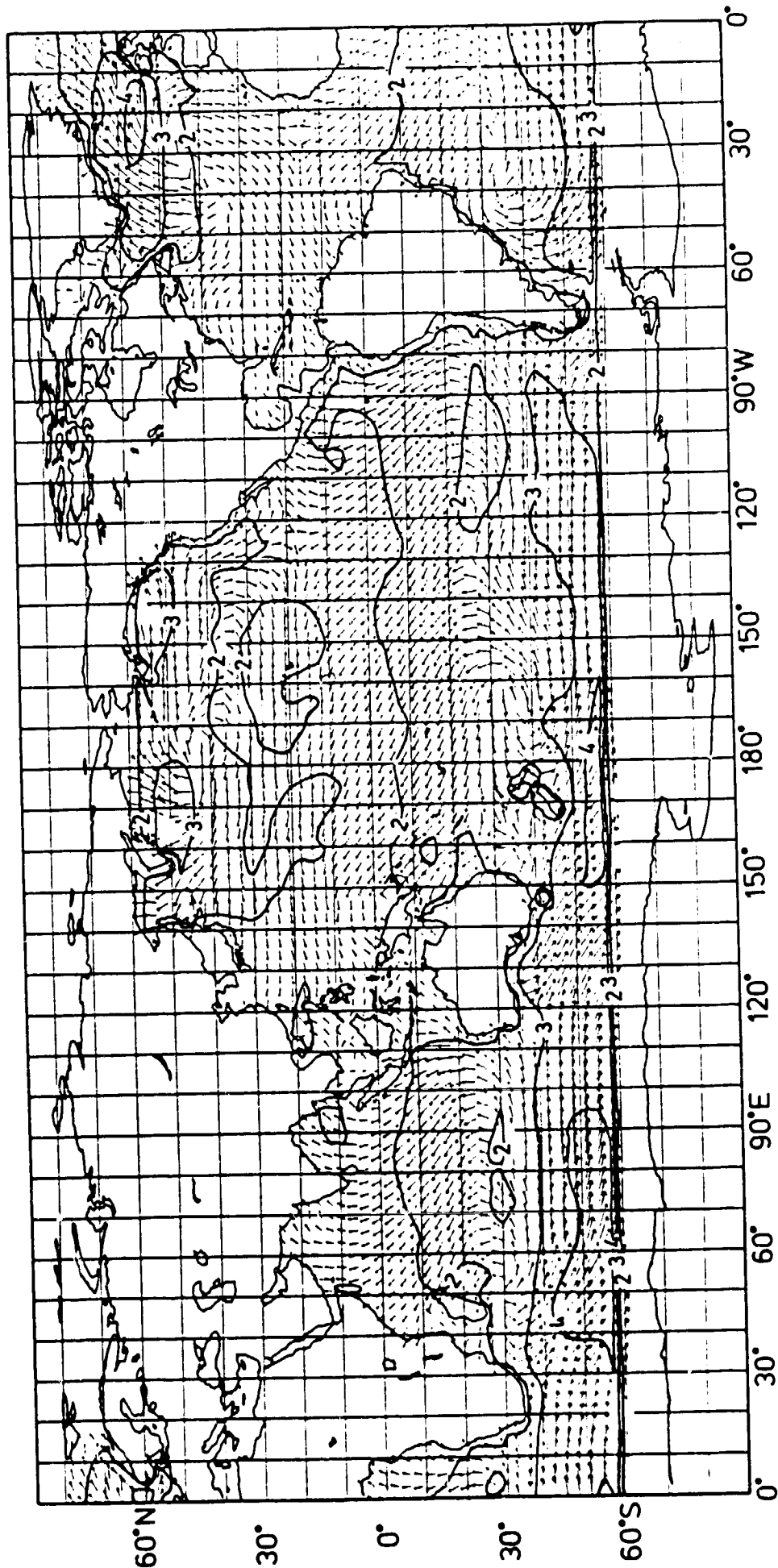
Fig 2 2 c    Averaged significant wave height and mean direction for the hindcast total
wave field for September 1978 (averaging periods are given in Table 1)  Wave
heights are indicated by isolines and lengths of wave direction arrows
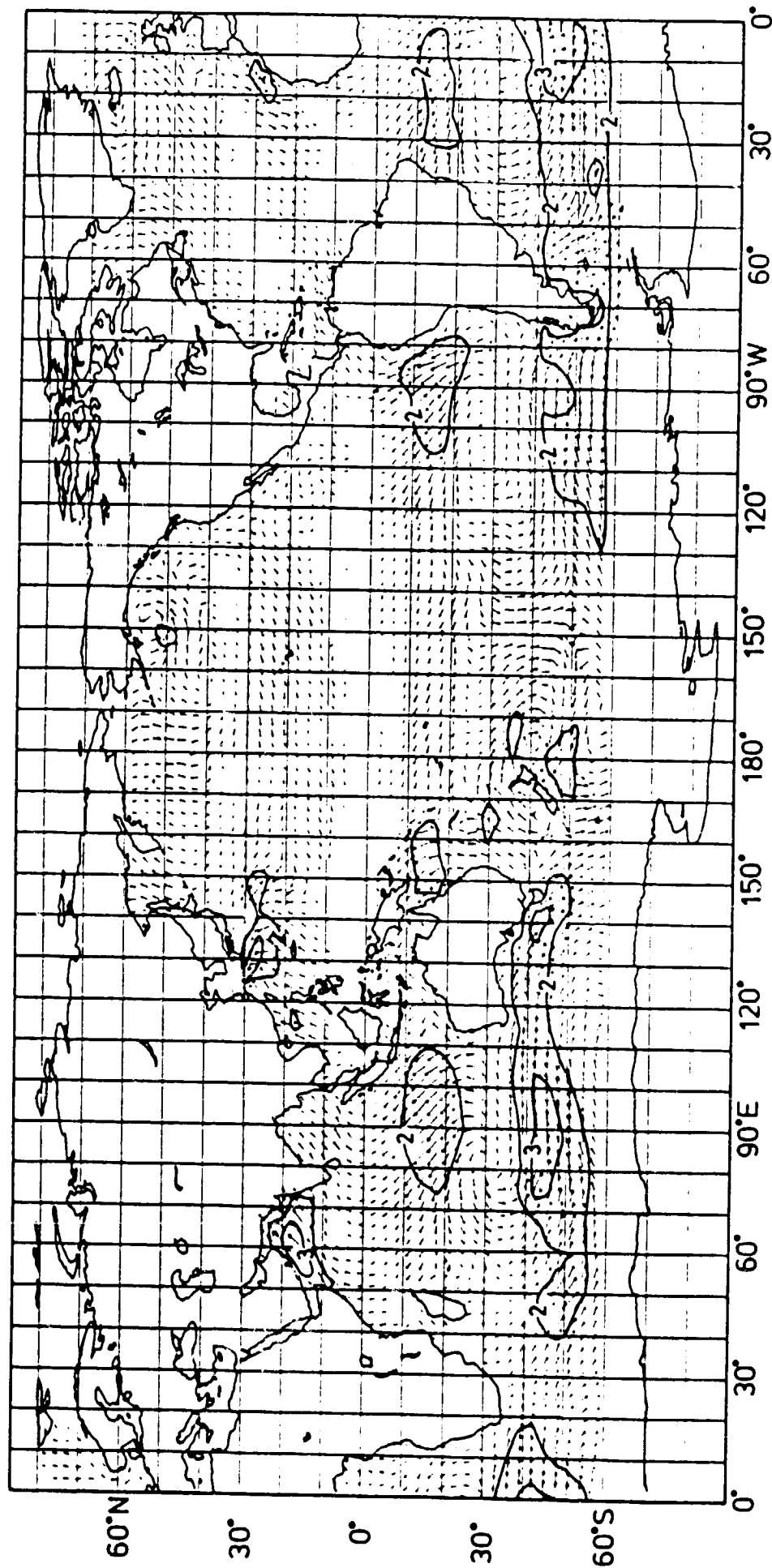
16

Fig 2 3 a

Averaged significant wave height and mean direction for the hindcast
windsea for July 1978 (averaging periods are given in Table 1). Wave heights
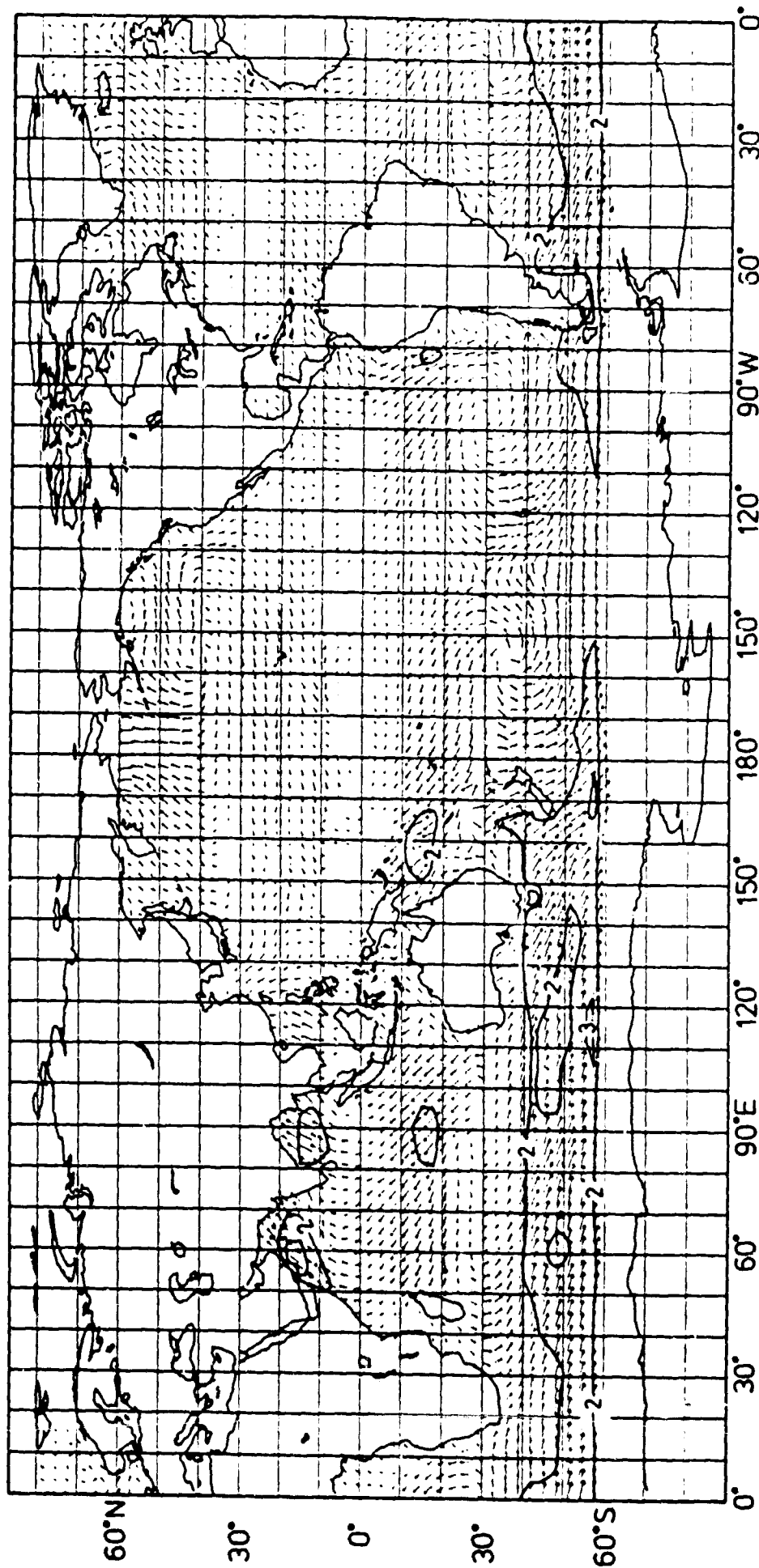are indicated by isolines and lengths of wave direction arrows

Fig 2.3.b

Averaged significant wave height and mean direction for the hindcast windsea for August 1978 (averaging periods are given in Table 1). Wave heights are indicated by isolines and lengths of wave direction arrows
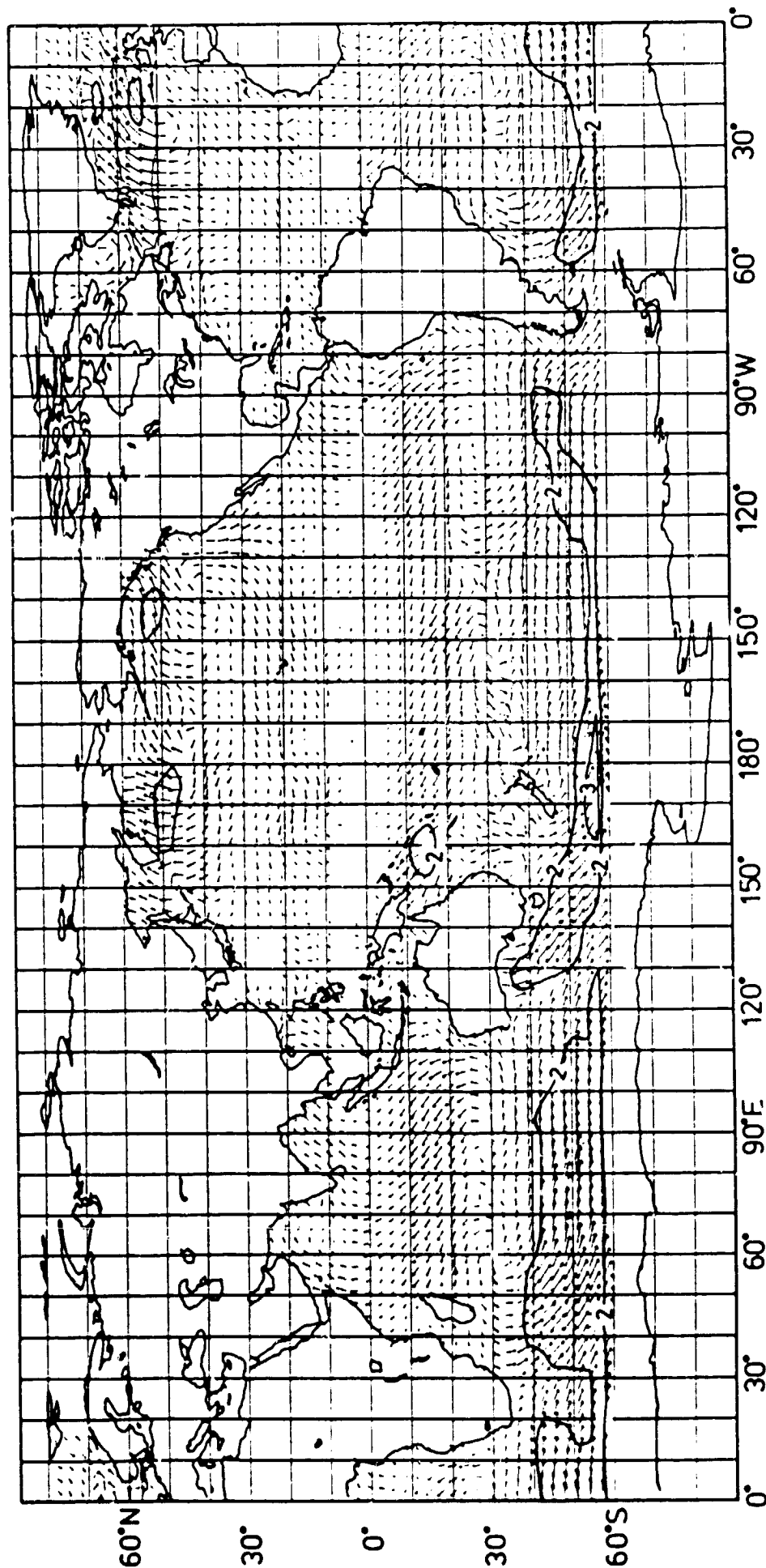
Fig 2.3 c    Averaged significant wave height and mean direction for the hindcast
windsea for September 1978 (averaging periods are given in Table 1). Wave
heights are indicated by isolines and lengths of wave direction arrows

19

Fig 2 4 a     Averaged significant wave height and mean direction for the hindcast swell
for July 1978 (averaging periods are given in Table 1). Wave heights are
indicated by isolines and lengths of wave direction arrows

Fig 2 4 b     Averaged significant wave height and mean direction for the hindcast swell
for August 1978 (averaging periods are given in Table 1) Wave heights are
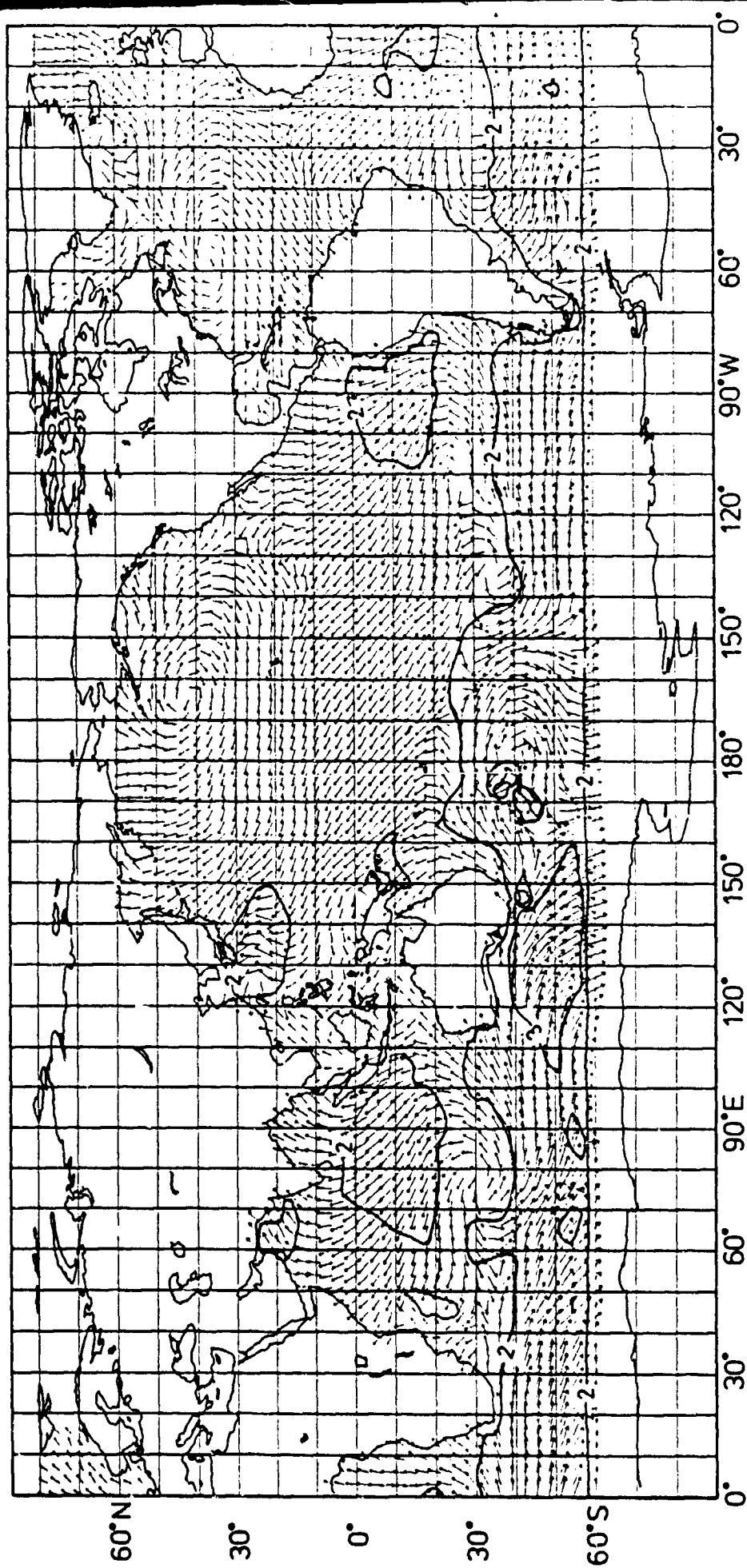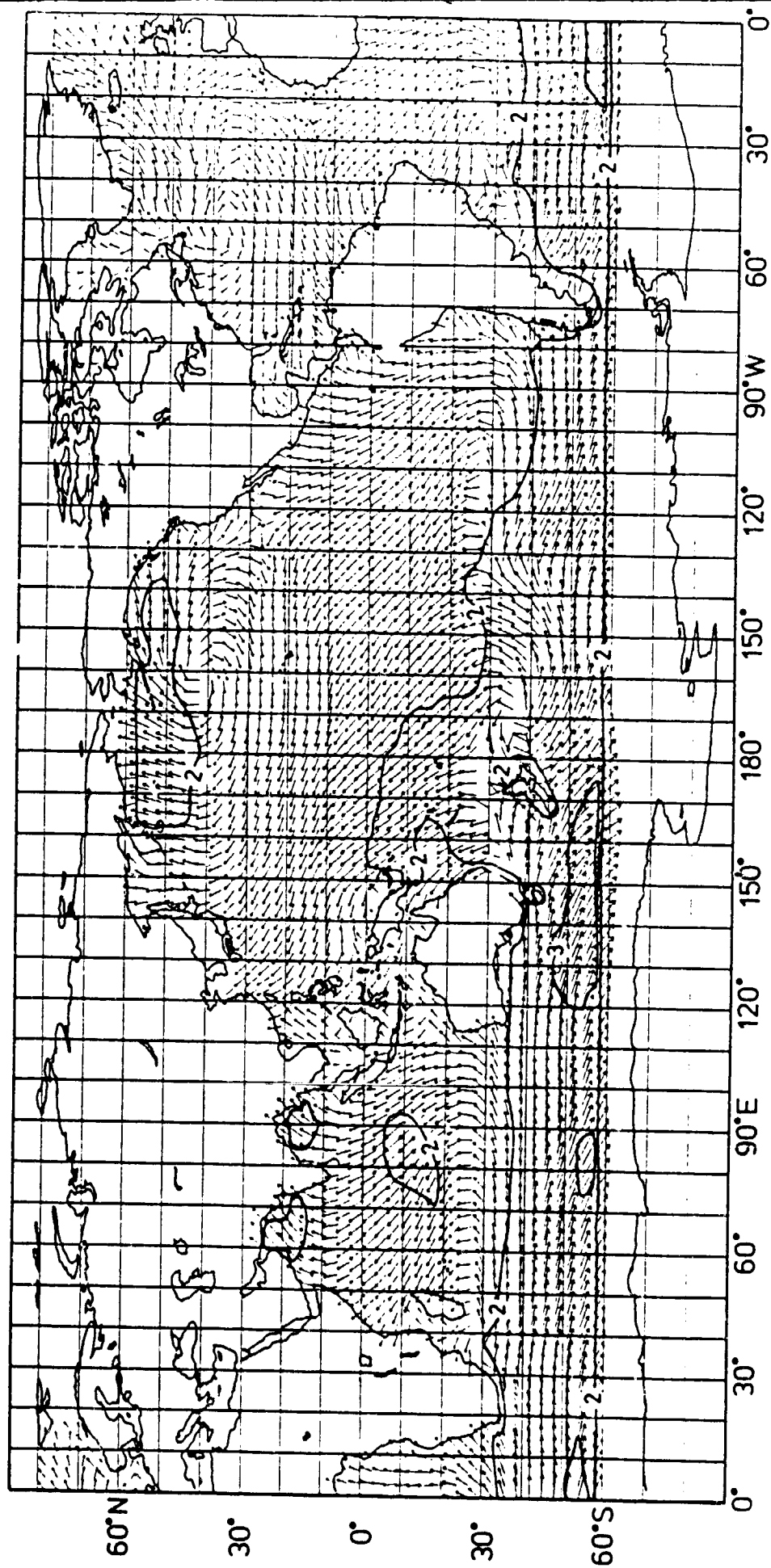indicated by isolines and lengths of wave direction arrows

21

Fig. 2.4 c

Averaged significant wave height and mean direction for the hindcast swell
for September 1978 (averaging periods are given in Table 1). Wave heights
are indicated by isolines and lengths of wave direction arrows
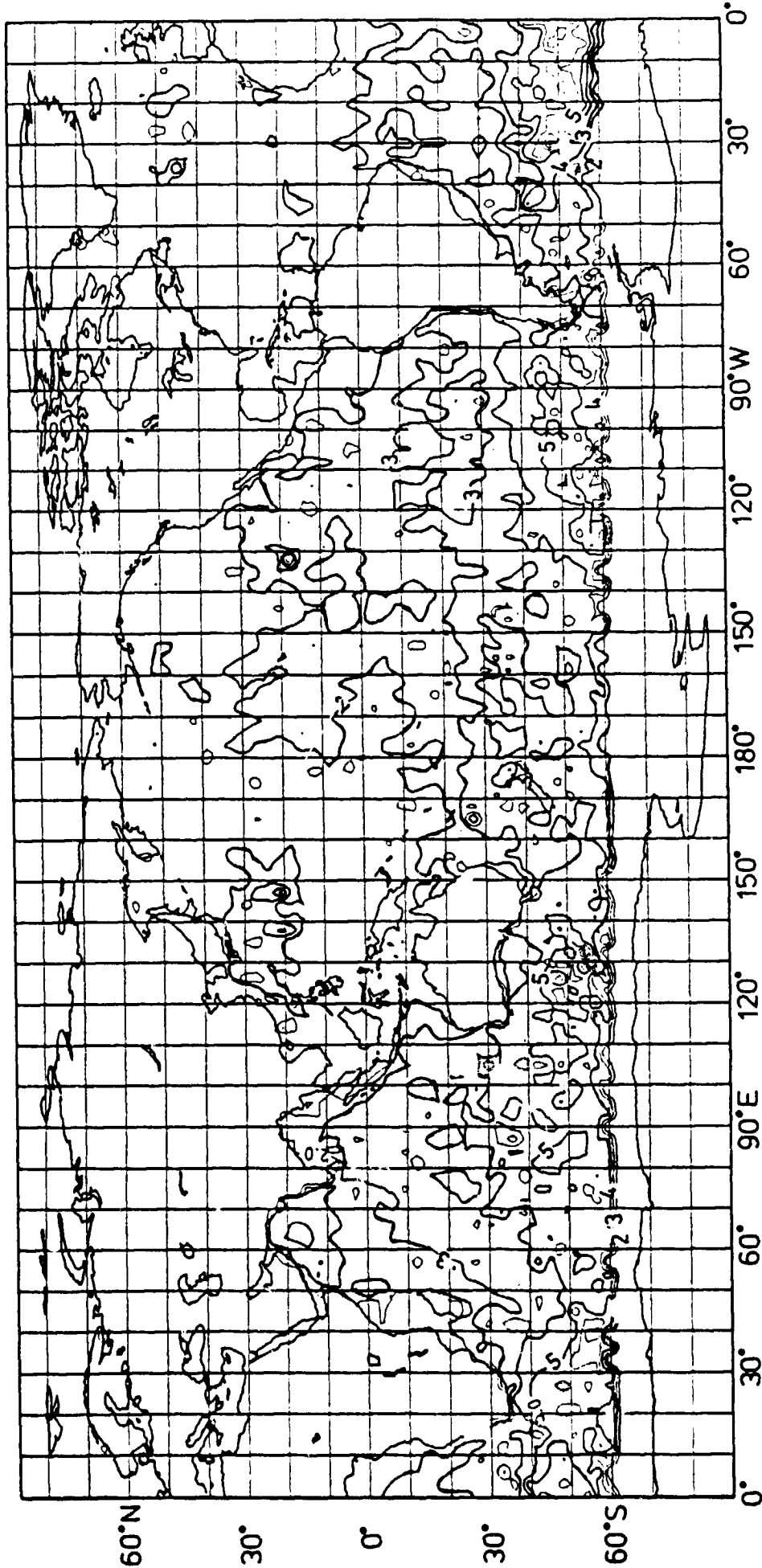
Fig 2 5 a

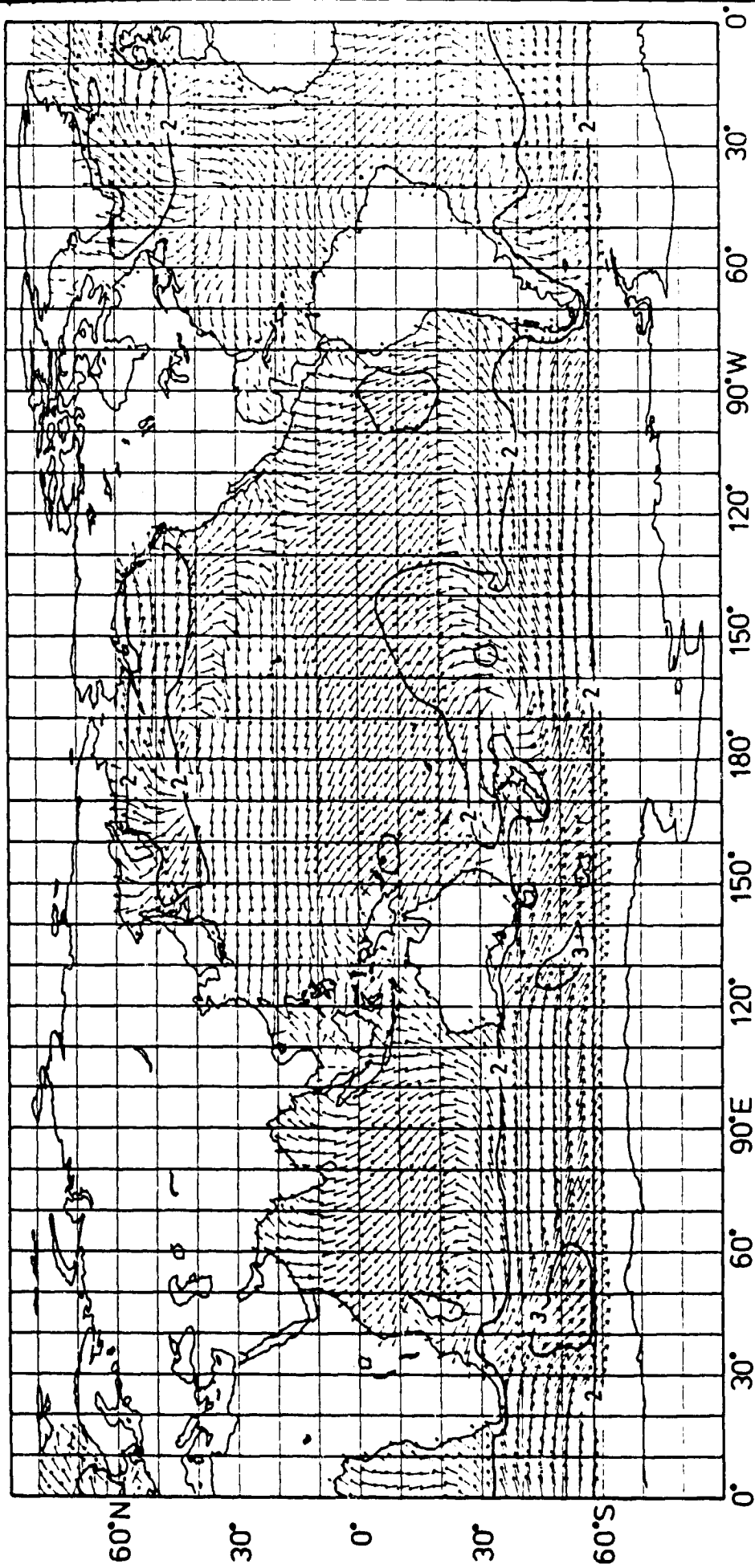Significant wave heights derived from the SEASAT altimeter for July 1978
(averaging periods are given in Table 1)

Fig 2 5 b    Significant wave heights derived from the SEASAT altimeter for August 1978
(averaging periods are given in Table I)

24
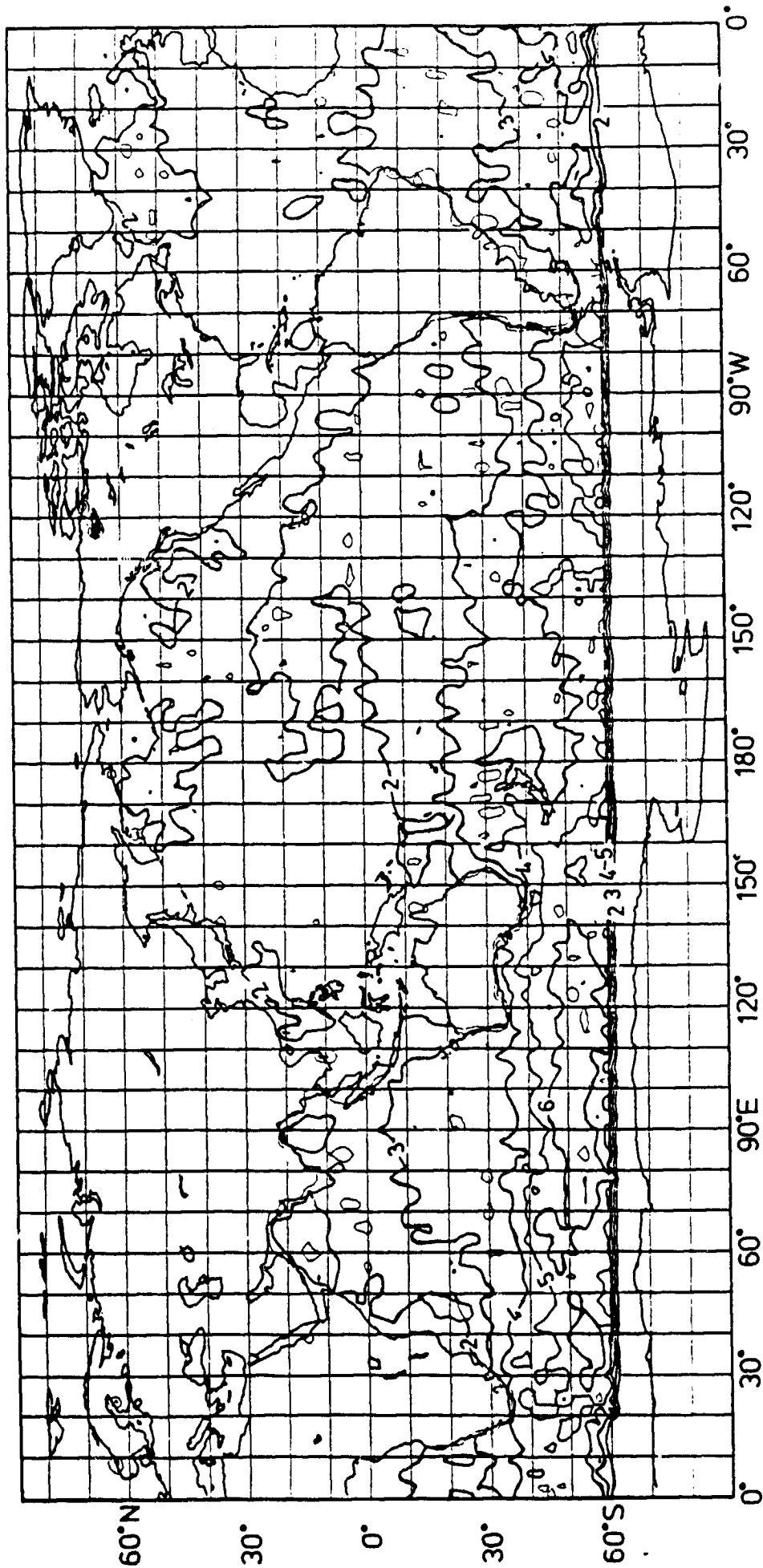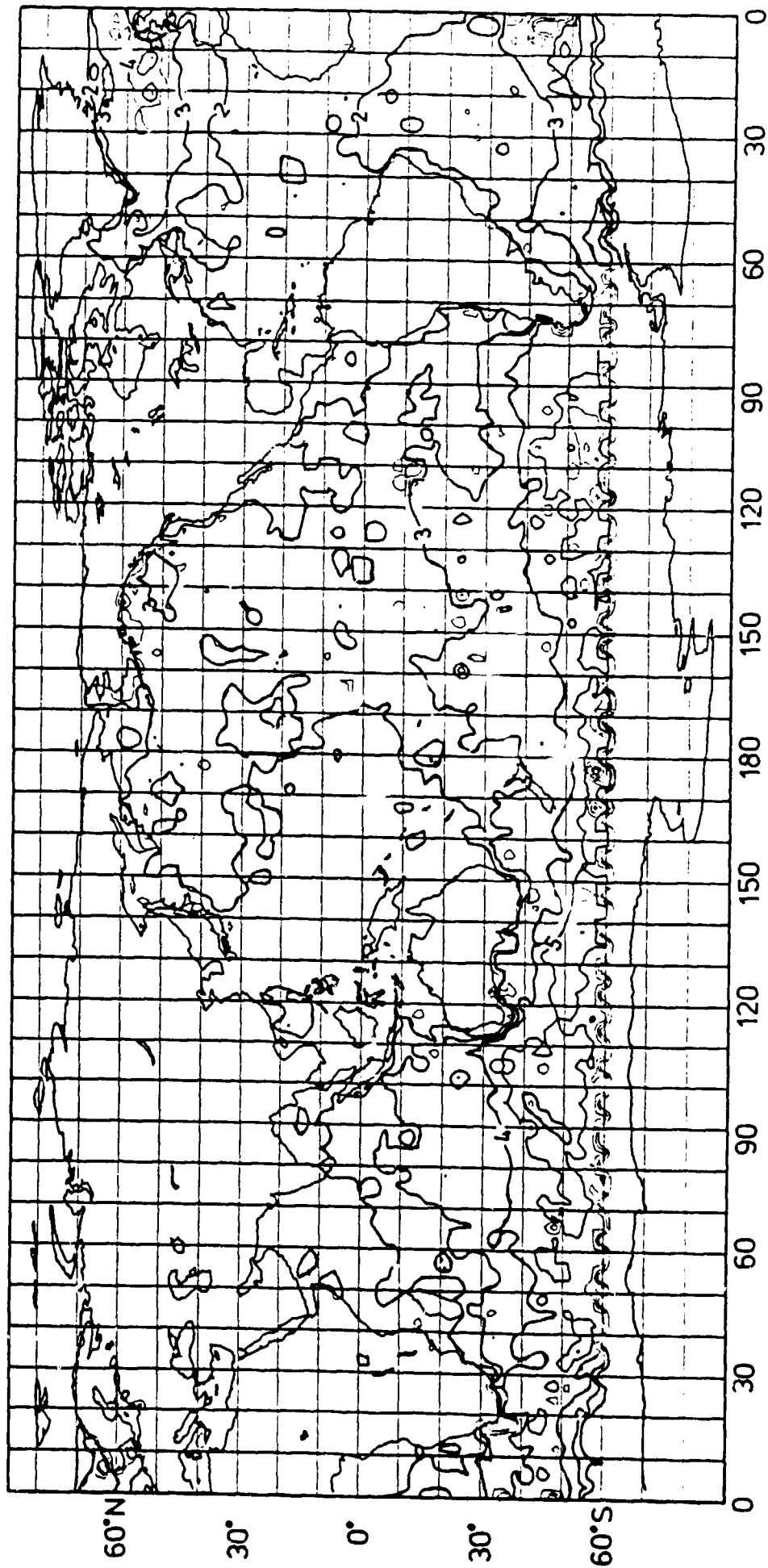
Fig 2.5 c   Significant wave heights derived from the SEASAT altimeter for September 1978 (averaging periods are given in Table 1)

25

The hindcast and altimeter wave heights are seen to agree rather well in the northern hemisphere, but the wave heights are significantly underestimated by the hindcast in the high wind belts of the winter-time southern hemisphere (40°S - 60°S). This is seen more clearly in Fig. 2.6, which shows the ratios of the hindcast to the altimeter wave heights. The causes of these discrepancies will be discussed in more detail in Section 3. However, we point out here already that it appears unlikely that they can be attributed to the altimeter wave height measurement or the wave model, since both have been well verified under rather high wind conditions. The problem therefore presumably lies in the surface stress field. The wave height underestimate corresponds to an underestimation of the wind stress by approximately 20 - 30 %. This example clearly demonstrates the advantage of operating a wave model in conjunction with a wind data assimilation system. The wave model provides a valuable cross validation of two sensor systems, the scatterometer wind measurement and the altimeter wave height, in this case revealing an inconsistency of the assimilated stress field in a climatically important region of the globe in which very few other independent measurements exist.

Figs 2.2 - 2.4 illustrate an interesting property of open ocean surface waves which is familiar to ocean wave researchers but is perhaps less widely known otherwise: most of the wave energy in the open ocean, even in the high wind belts, is associated with swell, the windsea energy being concentrated locally in relatively small regions of high winds. This is due to the fact that swell can propagate for a few weeks over many thousands of km in the ocean without significant dissipation (cf. Snodgrass et al., 1966), so that the windsea energy generated in rather short lived storm events is retained for a long time by the ocean as swell.

The concentration of the windsea energy in local regions is less apparent in the monthly averaged data in Fig. 2.3 than in the instantaneous wave height distribution, an example of which is shown in Fig. 2.7, together with the instantaneous surface stress field, for August 19, 1978, 00:00 GTM.

The fact, that most of the wave energy in the open ocean is associated with swell rather than windsea is an advantage for the assimilation of wave data in a wave forecast model. A swell field, once corrected by a measurement update, propagates from then onwards in the model at its corrected value, while a windsea update relaxes back to the original incorrect value unless the wind field is also properly corrected at the same time (see Section 5).
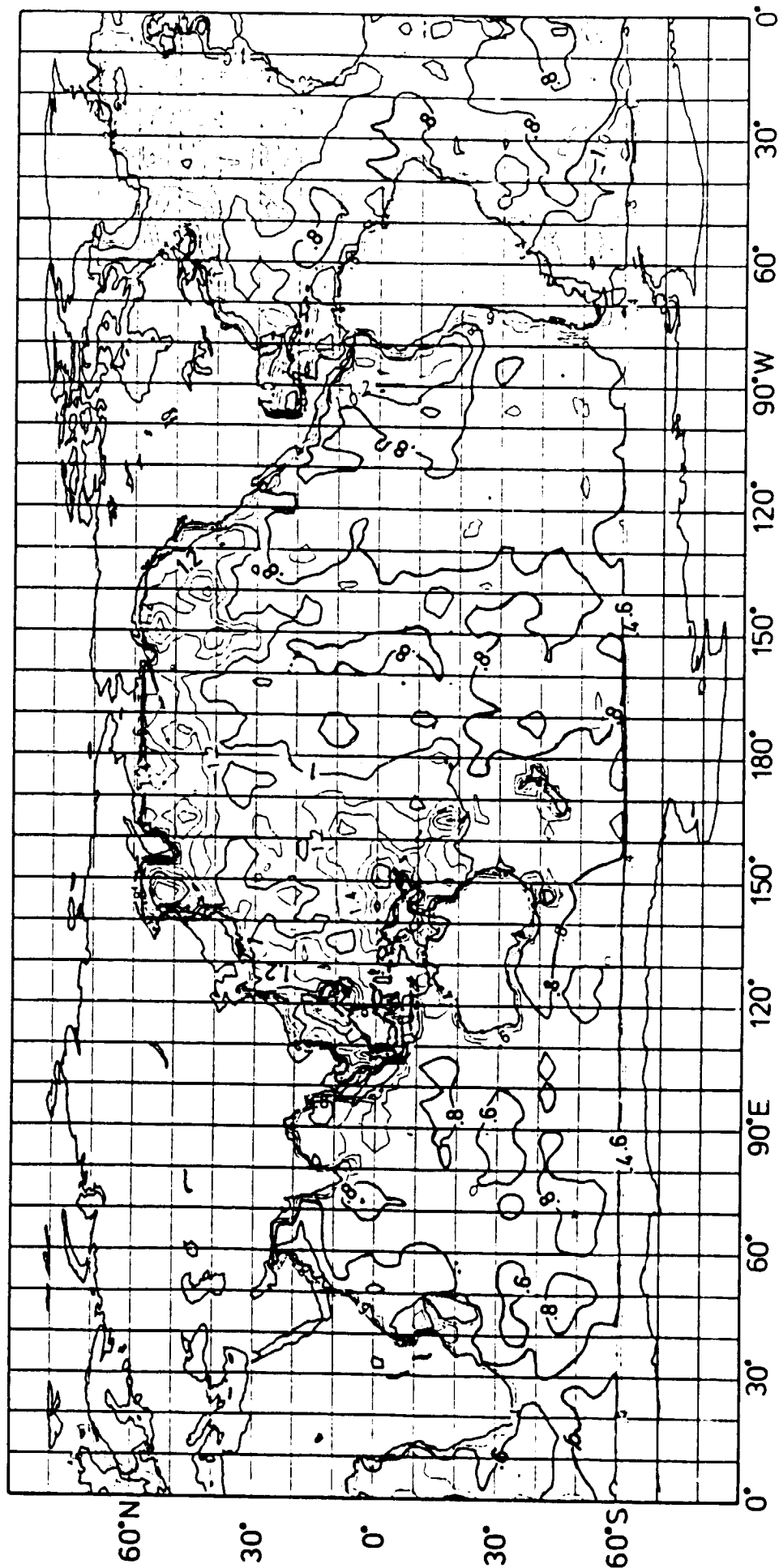
Fig 2 6 a    Ratio of model hindcast significant wave height (cf Fig 2 2) to altimeter
wave height (cf Fig 2 5) for July 1978
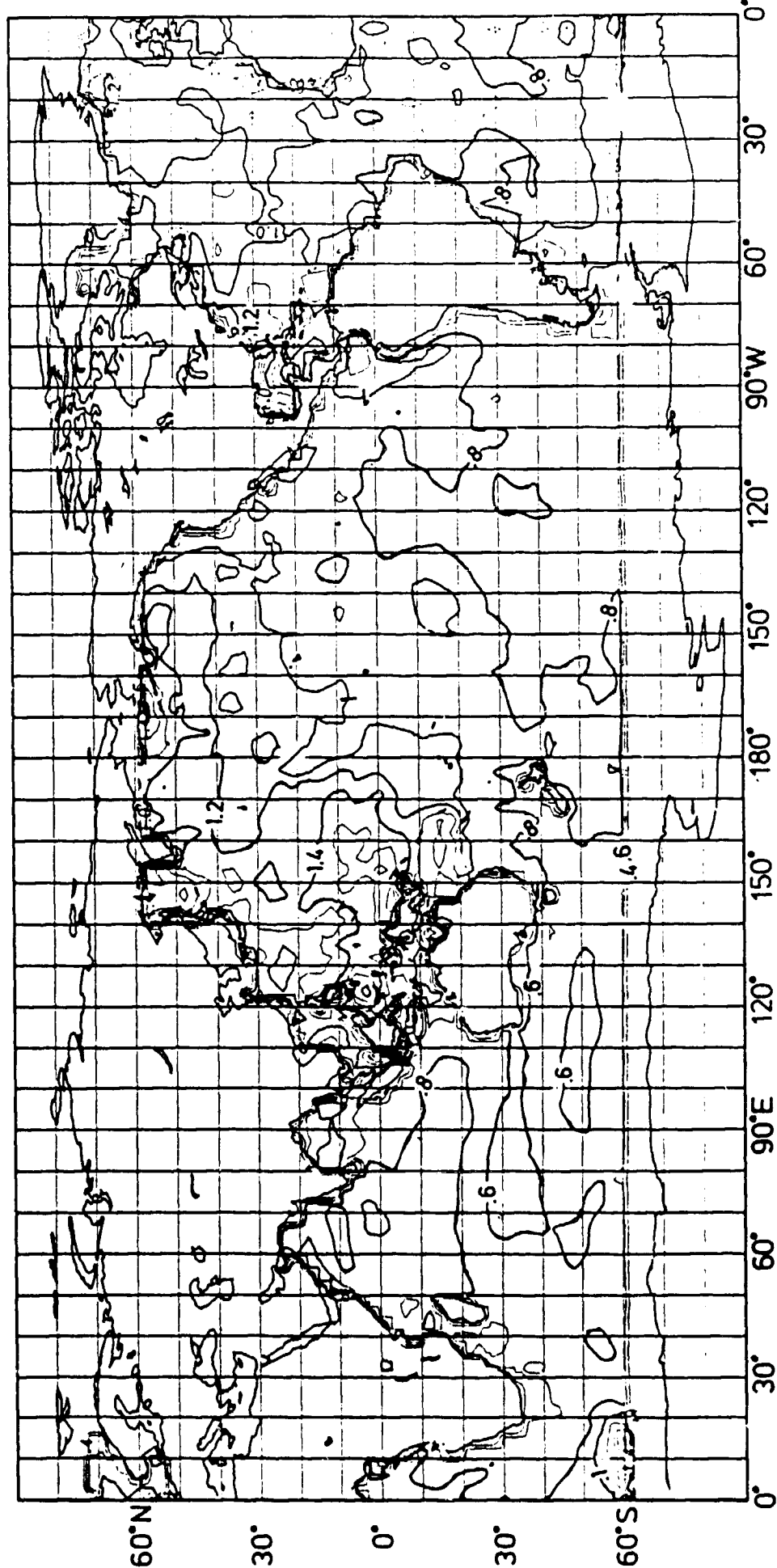
27

Fig 2 6 b      Ratio of model hindcast significant wave height (cf. Fig 2 2) to altimeter
wave height (cf Fig 2 5) for August 1978

28

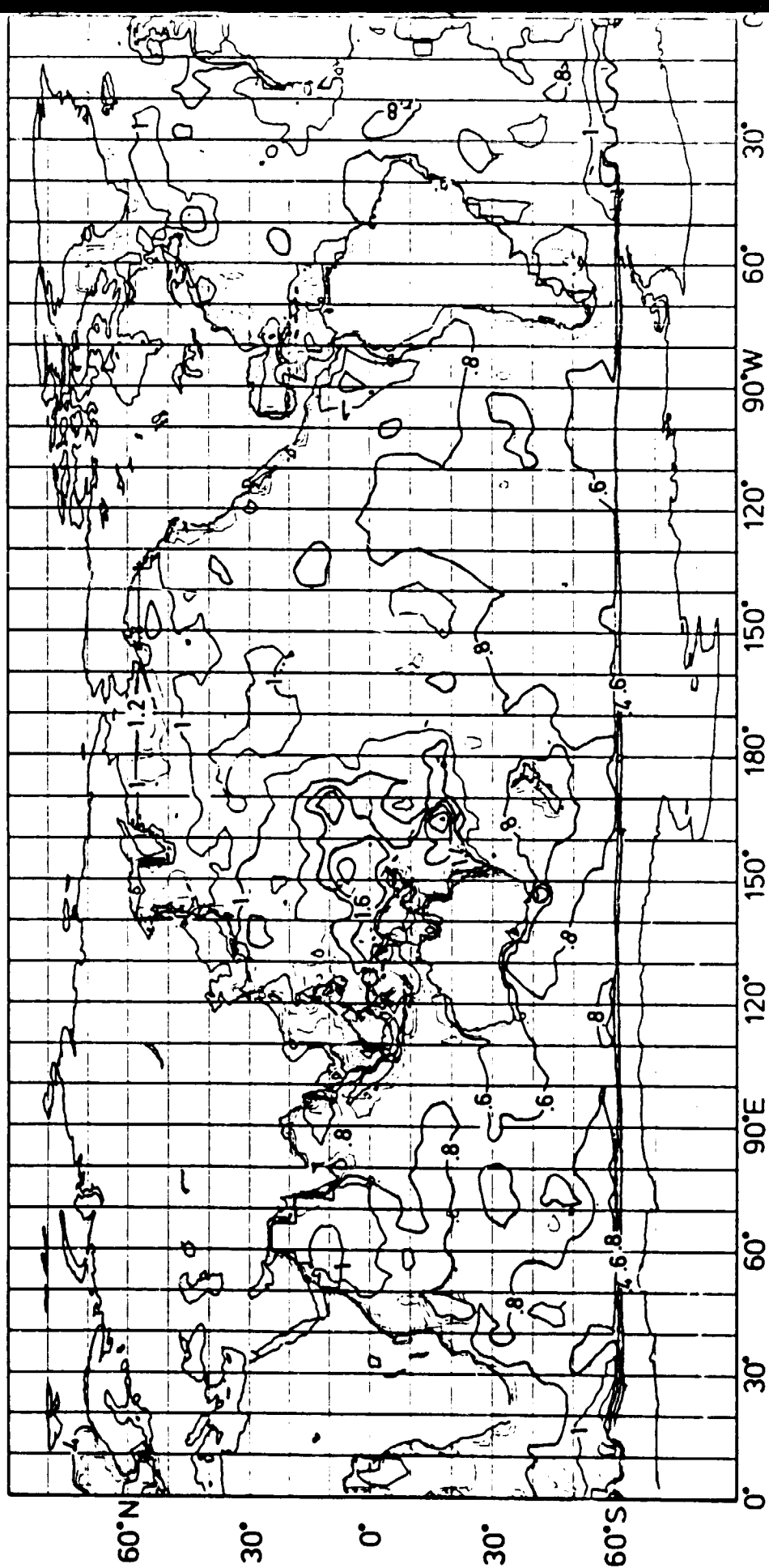Fig 2 6c    Ratio of model hindcast significant wave height (cf Fig 2 2) to altimeter
wave height (cf Fig 2 5) for September 1978
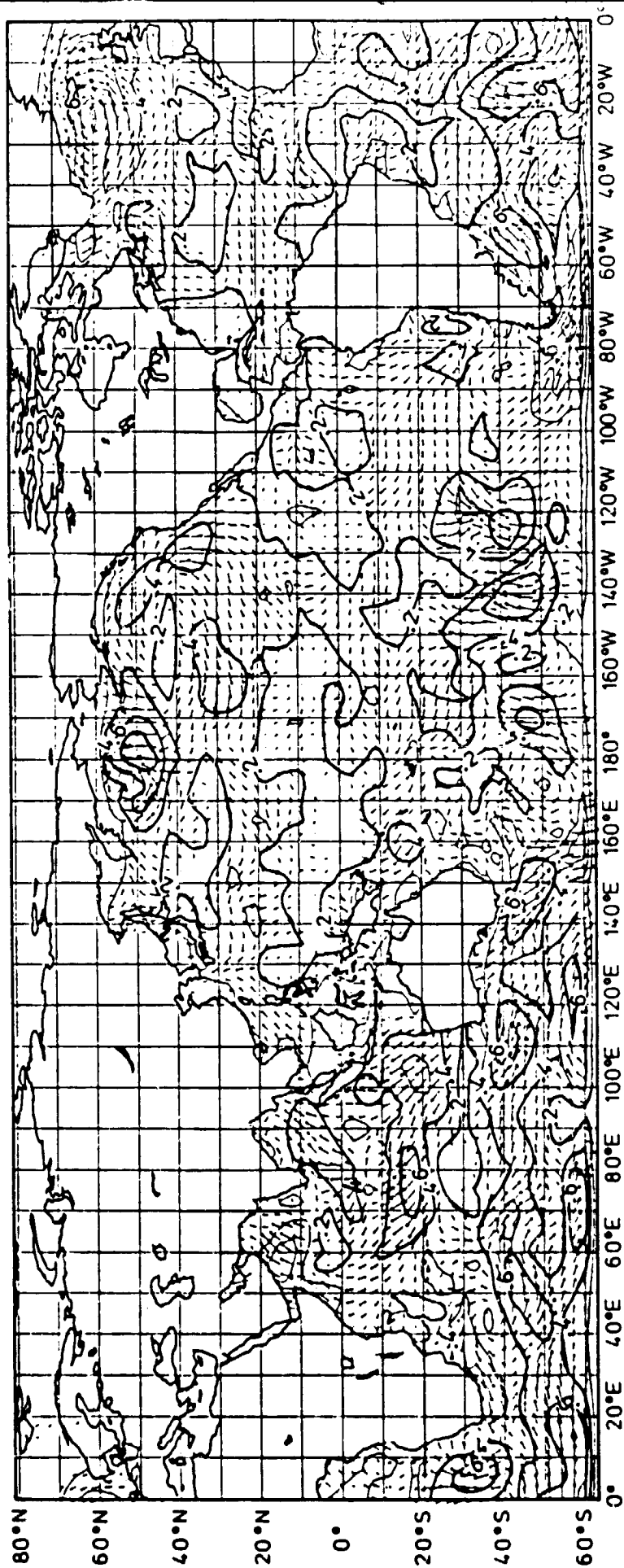
Fig 2 7 a    Surface stress fields for August 19, 1978, 00 00 GMT
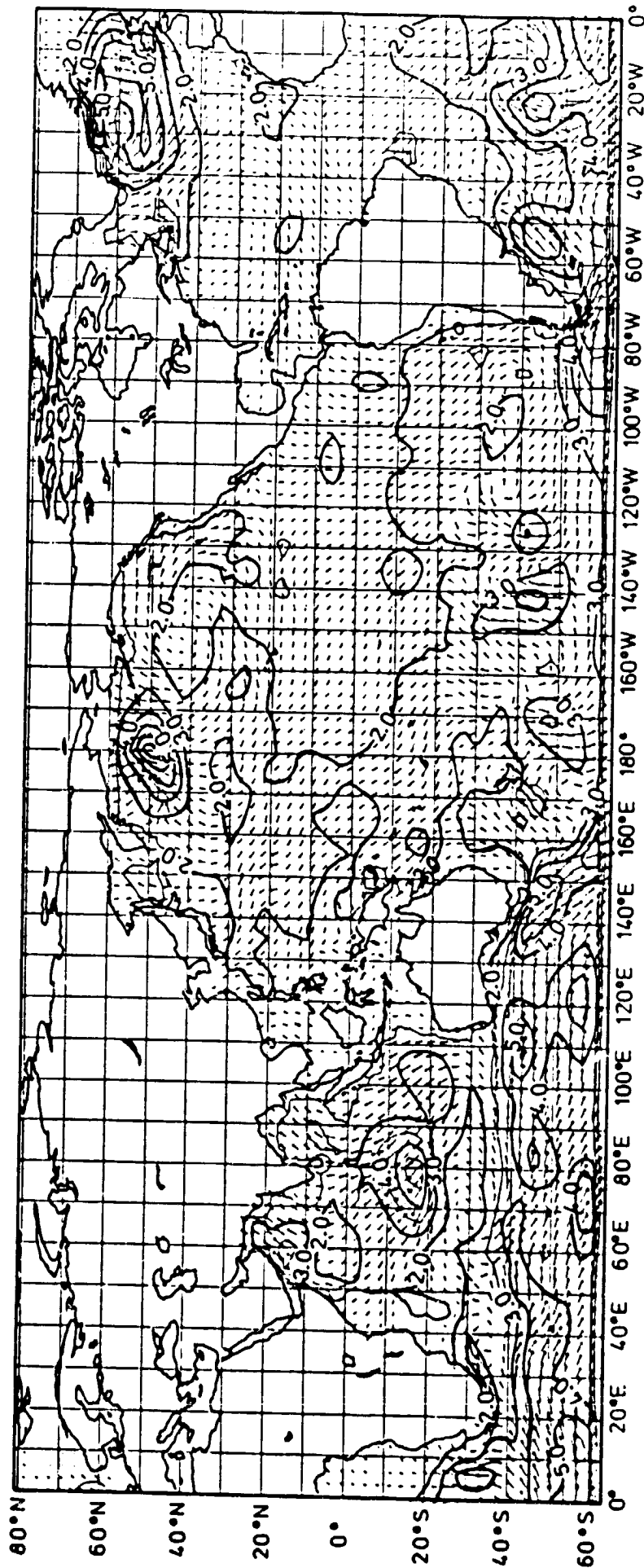
30

Fig 2 7 b      Significant wave height and mean direction fields for August 19 1978
               00:00 GMT

31
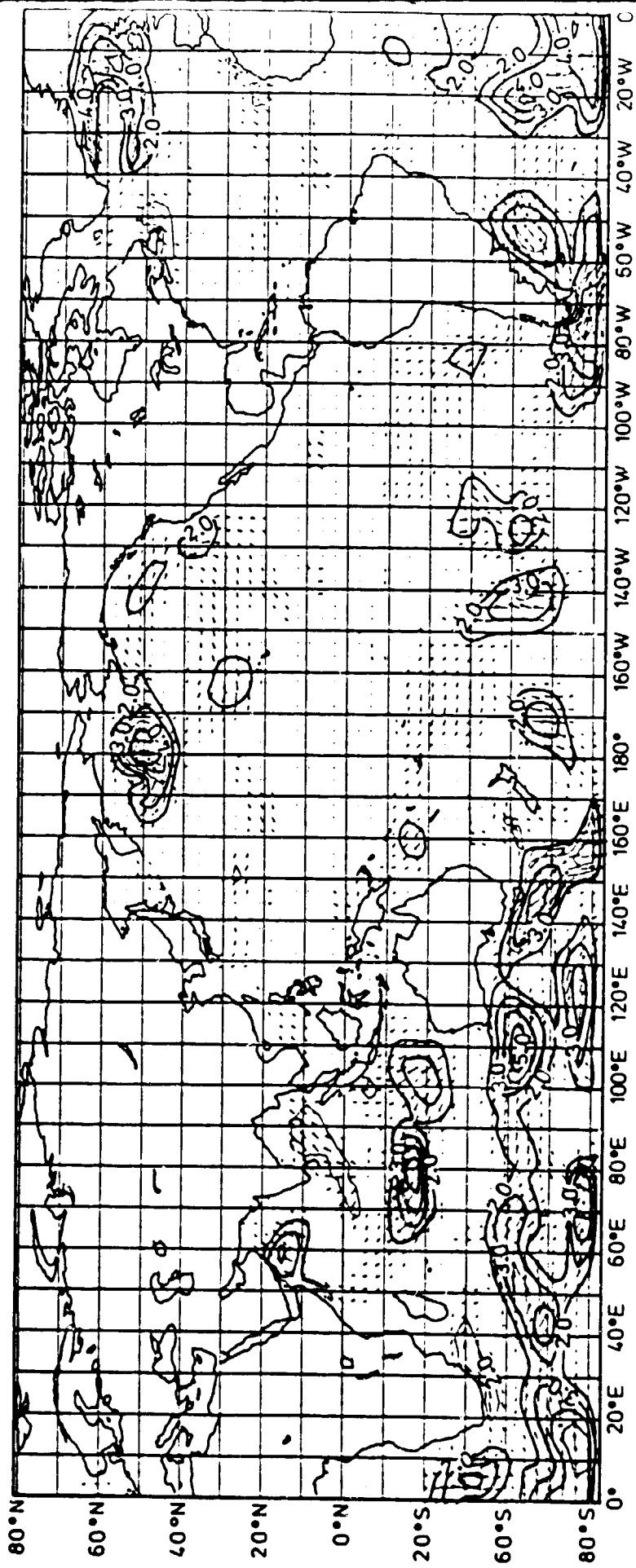
Fig 27c          Windsea for August 19, 1978, 00 00 GMT

32
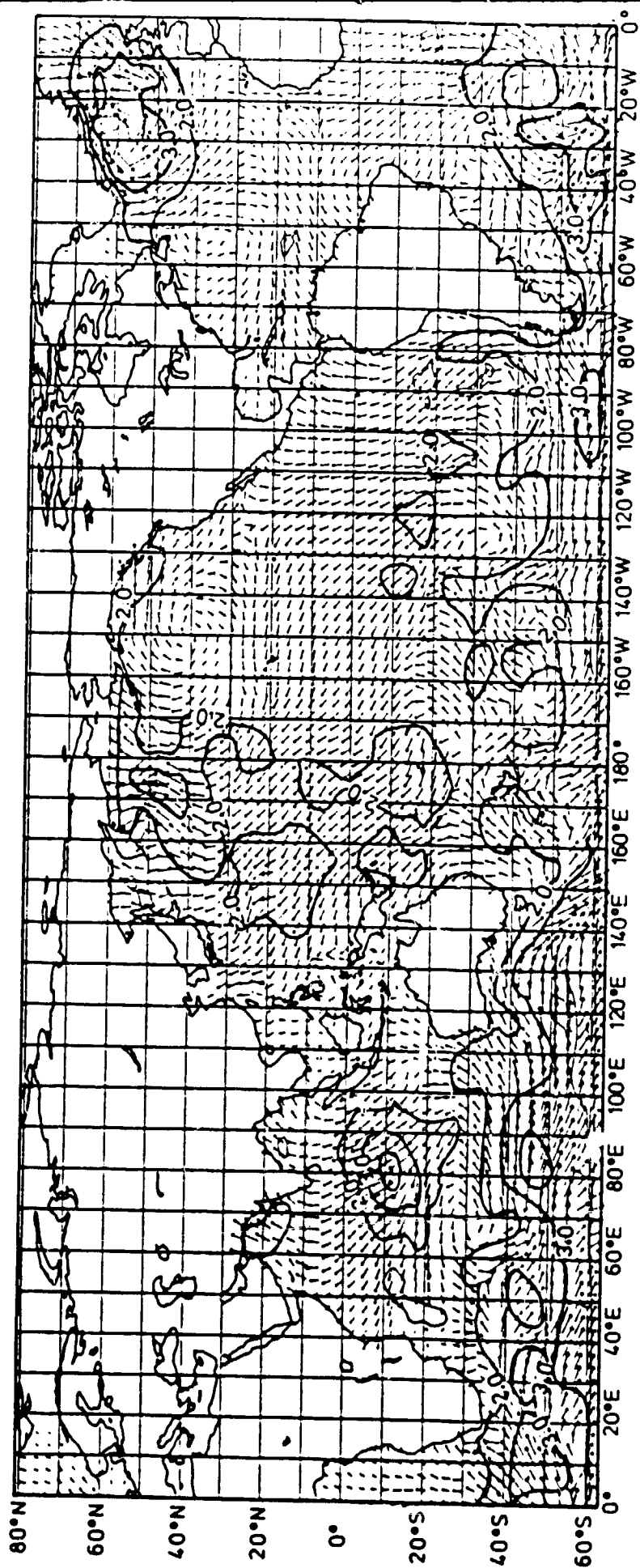
Fig 2 7 d    Swell for August 19, 1978, 00 00 GMT

33

## 2.2 Statistical comparison with altimeter wave height data

The above comparison of the averaged global fields of wave heights was comple-
mented by a more detailed statistical intercomparison. A linear regression analysis
was carried out between the model hindcast and altimeter wave height for a set of
8 periods of 10 to 11 days covering the time span of the experiment (cf. Table 2)

In the standard regression analysis for a set of pairs of variables $x_i, y_i, i = 1, \ldots N$,
the regression coefficient $c$ in the linear relation

$$y_i = cx_i \tag{2.2}$$

is determined by minimizing the average error $< y - cx^2 >$ with respect to the $y$
coordinate, where

$$< \ldots > = \frac{1}{N} \sum_{i=1}^{N} \ldots$$

One obtains then the regression coefficient

$$c_y = \frac{<xy>}{<x^2>} \tag{2.3}$$

(We have left out the optional additive constant in (2.2), as we are interested in the
mean factor relating the two variables.)

One can, of course, equally well interchange $x$ and $y$, minimizing the error
$<(x - y/c)^2>$ with respect to the $x$ coordinate. This yields the regression coefficient

$$c_x = \frac{<y^2>}{<xy>} \tag{2.4}$$

The two estimates satisfy the inequality

$$c_y \leq c_x \tag{2.5}$$

since

$$\frac{c_y}{c_x} = \frac{<xy>^2}{<x^2><y^2>} = r^2 \leq 1$$

34

where $r$ represents the correlation coefficient (defined here without subtraction of the means, consistent with the similar definition of the regression line slope (2.2) without an additive constant).

The regression coefficient may also be defined symmetrically by the relation

$$\bar{c} = (c_r c_y)^{\frac{1}{2}} = \left( \frac{<y^2>}{<x^2>} \right)^{\frac{1}{2}} \tag{2.6}$$

We will adopt this definition in the following. The asymmetrical regression coefficients $c_r$, $c_y$ may be determined from $c$ and the (similarly symmetrical) correlation coefficient $r$ through the relations

$$c_y = \bar{c} \cdot r \tag{2.7}$$

$$c_x = \bar{c} / r \tag{2.8}$$

Fig 2.8 shows the regression coefficients $\bar{c}$ and correlations $r$ for the 8 periods listed in Table 2, subdivided into three regions: the northern hemisphere ($2^\circ$ N to $70^\circ$ N), the southern hemisphere ($70^\circ$ S to $2^\circ$ S) and the tropics (between $22^\circ$ N and $22^\circ$ S). The abscissa axis represents the mean altimeter wave height in the relevant region for each of the averaging periods.

The statistical analysis confirms quantitatively the general impression gained already from Figs 2.2 - 2.5: the model hindcast is reasonably consistent with the altimeter wave height data in the northern hemisphere, but produces wave heights which are too low in the southern hemisphere by a factor of order 0.6 - 0.7, the bias increasing with wave height. Fig 2.9 gives an example of a typical scatter diagram of $H_s$ (hindcast) vs. $H_s$ (altimeter) from which the regression and correlation coefficients were derived. One data point represents an average over one day.
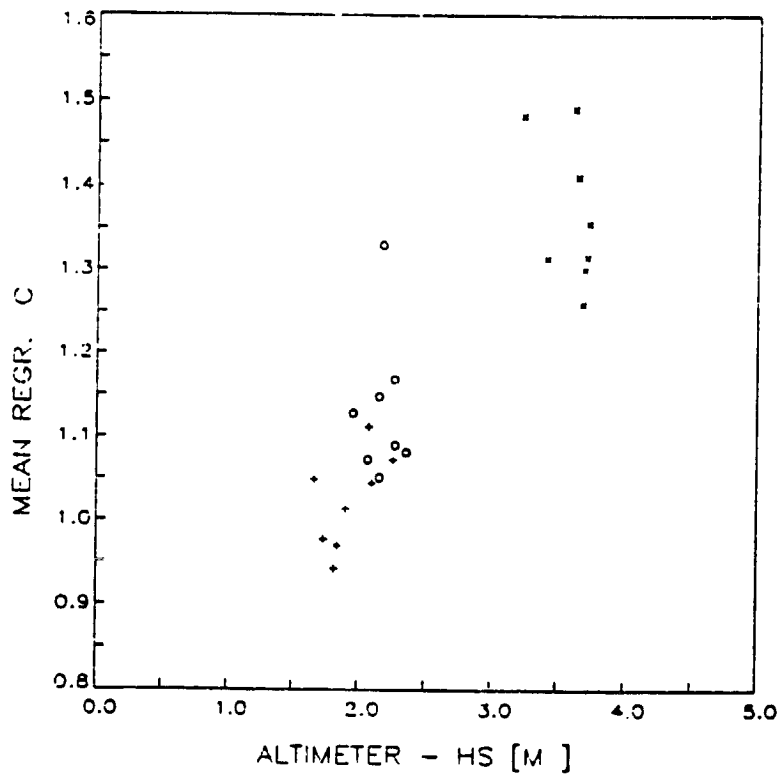
(a)
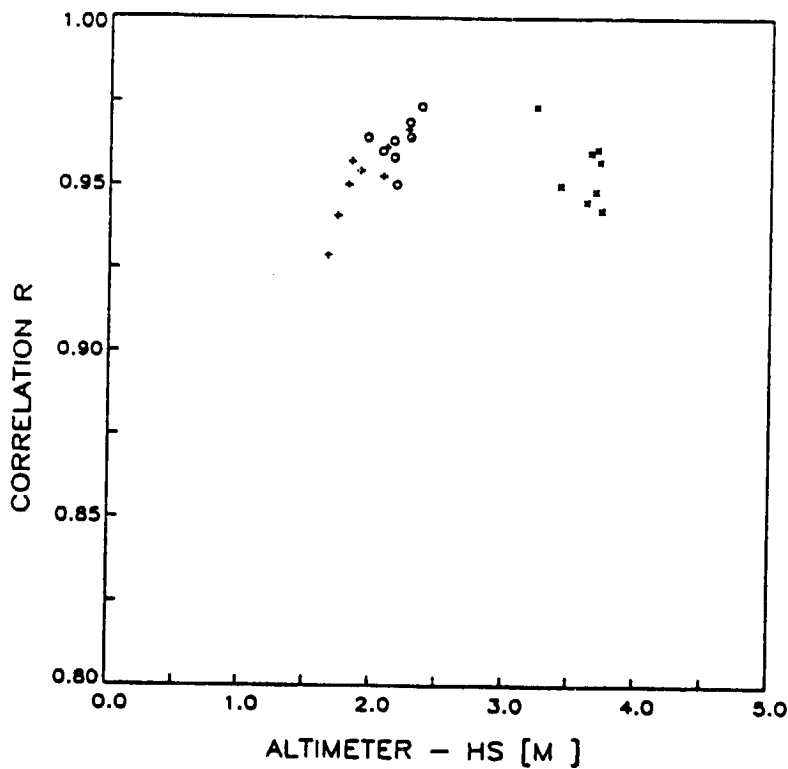


(b)

Fig. 2.8    Regression coefficients (panel (a)) and correlations (panel (b)) for regression analysis hindcast vs. altimeter wave height for the eight averaging periods listed in Table 2.
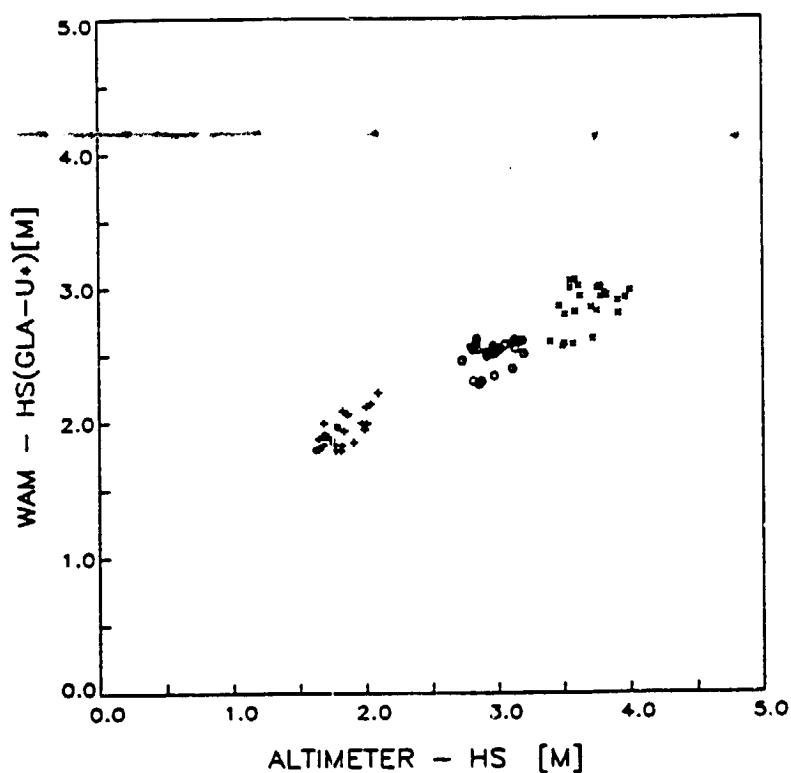
**Fig. 2.9**      Typical scatter diagram for $H_s$ (altimeter) v $H_s$ (hindcast) for one of the eight averaging periods listed in Table 2 (August 1, 1978, 00:00 - August 28, 1978, 00:00).

| | | | |
|---|---|---|---|
| 1) | 78071000 | - | 78072000 |
| 2) | 78072000 | - | 78080100 |
| 3) | 78080100 | - | 78081100 |
| 4) | 78081100 | - | 78082100 |
| 5) | 78082100 | - | 78090100 |
| 6) | 78090100 | - | 78091100 |
| 7) | 78091100 | - | 78092100 |
| 8) | 78092100 | - | 78100102 |

Table 2: Averaging periods used for the regression
analysis of altimeter vs. model data
($H_s$ and wind speed).

## 2.3   Regional comparison with wave buoys and altimeter data

At six NODC buoy locations in the North Pacific (4) and North Atlantic (2) (cf. Fig. 2.10) three-way inter-comparisons were made between the wind and wave data of the model hindcast, the altimeter and the wave buoys. The data from three sources were brought into a comparable format as follows:

Model hindcast: The values of each model parameter (friction velocity $u_*$, significant wave height $H_s$, mean frequency $\bar{f}$, mean direction $\bar{\theta}$) was determined from a weighted average, where the weights correspond to the inverse distance between the grid point and buoy location. Close to land boundaries, only three or two grid points were used.

Buoy: From the spectral data, $H_s$ and the mean frequency $\bar{f}$ were recalculated including an $f^{-4}$ tail in the same manner as in the WAM model (cf. WAMDIG, 1988). The wind velocity was reduced to 10 m winds if necessary and then converted to $u_*$ values by applying the expressions given in WAMDIG (1988). In order to determine a suitable averaging time for the buoy data, which was available every three hours, the correlation coefficients were computed for all variables using the actual buoy values at model output times for noon and midnight, then the values at 3 hours before, at, and 3 hours after the model output times, 6 hours before, ... etc., up to an averaging time of one day. Plots of the correlation coefficients revealed that the optimum averaging time was around 12 hours, where correlation coefficients typically peaked around 0.6 - 0.8 depending on the variable. This result is consistent with the averaging incurred by the model, since the energy of a 10 second wave propagating at its group velocity would take about 12 hours to travel a distance of 3 degrees, the grid resolution in the model.

Altimeter. The altimeter data set co-located with the buoys was determined by averaging values of $H_s$ and $u_*$ over five values (~ 70 km track length) along the altimeter track which was closest to the buoy and within a three hour time window of the buoy measurement. Altimeter wind speeds were reduced to 10 m winds and then converted to $u_*$ as described above. Extreme values in $H_s$ were deleted from the data set.

Tables 3 and 4 summarize the principal statistics (the bias is the mean of the difference between the first and second variables, the scatter index $SI$ the ratio of the rms differences between model parameters and observations to the mean of the observations (in %)). In general, the agreement between the model hindcast and

buoy data is comparable with the agreement between the altimeter and the buoys. The open ocean stations in the N. Pacific (e.g. buoy 46006, cf. Fig. 2.12) generally show better agreement than the stations closer to shore (e.g. buoy 41001, Fig. 2.11), for which the 300 km model resolution was presumably insufficient. A comparison of the friction velocity and wave height time series in Figs 2.11 and 2.12 suggests that much of the discrepancy between the different instruments can be attributed to local, relatively short-lived wind events which, on the one hand, are not adequately resolved by the altimeter and model and which, on the other hand, are not representatively sampled by a point measurement. Although the general consistency of the intercomparison gives support to all three measurement systems, the scatter is nevertheless greater than is typically found in model-measurement intercomparisons involving either larger averaging areas (cf. Section 3, for example) or point measurements accompanied by a higher resolution determination of the surrounding wind field (cf. hurricane and North Sea hindcast studies discussed in WAMDIG, 1988)

From the viewpoint of an optimal measurement strategy for the validation and calibration of ERS-1 during the initial commissionary phase, as well as the long term monitoring of the satellite sensor system, we therefore recommend giving higher priority to (i) global verification methods, based on combined scatterometer, altimeter, and SAR wave mode data, as outlined in Sections 2.1, 2.2, 3 and 5, and (ii) measurement campaigns, in which in situ measurement stations are deployed in arrays, rather than as single stations. However, where available, long term single station buoy measurements can nevertheless usefully augment these other approaches.

| Variable | Models vs. Buoy (707 observations) | | | | Buoys vs. Altimeter (386 observations) | | | | Model vs. Altimeter (69 observations) | | | |
|---|---|---|---|---|---|---|---|---|---|---|---|---|
| | AVE | Bias | σ | SI | AVE | Bias | σ | SI | AVE | Bias | σ | SI |
| $u_*$ (m/s) | 0.24 | 0.036 | 0.115 | 48.7 | 0.24 | 0.000 | 0.089 | 37.9 | 0.22 | 0.018 | 0.106 | 48.6 |
| Hs(m) | 1.63 | 0.323 | 0.596 | 36.7 | 1.65 | 0.353 | 0.550 | 33.4 | 1.60 | -0.098 | 0.655 | 41.0 |
| f(Hz) | 0.14 | 0.012 | 0.032 | 23.1 | | | | | | | | |
| θ(°) | 98.79 | 9.356 | 48.589 | 49.2 | | | | | | | | |

**Table 3** Statistics of three way intercomparisons for all buoy stations

| Variable | BUOY 44004 38°42'N 286°24'E (102 observations) | | | | BUOY 46008 57°06'N 208°18'E (114 observations) | | | | BUOY 41001 35°N 288°E (145 observations) | | | |
|---|---|---|---|---|---|---|---|---|---|---|---|---|
| | AVE | Bias | σ | SI | AVE | Bias | σ | SI | AVE | Bias | σ | SI |
| $u_*$ (m/s) | 0.27 | -0.016 | 0.100 | 36.7 | 0.16 | 0.156 | 0.116 | 74.0 | 0.22 | 0.003 | 0.097 | 44.9 |
| Hs(m) | 1.62 | -0.190 | 0.502 | 31.1 | 1.58 | 0.770 | 0.530 | 33.5 | 1.37 | -0.060 | 0.383 | 28.0 |
| f(Hz) | 0.11 | 0.058 | 0.020 | 17.9 | 0.17 | 0.025 | 0.030 | 17.7 | 0.17 | 0.001 | 0.023 | 13.3 |
| θ (°) | 162.09 | 17.522 | 32.038 | 19.8 | 110.12 | 9.239 | 58.174 | 52.8 | 215.09 | 12.175 | 64.269 | 29.9 |

**Table 4** Statistics of model vs buoy intercomparisons for individual buoys (to be continued next page)

| Variable | BUOY 46001 56°N 212°E (56 observations) | | | | BUOY 46005 46°N 229°E (145 observations) | | | | BUOY 46006 41°N 222°E (145 observations) | | | |
|---|---|---|---|---|---|---|---|---|---|---|---|---|
| | AVE | Bias | σ | SI | AVE | Bias | σ | SI | AVE | Bias | σ | SI |
| $u_*$(m/s) | 0.25 | 0.071 | 0.099 | 40.4 | 0.27 | 0.010 | 0.089 | 32.7 | 0.25 | 0.023 | 0.099 | 39.5 |
| Hs(m) | 1.49 | 1.107 | 0.451 | 30.2 | 1.82 | 0.358 | 0.393 | 21.6 | 1.78 | 0.378 | 0.475 | 26.7 |
| f(Hz) | 0.12 | 0.011 | 0.021 | 16.8 | 0.13 | 0.013 | 0.014 | 11.4 | 0.12 | 0.022 | 0.015 | 12.6 |
| θ(°) | 284.44 | 10.562 | 35.447 | 12.5 | 79.53 | 12.280 | 30.697 | 38.6 | 93.36 | 15.386 | 34.090 | 36.5 |

**Table 4** Statistics of model vs buoy intercomparisons for individual buoys (continued from last page)
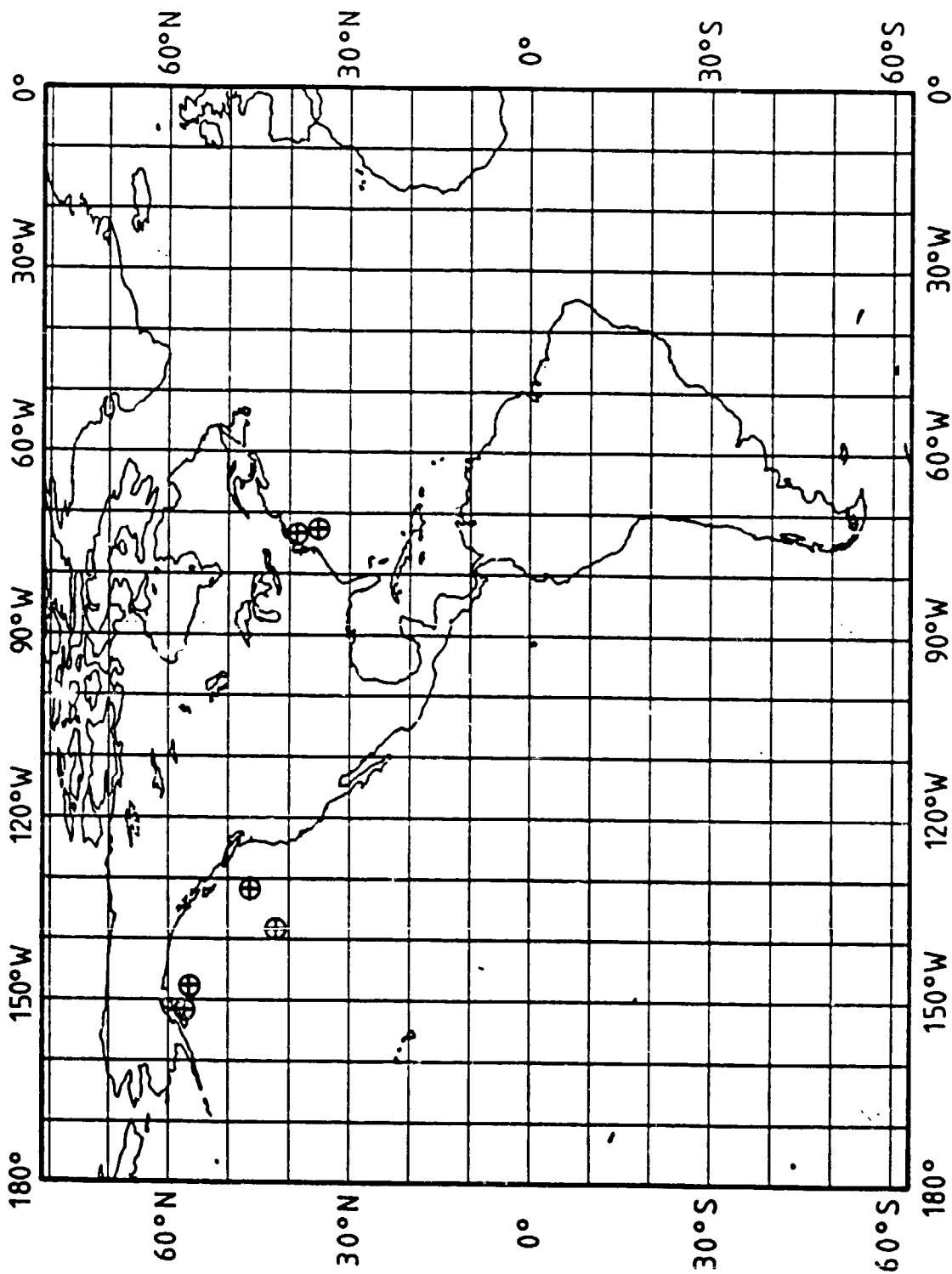
Fig 2 10    Positions of the six NODC buoys used for model hindcast, altimeter and buoy
data intercomparison

44

BUOY 41001 (35 00 N, 288 00 E

ALTIMETER o
MODEL x
BUOY —

FRICTION VELOCITY DIRECTION

FRICTION VELOCITY (M/S)

SIGNIFICANT WAVE HEIGHT (M)

MEAN WAVE FREQUENCY (1/SEC)

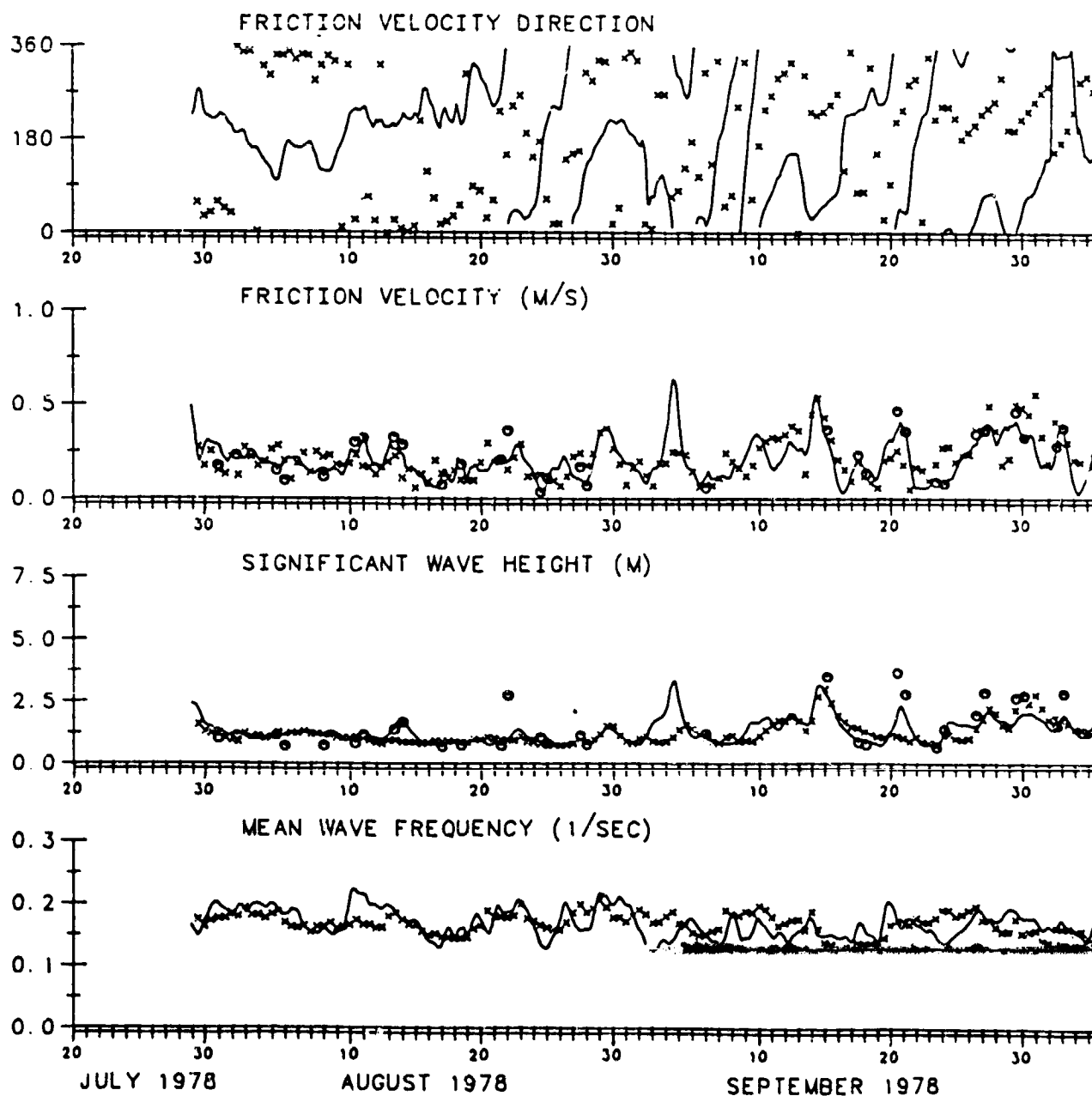JULY 1978        AUGUST 1978        SEPTEMBER 1978

**Fig. 2.11**        Time series wind and wave data from wave hindcast altimeter and wave buoy
at location of buoy 41001 in N. Atlantic (cf. Fig. 2.10)

**BUOY 46006 (41 00 N, 222 00 E)**

ALTIMETER o
MODEL x
BUOY –

FRICTION VELOCITY DIRECTION

FRICTION·VELOCITY (M/S)

SIGNIFICANT WAVE HEIGHT (M)

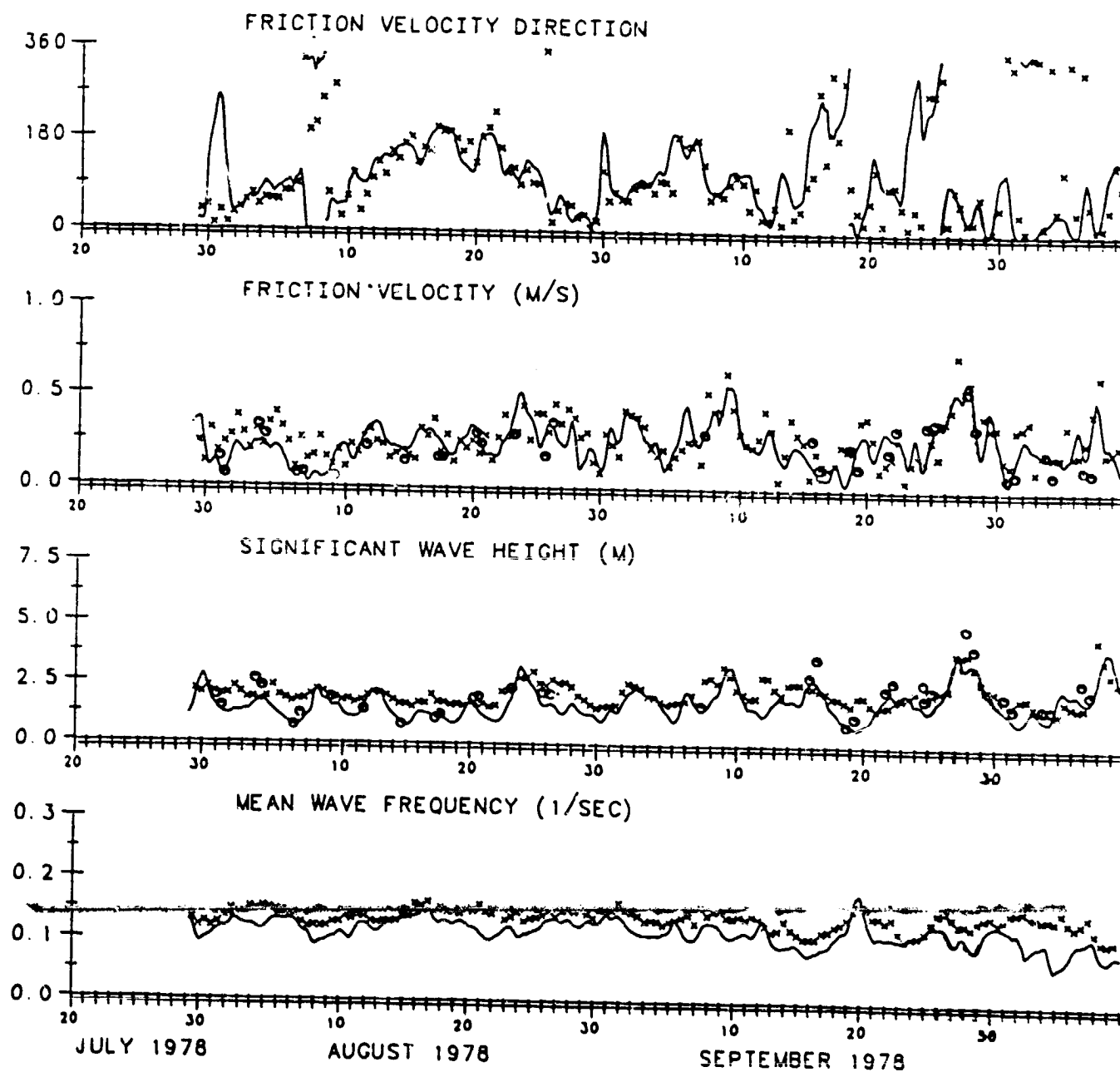MEAN WAVE FREQUENCY (1/SEC)

JULY 1978    AUGUST 1978    SEPTEMBER 1978

Fig. 2.12    Time series wind and wave data from wave hindcast, altimeter and wave buoy at location of buoy 46006 in N. Pacific (cf. Fig 2.10).

46

## 3    Intercomparison of wind fields and wave hindcasts

### 3 1    Intercomparison of GLA surface wind and stress fields with ECMWF and JPL surface wind fields

To determine the possible origins of the discrepancy between the model hindcast wave heights and SEASAT altimeter wave heights in the southern hemisphere, an intercomparison was made between the GLA surface wind and stress fields and two other wind fields which were available for sub-periods of the 96-day hindcast period - the assimilated ECMWF 1000 mb wind fields for the period September 6 - 17 (Anderson et al., 1987), and the subjectively analyzed JPL 19 5 m height wind fields for the period September 7 - 20 (Woiceshyn et al, 1987)  Details of the wind and stress data sets are given in Table 5

In the following two sub-sections we consider first the intercomparison for the three wind field data sets and then the GLA stress wind field intercomparison  It was found that the main problem appears to lie in the GLA southern hemisphere stress field analysis, while the three wind field products are reasonably consistent for all regions of the globe  This finding is borne out by the intercomparison of the three wave hindcasts for the period of common overlap discussed in Section 3 3

All following intercomparisons are expressed in terms of the symmetrized regression coefficient $\tilde{c}$ relating pairs of fields $(x., y)$ in accordance with equ (2 6)

### 3 1 1  Wind field intercomparisons

Table 6 summarizes the results for the three wind field regressions for different pairs of the GLA, ECMWF and JPL wind fields  In addition to the global statistics, data are also given for the northern and southern hemispheres and the tropics  Figs 3 1 - 3 3 show the dependence of $\tilde{c}$ and $r$ on wind speed in each of the three latitudinal belts for each of the three intercomp.      Each  point in these figures corresponds to an average formed for the correspond         a particular analysis time

The principal conclusion to be drawn from these results is that the three wind fields show a surprising level of agreement  the regression coefficient lies close to one for all three intercomparisons in all three regions, and the correlation coefficient is of the order of 90 - 95 % in all cases  It appears that the discrepancies between the

47

aitimeter wave heights and the model wave hindcast in the southern hemisphere shown in Section 2.1 cannot be attributed to the wind field analysis. The problem lies, in fact, in the southern hemisphere GLA stress fields, as shown in the following subsection.

A similar level of agreement is also found in the wind directions. As example, Fig. 3.4a shows the global histogram for the difference in wind direction $\Delta\theta$ between the GLA and ECMWF wind vectors. Most of the errors are less than $20°$. Fig. 3.4b shows the distribution of the mean wind speed and the standard deviation of the wind speed as function of the directional deviation. As to be expected, larger directional deviations are generally associated with weaker wind speeds. Similar results are found for the other two intercomparisons and for the breakdown into the three latitude zones.

### 3.1.2 Intercomparison of GLA surface wind and surface stress fields

To test the consistency of the GLA (1000 mb) surface wind speeds $v$ with the GLA surface stress values $\tau$, a regression analysis was carried out between $v^2$ and $\tau/\rho_a$, where $\rho_a$ denotes the density of air. The regression coefficient $\bar{c}$ then represents an estimate of the average drag coefficient $c_D$. Since the local (temperature dependent) $\rho_a$ values were not available on the GLA data tape, $\rho_a$ was taken as constant ($\rho_a = 1.23 \text{ kg m}^{-3}$)

A problem arose in the assignment of time levels. The wind field analysis at time $t_n$ represents an instantaneous field obtained by combining the first guess wind field provided by the model forecast, derived from the previous analysis time $t_{n-1}$, 6 hours earlier, with conventional atmospheric observations and scatterometer winds at (or close to) the analysis time $t_n$. The surface stress fields, on the other hand, are computed as the average values of the model over the period $t_{n-1}$ to $t_n$. As perhaps to be expected, the best correlations were found between $\tau(t_n)/\rho_a$ and $v^2(t_{n-1})$. This is illustrated in Fig. 3.5, in which the global regression coefficient $\bar{c}$ and correlation $r$ is shown as a function of the lag $\Delta t = t(\tau/\rho_a) - t(v^2)$. The correlations discussed in the following were made for $\Delta t = 6$ hours

48

| Source (wind or stress) units | Grid (lat., long) | Global extension | Time step | Period |
|---|---|---|---|---|
| GLA ($\tau$) in Nm⁻² | 4° × 5° | 90°S - 90°N 180°W - 175°E | 6 hours | 78/07/07 00:00 - 78/10/10 00:00 |
| GLA ($u_{10m}$) in ms⁻¹ | 4° × 5° | 90°S - 90°N 180°W - 175°E | 6 hours | 78/07/07 00:00 - 78/10/10 00:00 |
| JPL ($u_{10m}$) in ms⁻¹ | 1° × 1° | 70°S - 70°N 1°E - 360°E | 6 hours | 78/09/07 12:00 - 78/09/20 00:00 |
| ECMWF ($u_{10m}$) in ms⁻¹ | 1.875° × 1.875° | 90°S - 90°N 0°E - 358°E | 6 hours | 78/09/06 12:00 - 78/09/17 12:00 |

**Table 5** Available wind and stress data sets.

| y-field | x-field | N | $\langle y \rangle \pm \sigma_y$ [ms-1] | $\langle x \rangle \pm \sigma_x$ [ms-1] | r | c |
|---------|---------|------|------------|------------|------|------|
| GLA | JPL | 1540 | 9 06 ± 0 41 | 9 09 ± 0 42 | 0 92 | 1 09 |
| GLA | ECMWF | 1710 | 9 20 ± 0 39 | 9 09 ± 0 54 | 0 93 | 1 01 |
| ECMWF | JPL | 1540 | 9 00 ± 0 56 | 8 46 ± 0 42 | 0 94 | 1 09 |

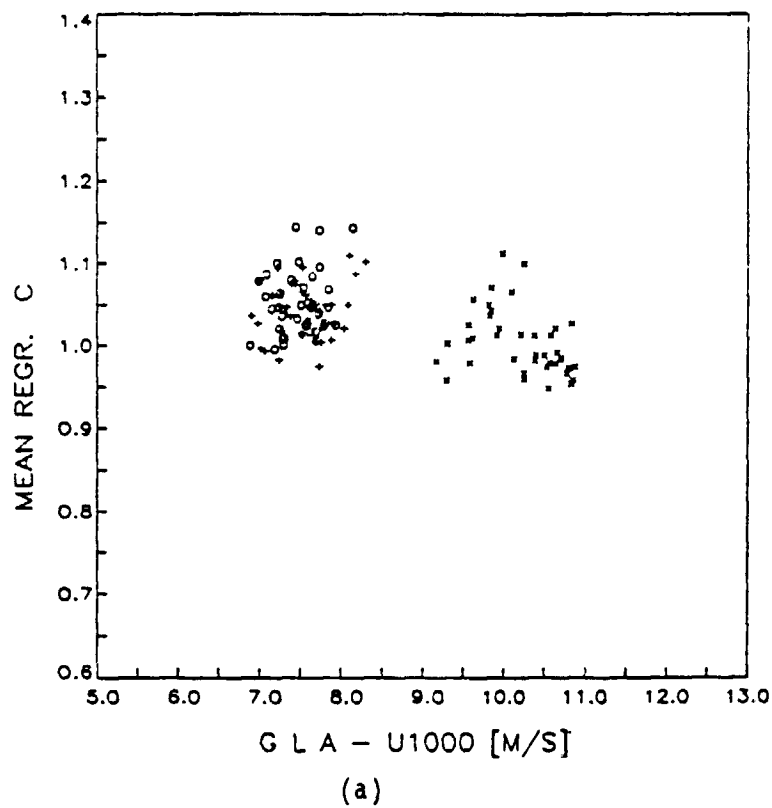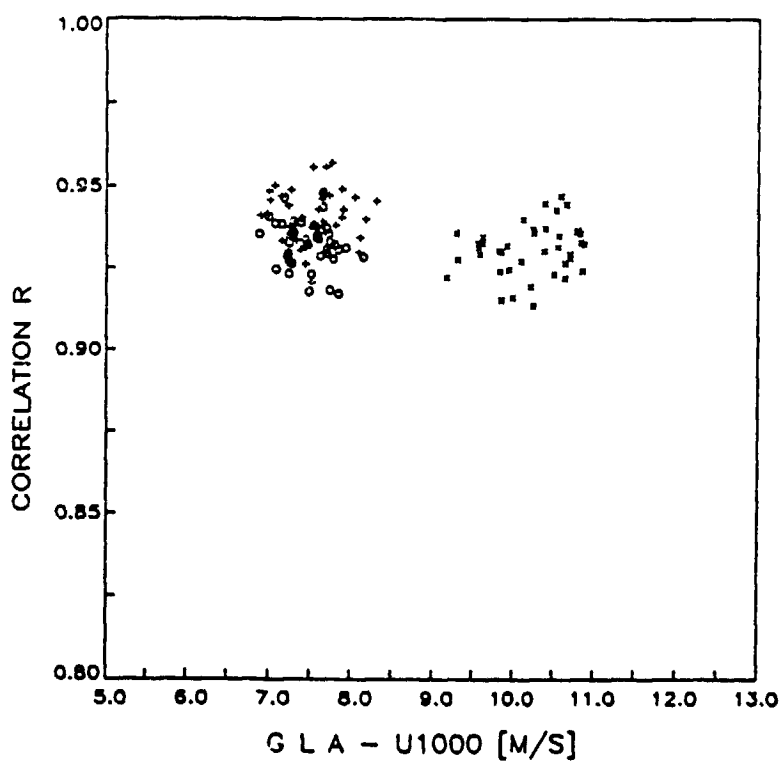**Table 6** Global linear regression analysis between wind velocity fields
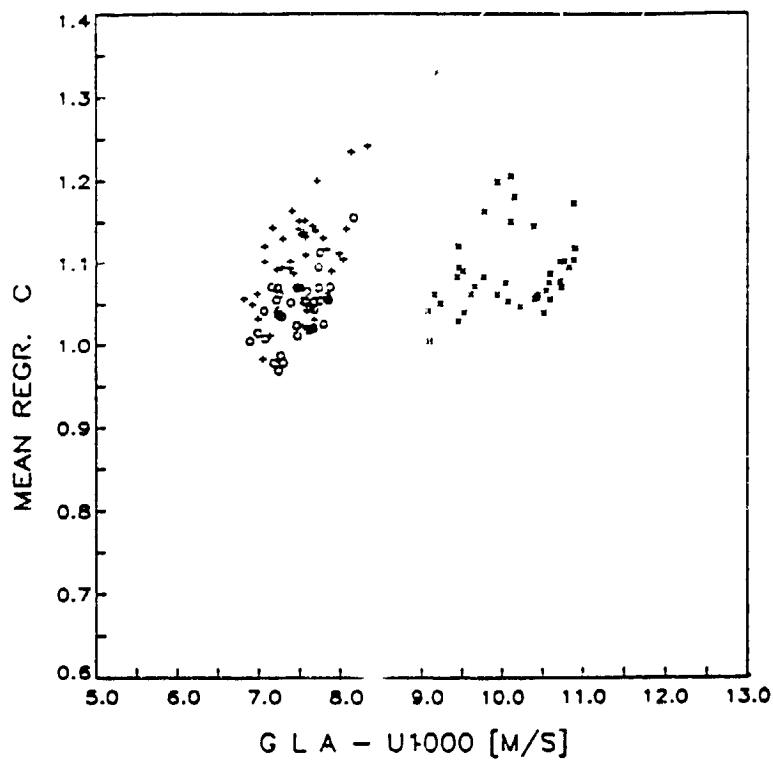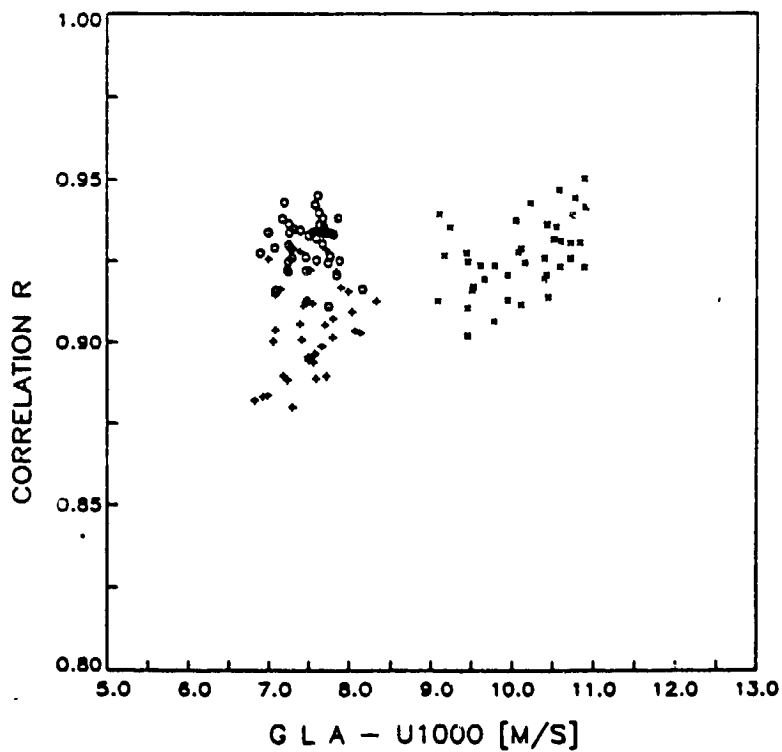
Fig. 3.1    Dependence of regression coefficient $\bar{c}$ (panel (a)) and correlation coefficient $r$ (panel (b)) on GLA wind speed for GLA-JPL intercomparison

<u>Fig. 3 2</u>        Dependence of regression coefficient $\tilde{c}$ (panel (a)) and correlation coefficient $r$ (panel (b)) on GLA wind speed for GLA-ECMWF intercomparison
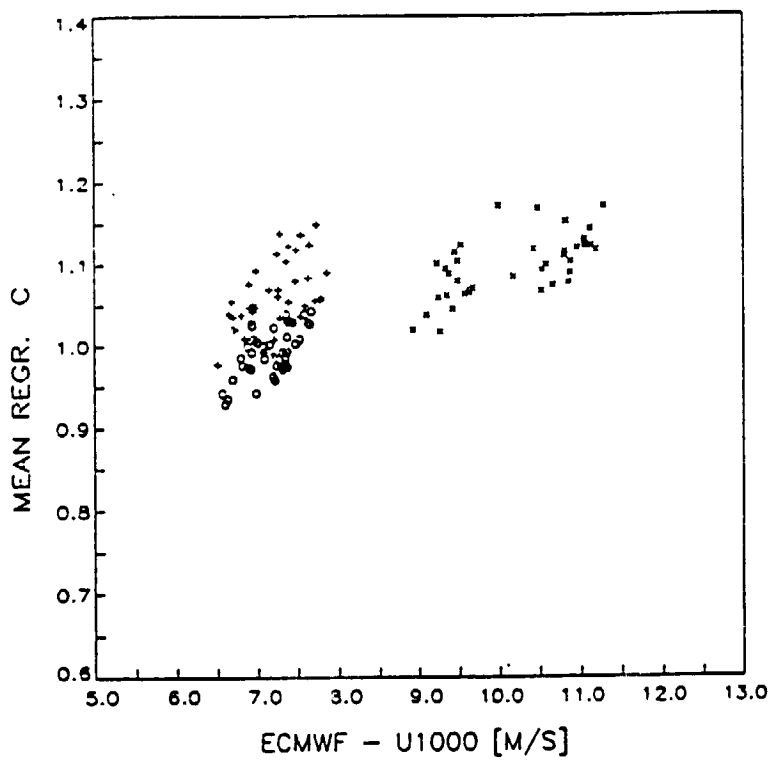
(a)



(b)

Fig. 3.3    Dependence of regression coefficient $\bar{c}$ (panel (a)) and correlation coefficient $r$ (panel (b)) on GLA wind speed for ECMWF-JPL intercomparison
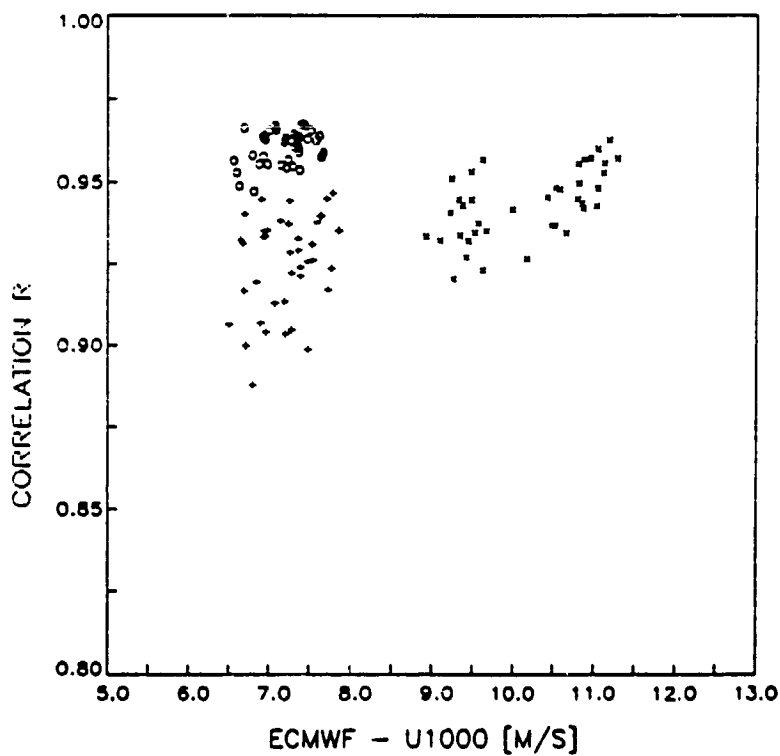
(a)
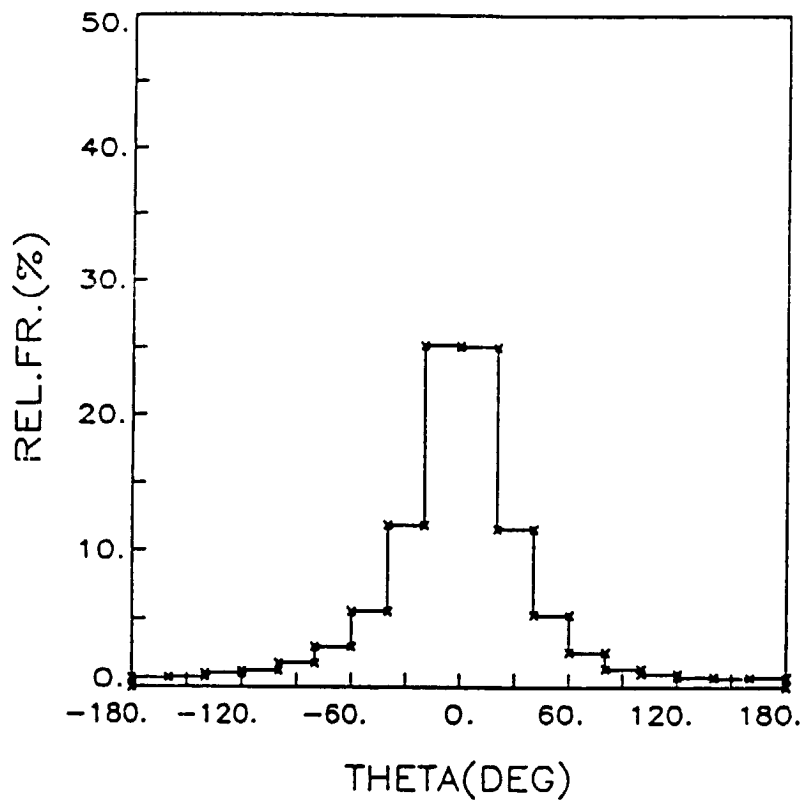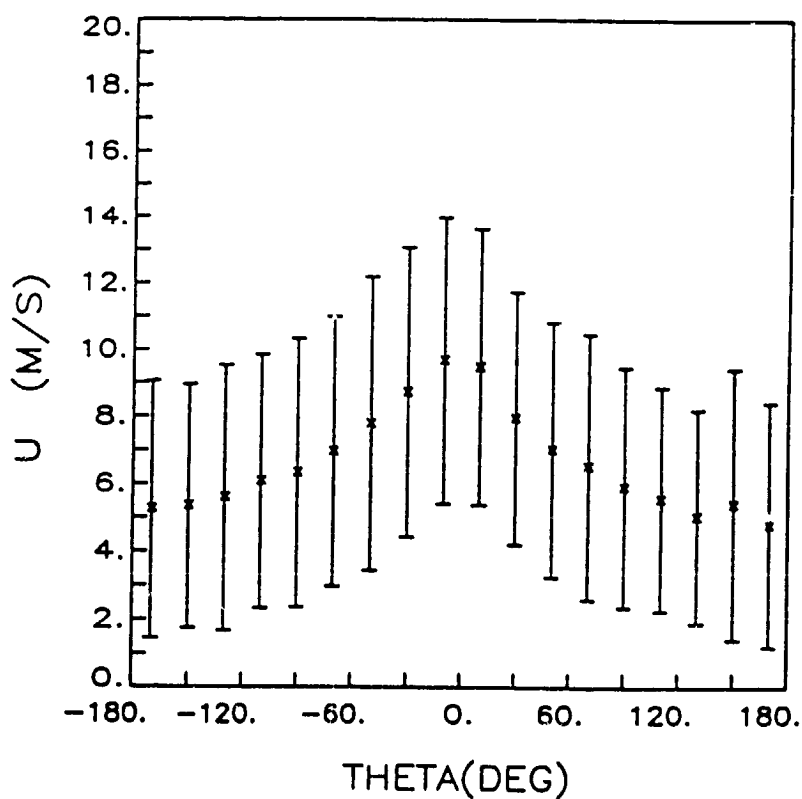


(b)

Fig. 3.4    Probability distribution of deviation in direction $\Delta\theta$ between wind vectors
(panel (a)) and mean wind speed and rms wind spread (panel (b)) as function
of $\Delta\theta$ for GLA-ECMWF intercomparison (70° S - 70° N)

The cause of the underestimate of the southern hemisphere wave hindcast is revealed in Figs 3 6a, b  These show the dependence of the regression coefficient $\bar{c}$ (i.e. the drag coefficient) and the correlation coefficient on the wind speed for the northern, southern and tropical regions. We expect an increase of $\bar{c}$ with wind speed in accordance with Charnock (1955) or other similar drag law relations (e g  Wu, 1982) Instead, $\bar{c}$ decreases with increasing wind speed  The northern hemisphere values of $\bar{c}$ of the order of 1.2 - 1.7·$10^{-3}$ are reasonably consistent with empirical drag laws for the moderate wind speeds characteristic of the northern hemisphere summer  The values for comparable wind speeds in the tropics are generally too low  However, the biggest bias is found in the southern hemisphere. For mean southern hemisphere wind speeds of the order of 11 - 12 m/s, Wu's formula gives $c_D$ = (1 52 - 1 58)·$10^{-3}$ which is 20 % to 60 % larger than the $\bar{c}$ values in the range 1.0 - 1 2·$10^{-3}$  For a fully developed spectrum, the significant wave height in the WAM model is proportional to the surface stress. Thus, it appears that the bias found in the model wave height hindcast relative to the altimeter wave heights in the southern hemisphere, which was of about the same magnitude, can be explained by the underestimate of the GLA surface stress fields in this region.

We can offer no simple explanation here for the cause of this underestimation However, it appears probable, in accordance with a suggestion of the GLA group, that it is related to the 6 hourly averaging involved in computing the stress field  Through the nonlinearity in the definition of $\bar{c}$, equ. (2 6), this leads to an underestimation of the drag coefficient, and a similar nonlinearity of the wave model response leads to a comparable underestimation of the wave height  The main conclusion we wish to draw from this analysis is that the operation of a wave model in conjunction with general data validation cross checking procedures, applied to both model products and observed data, can rapidly identify and locate problems in different data sets  The operational application of such procedures would clearly be very valuable for continually monitoring the performance of the ERS-1 wind and wave sensor system and algorithms

Other problems related to the original scatterometer winds (which were not considered in the present project) have been identified in the previous ESA study contract, Part I (Anderson et al , 1987) and Part II (Janssen et al , 1988)  All three investigations demonstrate that the simultaneous application of sophisticated models a general data assimilation system and a wide spectrum of data validation techniques on an operational basis is an essential pre-requisite for the implementation of a reliable end-to-end system for ERS-1 wind and wave data processing
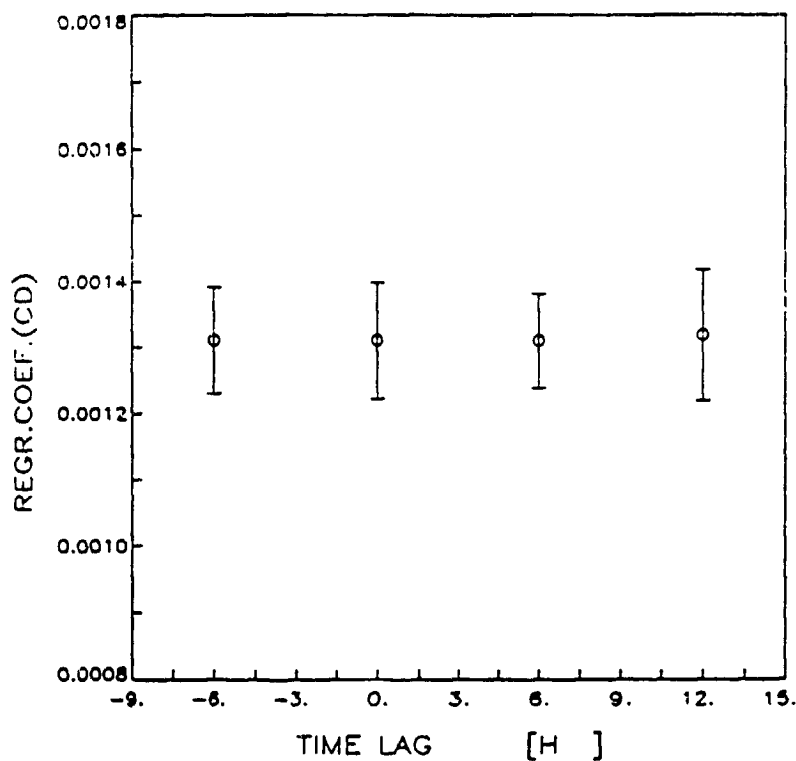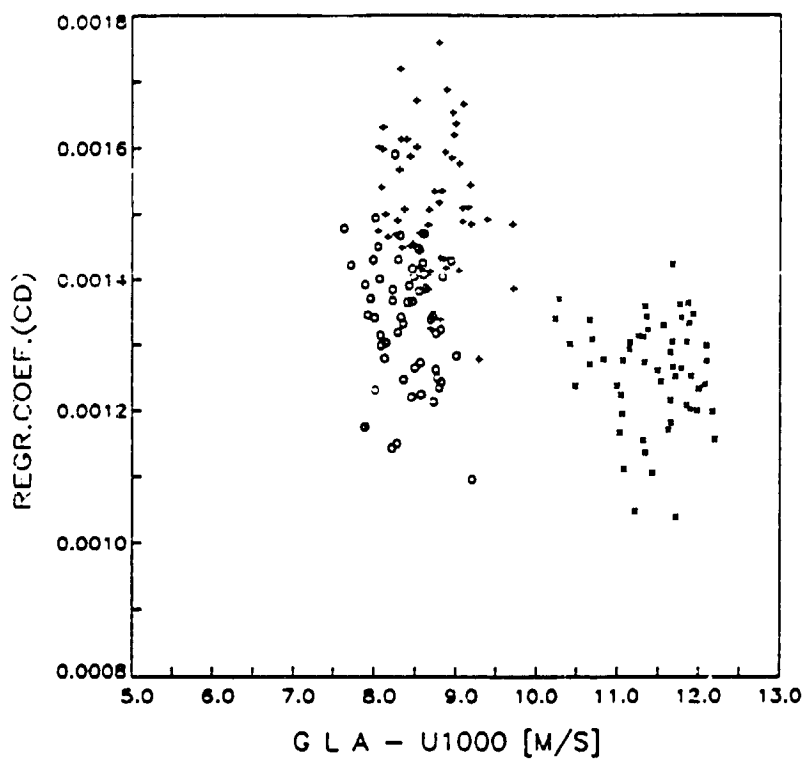
(a)
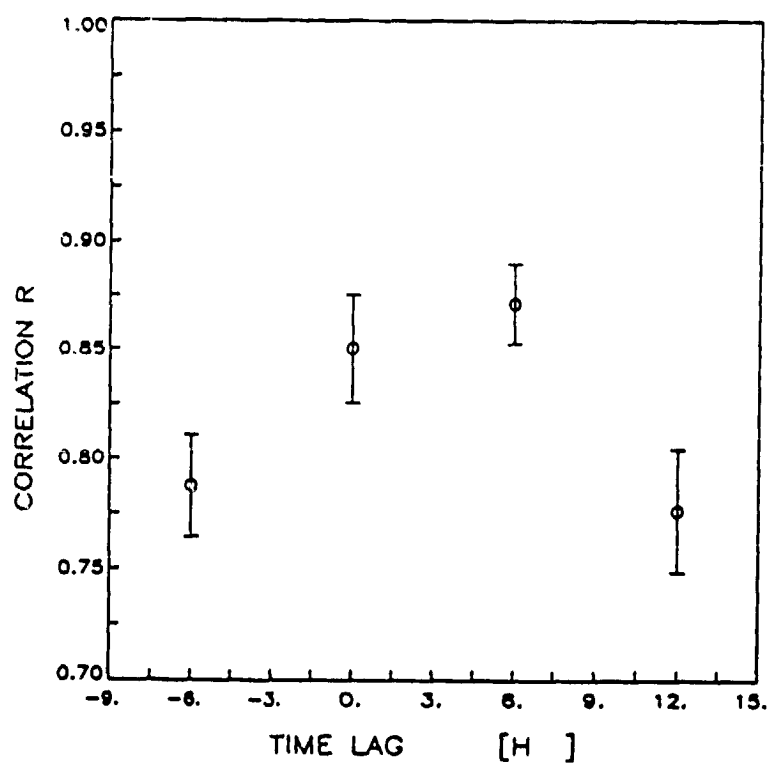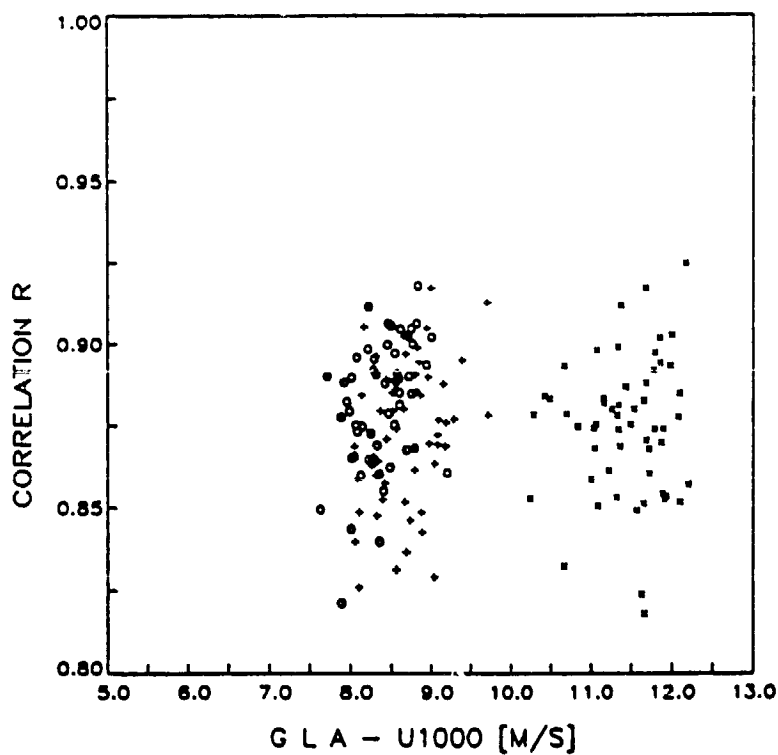


(b)

Fig. 3 5          Dependence of global regression coefficient r̄ and correlation coefficient r
                  for GLA t p₀ vs. t² on lag Δt

<u>Fig 3 6</u>        Regression (estimated drag) coefficient $\bar{c}$ (panel (a)) and correlation
coefficient $r$ (panel (b)) for regression between GLA fields $u$ p(0) and $u$ (1.6h)

## 3.2 Intercomparison of GLA surface wind field with SEASAT altimeter wind speeds

For completeness we show in this section an intercomparison of the GLA surface winds and the SEASAT altimeter wind speeds, which were obtained simultaneously with the altimeter wave height data shown in Section 2 1 The format of the analysis is identical to the intercomparison of the altimeter and wave model hindcast wave heights presented in Sections 2 1 and 2 2

None of the analysed wind fields considered in this study actually made use of the altimeter wind speeds It is generally accepted that the altimeter wind speeds, which are inferred from the altimeter measurement of the rms slope of the sea surface, are 'ess reliable than the scatterometer wind speeds derived from the short Bragg scattering surface wave ripples. This is confirmed in our analysis.

Fig. 3 7 shows the global distributions of time averaged altimeter wind speeds for the three approximately monthly averaging periods listed in Table 1. This may be compared with the corresponding Fig 3 8 for the GLA wind fields The altimeter winds are clearly significantly lower than the GLA winds, particularly in the high wind regions in the southern hemisphere. Since it was shown that the GLA wind fields, in contrast to the GLA stress fields, are consistent with other data in both hemispheres, the discrepancies must be attributed to the altimeter winds rather than the GLA wind field

An underestimation of the wind speed in the SEASAT altimeter algorithm at high wind speeds is found also in the statistical intercomparison of the GLA and altimeter wind speeds shown in Fig. 3.9 The high wind speed bias is of the order of 25 % A recalibration of the altimeter wind speed algorithm (which should be directly applicable also to the ERS-1 altimeter) appears called for Since the altimeter measures the rms sea surface slope, which is known to be a function not only of the local wind speed, but also of the sea state, an improved algorithm should preferably combine wind and wave information.

Fig 3 7 a    Averaged global fields for SEASAT altimeter wind speeds for July 1978 (exact averaging per ods are given in Table 1)

Fig 3.7 b    Averaged global fields for SEASAT altimeter wind speeds for August 1978
(exact averaging periods are given in Table 1)

Fig 3 7c    Averaged global fields for SEASAT altimeter wind speeds for September 1978
(exact averaging periods are given in Table 1)

61

Fig 3 8 a    Averaged global fields for GLA 1000 mb wind speeds for July 1978 (exact averaging periods are given in Table 1)
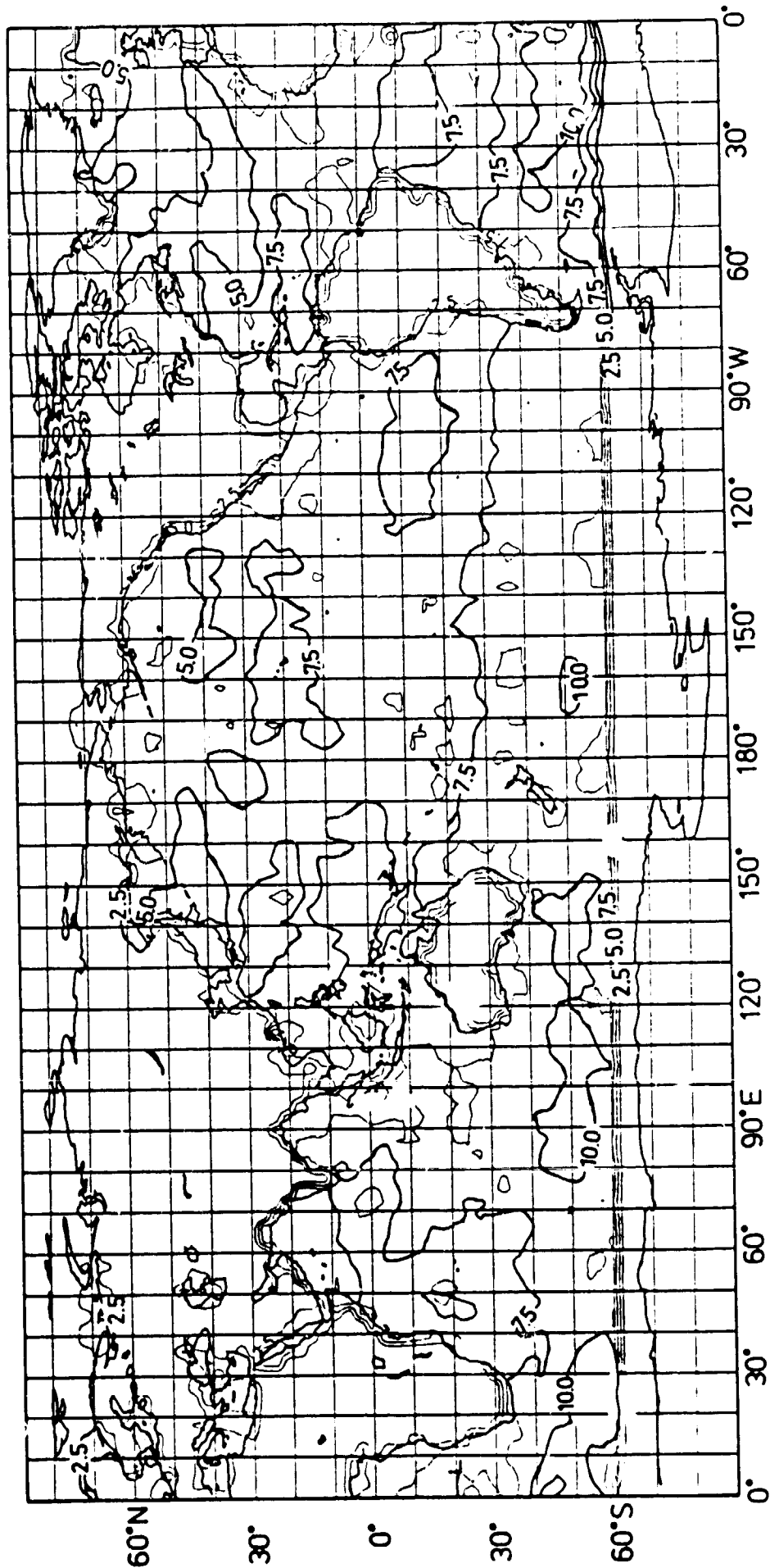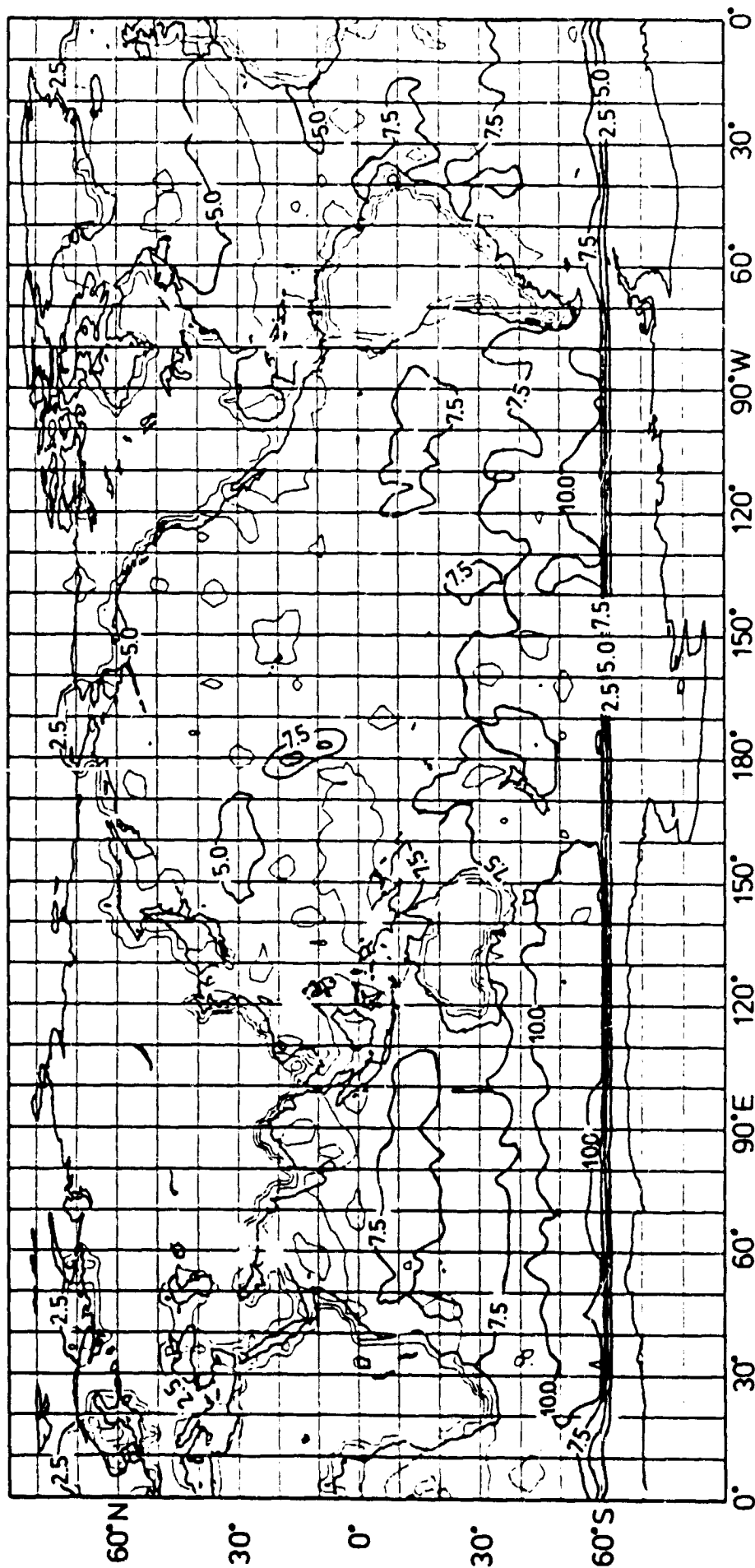
Fig 3.8 b    Averaged global fields for GLA 1000 mb wind speeds for August 1978 (exact averaging periods are given in Table 1)
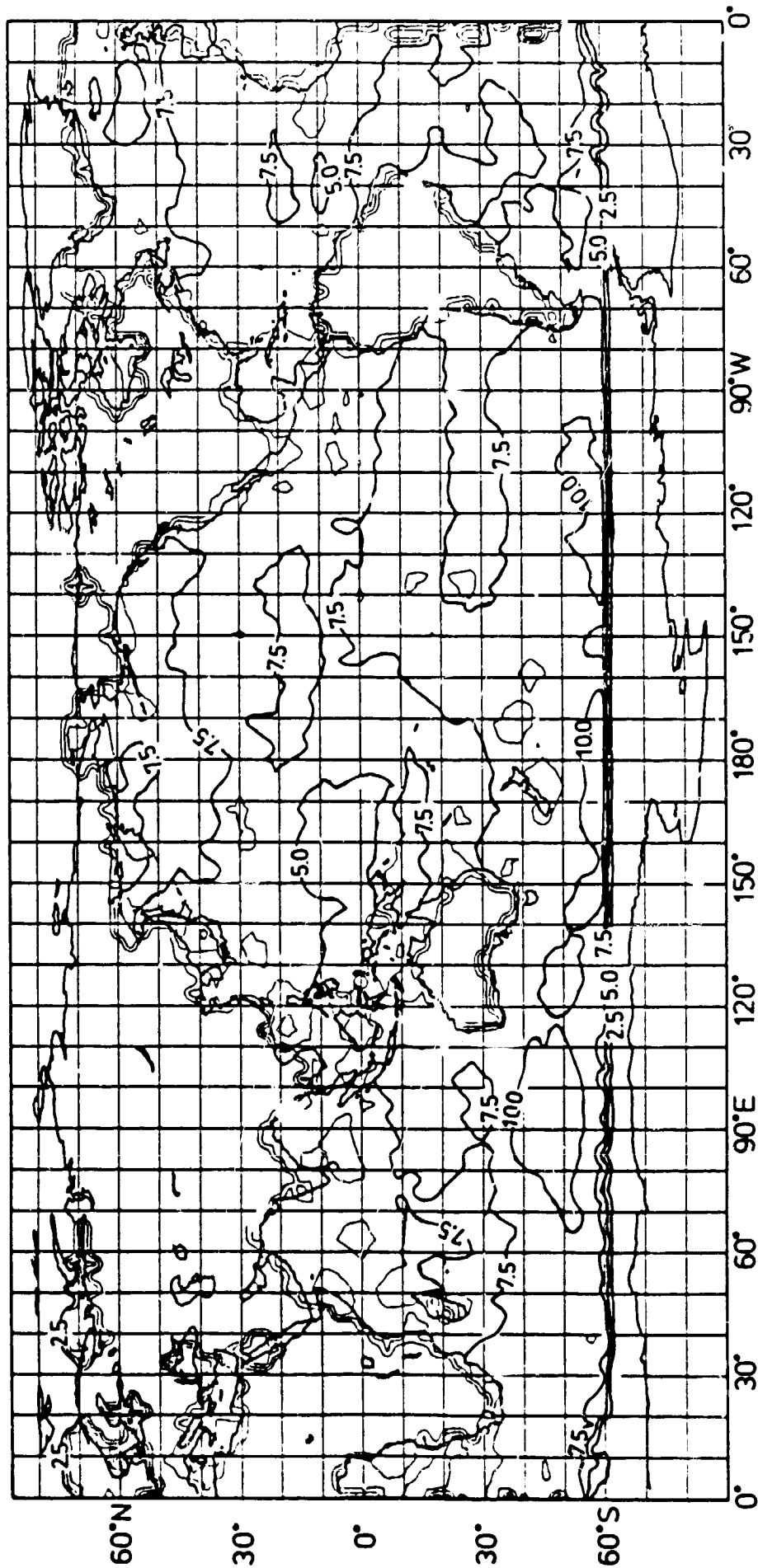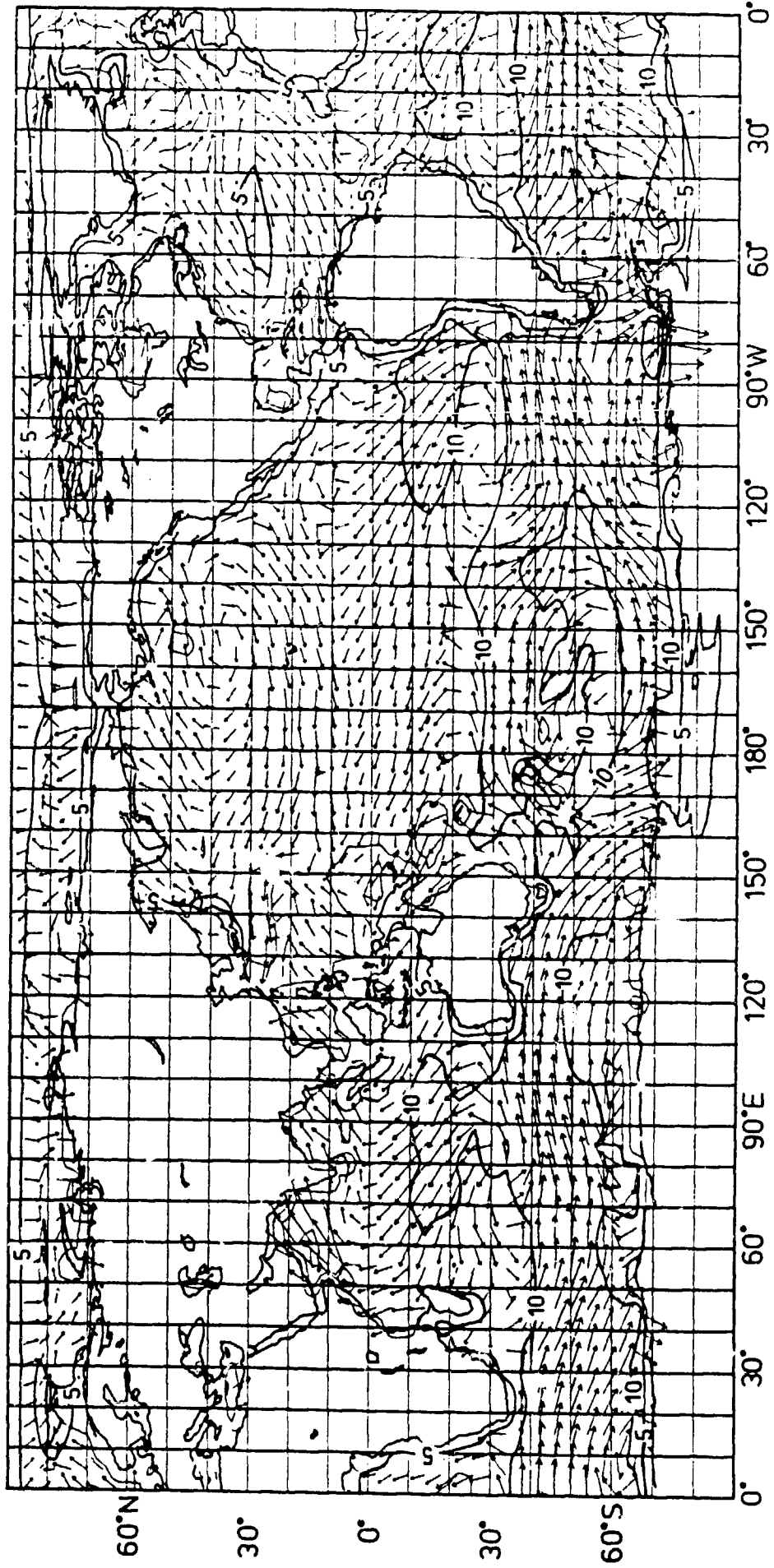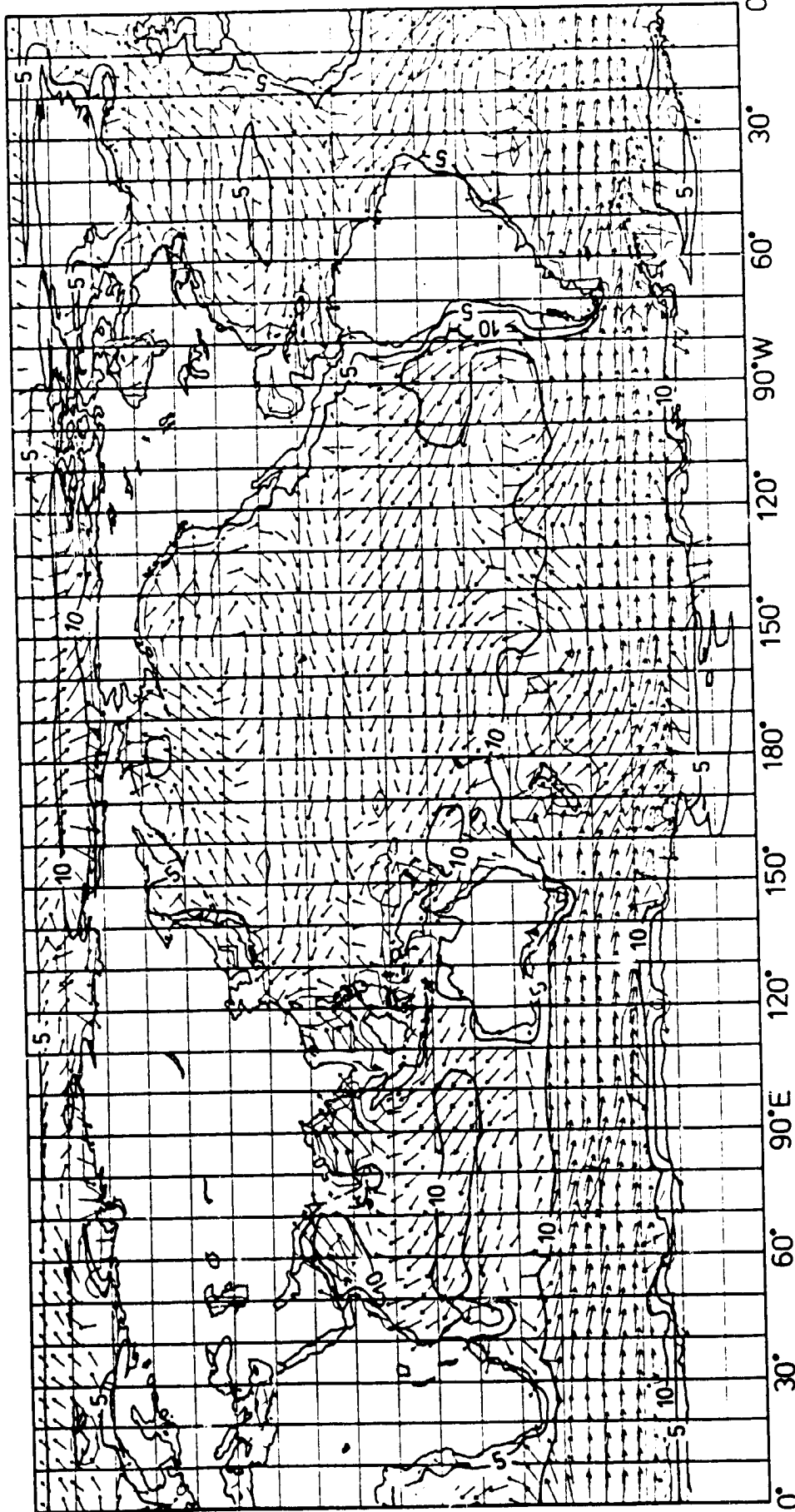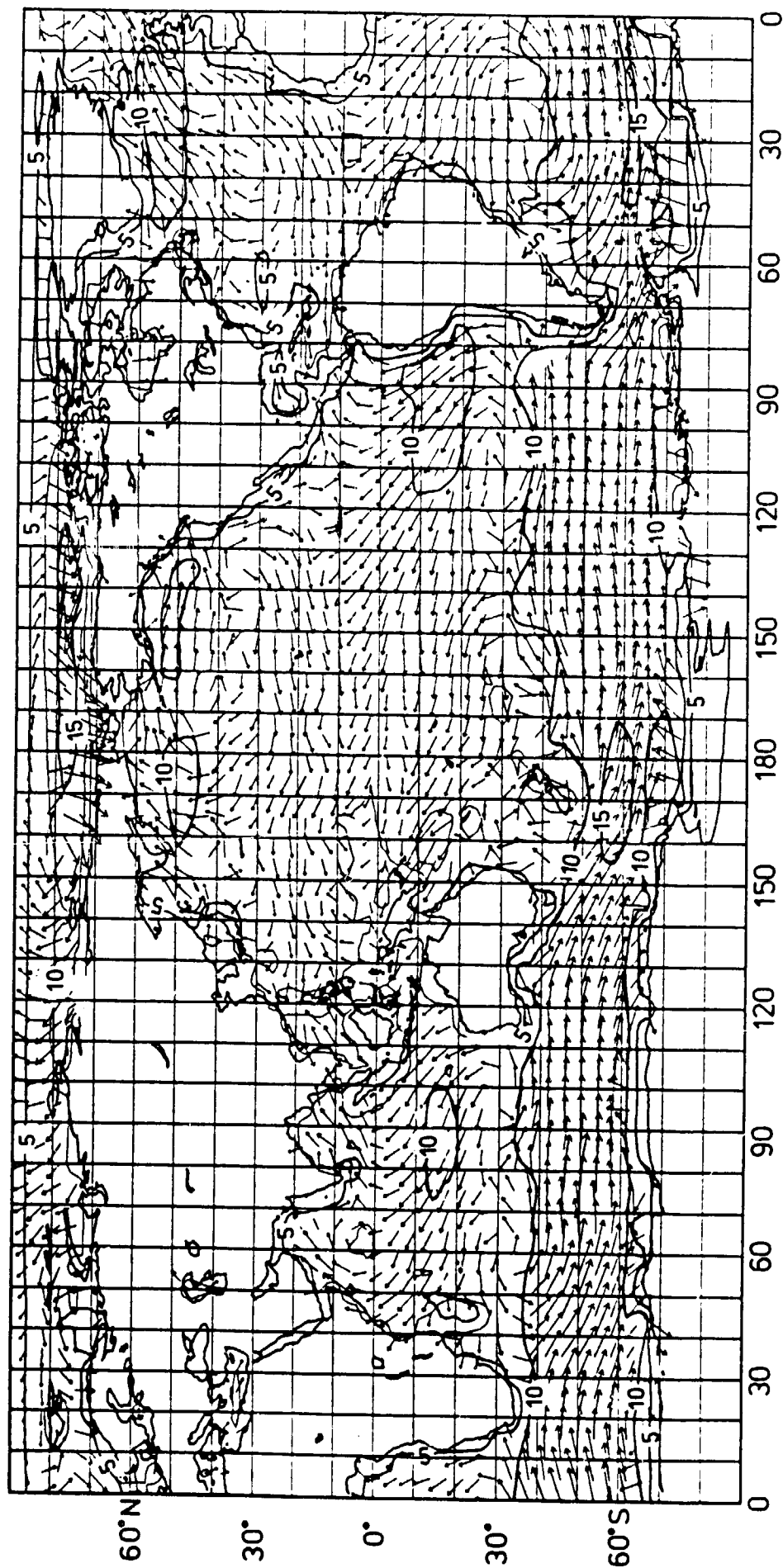
63

Fig 3.8 c    Averaged global fields for GLA 1000 mb wind speeds for September 1978
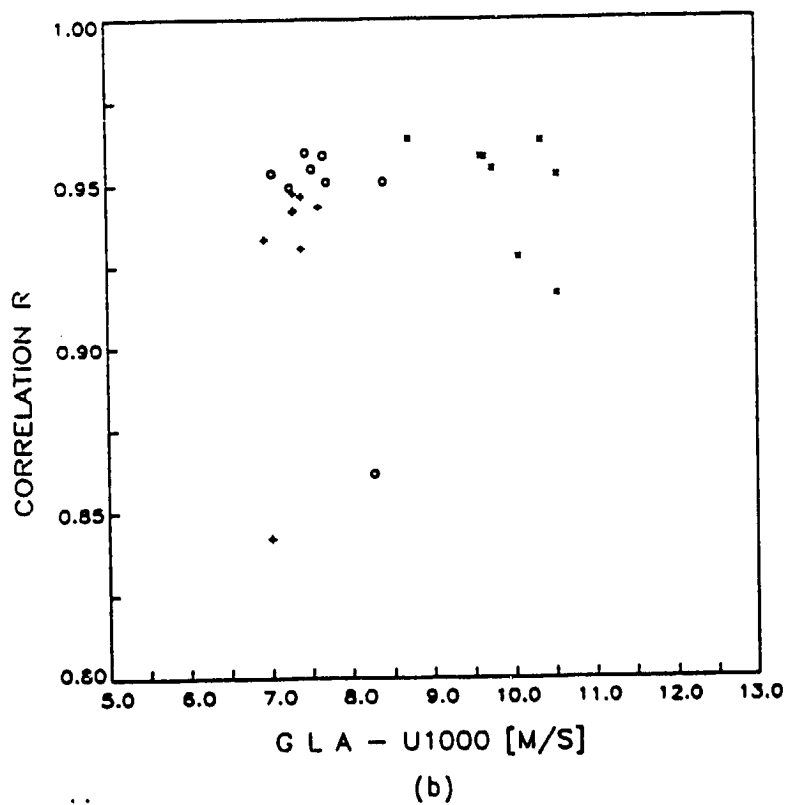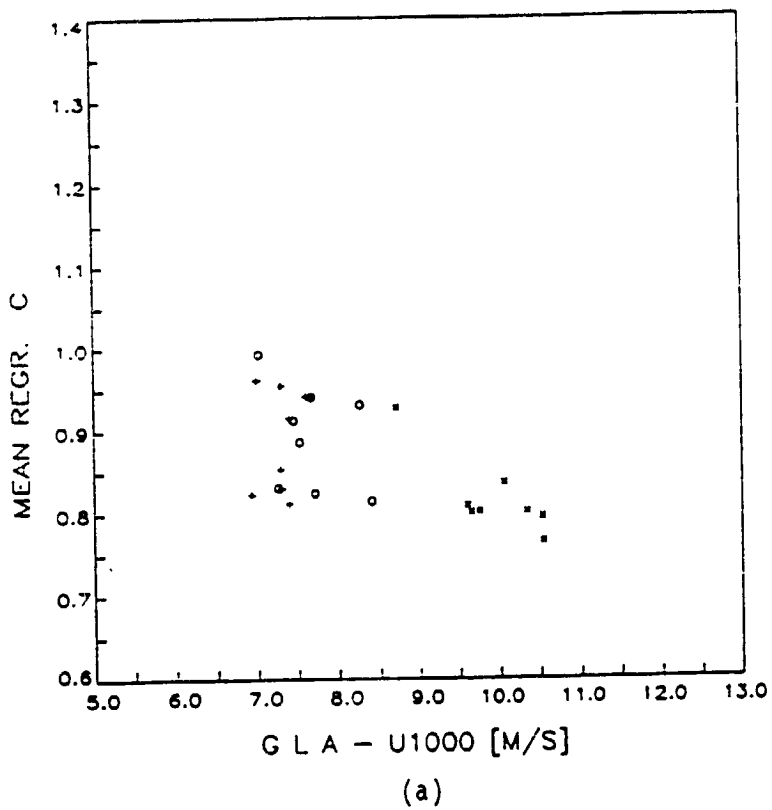(exact averaging periods are given in Table 1)

## 3.3 Intercomparison of wave model hindcasts for GLA, ECMWF and JPL surface forcing

It is of interest to investigate how the comparison between the surface wind and surface stress fields for the three wind field analyses discussed above is translated into the corresponding wave model hindcasts. As has already been pointed out, wave model simulations generally provide a sensitive test of the input wind fields.

Rather than repeat the statistical analysis presented in Section 3.1 for the wind speed and directions now in terms of the corresponding wave variables, the significant wave height and mean propagation direction, we show in Figs. 3.10 - 3.12 a comparison of the three global hindcast fields for the significant wave height, averaged over the common period September 6 - 17, 1978, of the three hindcasts.

The ECMWF and JPL wind fields were transformed into stress fields required as input for the wave model using Wu's formula (which was also used in the calibration of the wave model, cf. Komen, 1985, WAM-DIG, 1988).

$$\tau = c_D \rho_a U^2$$

where

$$c_D = \begin{cases} 1.2875 \cdot 10^{-3}, & U < 7.5\,m/s \\ (0.8 + 0.065 \cdot U) \cdot 10^{-3}, & U \geq 7.5\,m/s \end{cases}$$

No distinction was made between the 1000 mb ECMWF winds and the 19.5 m height JPL winds.

Figs. 3.10 - 3.12 support the general conclusions of Section 3.1: there is reasonably good agreement between the three forcing fields in the northern hemisphere, while the GLA forcing is clearly significantly weaker than the other two forcing fields in the high wind region of the southern hemisphere. A comparison with the altimeter wave heights shown in Section 2.1 for the entire 96-day period suggests that the ECMWF and JPL forcing fields are probably of about the right magnitude in the mid- and high-latitude southern hemisphere, while the GLA stress field is too weak in this region.

Apart from these general relations, the figures reveal a number of regional deviations, which will not be pursued here, but would clearly be of interest in applying a wave model for wind field validation in an operational setting

Filg 3.10   Significant wave height for wave hindcast for GLA surface stress field for the
period September 7 - 17, 1978

68

Fig 3 11    Significant wave height for wave hindcast for ECMWF surface wind field for
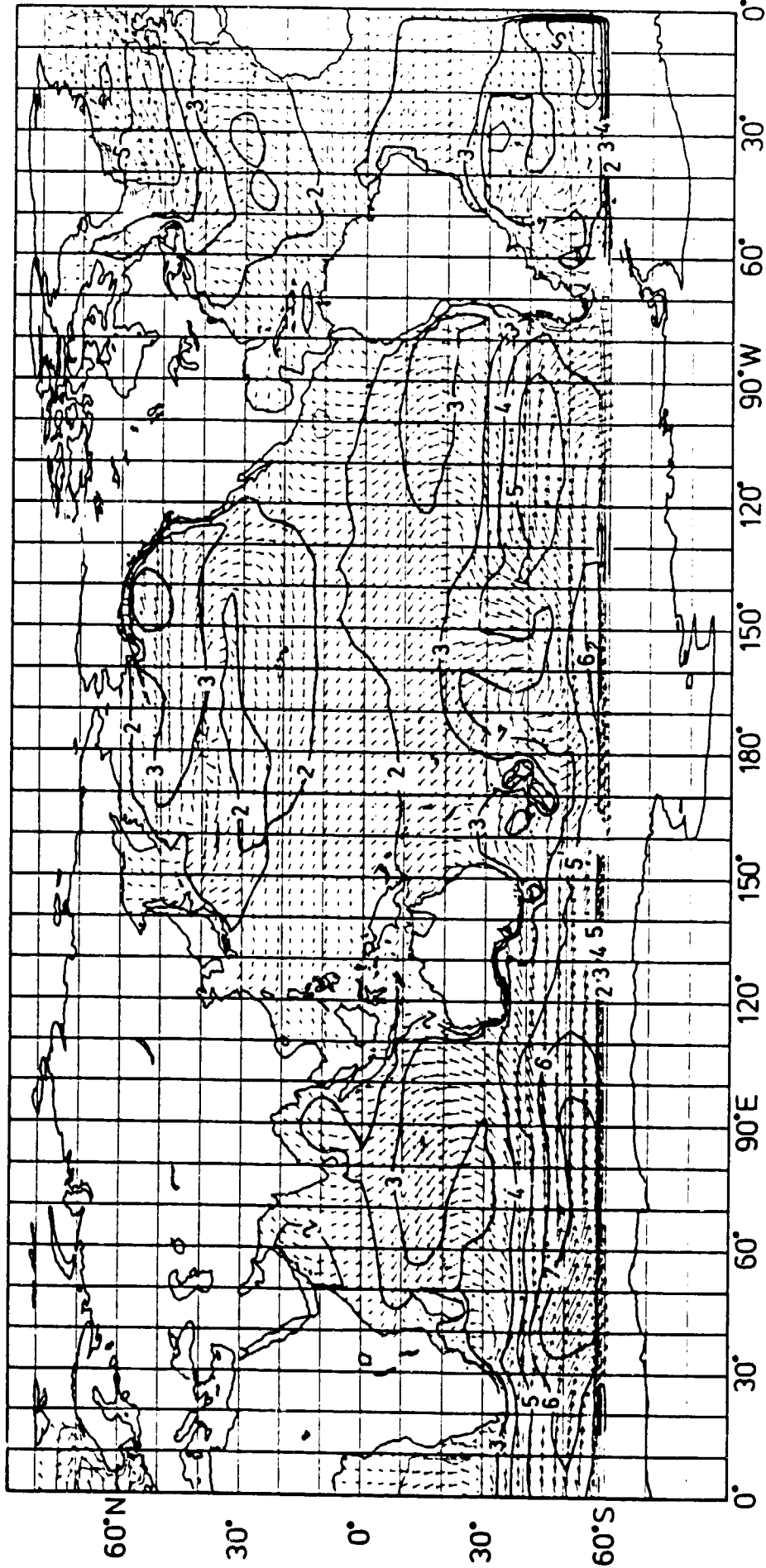the period September 7 - 17, 1978

69

Fig 3.12    Significant wave height for wave hindcast for JPL surface wind field for the
            period September 7 - 17, 1978

70

## 4 Computations of the linear and nonlinear mapping relation between ocean wave spectra and SAR image spectra

### 4.1 Introduction

ERS-1 will be the first satellite to provide global SAR wave data through the AMI wave mode instrument. The potential value of global two-dimensional SAR wave image spectra for wave forecasting can hardly be over-emphasized. However, the effective use of SAR wave data requires the development of efficient methods for recovering the wave spectrum from the SAR image spectrum. This is a non-trivial task. The first step, considered in this section, is to derive an efficient method for computing the mapping from a surface wave spectrum into a SAR image spectrum. We discuss the second step, the solution of the inverse mapping problem, later in Section 6.

The theory for the imaging of a moving ocean surface by a Synthetic Aperture Radar is reasonably well understood. Although open questions still remain regarding finer details of the backscattering mechanism, it is generally agreed that in the range of incidence angles between 20° and 60° typical of most SAR operation conditions the backscattered return may be represented as a superposition of the statistically independent returns from a continuous ensemble of small scale facets. The backscattered return from each facet is governed by the Bragg scattering from short ripple waves. The backscattering from the short waves in turn is modulated by the longer waves, thereby enabling a SAR to image normal ocean waves.

The long wave modulation consists of three processes

(i)    the hydrodynamic interaction between short and long waves,

(ii)    the change in the local incidence angle (tilt) of the facet and

(iii)    the advection of the facet by the long wave orbital velocity, which produces doppler shifts in the return signal.

It can be assumed for all of these processes that to first order the backscattering ripple waves and the modulating ocean waves are widely separated in scale. The scale separation assumption is well satisfied for microwaves ($\lambda \sim 1 - 30$ cm) and ocean wave spectra ($\lambda \sim 10 - 1000$ m). The two-scale model was first developed by Wright (1968) and

Bass et al. (1968) and has been extensively tested and verified in field and wave tank experiments. On the basis of this model, a rather complete theory of SAR imaging of a random ocean wave field can be developed (cf. Alpers et al., 1979, Hasselmann et al., 1985)

An important feature of this theory is that SAR imaging can become strongly nonlinear. Although the hydrodynamic and tilt modulation can normally be regarded as linear processes, the motion effects become strongly nonlinear in typical windsea situations. The doppler shift arising from the radial component of the orbital velocity of a backscattering facet produces an azimuthal displacement of the apparent position of the backscattering facet in the image plane. For displacements small compared with the characteristic wavelength of the long waves, this 'velocity bunching' mechanism can be treated as a linear process. It can be characterized by a 'velocity bunching modulation transfer function' which, just as the hydrodynamic and tilt mtf's, contributes to the wave image contrast. However, if the displacements become comparable with or larger than a quarter wavelength, the velocity bunching mechanism becomes nonlinear, and for still larger displacements ultimately results in a complete smearing of the image.

The transformation of a surface wave spectrum into a SAR image spectrum has been computed numerically in the weakly and strongly nonlinear regimes by Monte Carlo techniques (Alpers and Bruning, 1986, Bruning, 1987, Bruning et al., 1988). From an extensive compilation of such simulations for different wave conditions and SAR parameters, Bruning et al. (1988) derived general relations for the distortion of the surface wave spectrum in the SAR image spectrum. To first order, the principal effects are that short waves travelling in the azimuthal direction are filtered out, the spectrum is skewed towards the range direction, and the mean wavelength is increased.

The Monte Carlo computations are based on individual realizations of a random surface wave field. For each realization, the individual moving backscattering surface elements in each scene are mapped into their corresponding positions in the SAR image plane, and the resulting image is Fourier transformed. The SAR image variance spectrum is then computed by averaging the spectra for an ensemble of such realizations. This 'brute force' method is rather expensive in computer time. Thus it cannot be applied operationally in a wave model to relate the model output spectrum to the large number of SAR image spectra which will be provided continuously by future oceanographic satellites such as ERS-1 or RADARSAT.

In this section an alternative computation is proposed  it is shown that the wave spectrum and SAR image spectrum can be related directly in both the linear and nonlinear mapping regimes, through a general nonlinear integral equation  The transformation can be readily evaluated numerically and can therefore be used in routine operational applications

At first sight it appears rather surprising - in view of the notorious closure problems of strongly nonlinear systems - that a closed expression can be derived relating the surface wave spectrum and the SAR image spectrum in the strongly nonlinear regime  However, closure is possible in the present case because the input and output fields do not interact dynamically, and to a good first approximation the input surface wave field itself can be regarded as linear and Gaussian

Similar techniques to those developed in Sections 4 3, 4 4 have been applied previously in the computation of the dissipation of finite-depth surface waves by bottom friction (Hasselmann and Collins, 1968) and in the determination of the structure of the dissipation source function due to white capping (Hasselmann, 1974)  The basic concept is to consider the isolated impact on the process of the infinitesimal contribution from a single Fourier component of the input field  This can be determined rigorously, because for a Gaussian wave field the infinitesimal contribution to the continuous spectrum are statistically independent  The resulting (nonlinear) integro-differential expression relating the infinitesimal change in the surface wave spectrum to the associated infinitesimal change in the image spectrum can then be integrated analytically to yield the general nonlinear integral transformation from the ocean wave spectrum to the SAR image spectrum

In the following Section 4 2 we summarize first the relations for RAR (real aperture radar) and SAR imaging, as derived from the standard two-scale scattering theory  and introduce notations  The general nonlinear transformation relating the SAR image spectrum to the ocean wave spectrum is then derived in Section 4 3  A more detailed discussion of the various terms occurring in the transformation is given in Section 4 4

### 4 2   Mapping of the ocean surface into the SAR image plane

The SAR surface wave imaging process may be divided into two processes  the RAR (real aperture radar) imaging processes, consisting of hydrodynamic and tilt modulations, and the motion effects, which are specific to the SAR and have no influence on RAR imaging.

We consider first the RAR imaging process

Decomposing the surface elevation $\zeta(x, t)$ and the local back-scattering cross section $\sigma(x, t)$ sensed by a RAR into discrete Fourier series,

$$\zeta(x, t) = \sum_k \zeta_k \exp[i(k \cdot r - \omega t)] + \text{compl. conj.} \qquad (4.1)$$

$$\sigma(x, t) = \sigma \left\{ 1 + \left[ \sum_k m_k \exp[i(k \cdot r - \omega t)] + c.c. \right] \right\} \qquad (4.2)$$

where $\sigma$ is the spatially averaged mean (specific) cross section and $m_k$ the cross-section modulation factor. the standard two-scale scattering theory for hydrodynamic and tilt modulation yields a linear relation

$$m_k = T_k^R \zeta_k \qquad (4.3)$$

between the Fourier components of $\zeta$ and $\sigma$, with a net RAR complex modulation transfer function (MTF) $T_k^R = T_k^{hyd} + T_k^{tilt}$ which consists of the sum of the hydrodynamic and tilt modulation transfer functions. For our purposes we regard $T_k$ as given. (It is notationally more convenient to work with discrete Fourier sums than with continuous integrals as we shall be considering later differentials with respect to individual Fourier components. The discrete representation avoids the rather cumbersome functional derivative notation.)

In equ. (4.1) the frequency is given by the free gravity wave dispersion relation $\omega = \sqrt{gk}$, where $g$ is the acceleration of gravity. it should be noted that equations (4.1), (4.2) represent three-dimensional wavenumber-frequency spectra which have been reduced to two-dimensional spectra because the frequencies are constrained to lie on the dispersion surface. in contrast to the two-dimensional wavenumber spectrum of a frozen surface considered below (equ. (4.4)). Fourier components of opposite sign in $k$ represent waves travelling in opposite directions and are not related

Radars, on the other hand, produce quasi-instantaneous images of the surface, so that the relevant Fourier decomposition of the image $I(r)$ at a fixed time, $t = 0$, say takes the form

$$I(t) = \left| 1 + \sum_{k} I_k \exp(ik \cdot r) \right|$$  (4.4)

where

$$I_k = (I_{-k})^*$$  (4.5)

and the image intensity is normalized with respect to the mean image intensity (Note that the explicit complex conjugate term of eqns (4.1), (4.2) is missing here, as it is already included in the sum over positive and negative **k**)

For a RAR, the image intensity is simply proportional to the cross section, so that

$$I^R(r) = \sigma(r,0) - \sigma$$  (4.6)

and equations (4.1) - (4.5) yield

$$I_k^R = T_k^R \zeta_k + \left( T_{-k}^R \zeta_{-k} \right)^*$$  (4.7)

From equ (4.7) we find then that the relation between the ocean wave and image variance spectra $F_k$, $P_k$, respectively, defined by

$$\langle \zeta^2 \rangle = \sum_{k} F_k = 2 \sum_{k} \langle \zeta_k \zeta_k^* \rangle$$  (4.8)

$$\langle I^2 \rangle = \sum_{k} P_k = \sum_{k} \langle I_k^* I_k \rangle$$  (4.9)

where the cornered parentheses $< \quad >$ denote ensemble averages, is given by

$$P_k^R = \left| T_k^R \right|^2 \frac{F_k}{2} + \left| T_{-k}^R \right|^2 \frac{F_{-k}}{2}$$  (4.10)

The RAR image $I^R(r)$ corresponds to the image which a SAR would produce if the sea surface were frozen. Consider now the distortion of this image induced by the motion effects. These consist of two terms: an azimuthal displacement $\xi$ of the

position of a backscattering element in the image plane, and an azimuthal smearing or broadening $\delta x$ of the (theoretically infinitesimal) backscattering element in the image

The azimuthal displacement is proportional to the range component $c$ of the average advection (i.e. orbital) velocity of the backscattering element (cf. Alpers and Rufenach, 1979)

$$\xi = Bc \tag{4.11}$$

where

$$B = \rho / U \tag{4.12}$$

and $\rho$ is the slant range, $U$ the velocity of the SAR. The orbital velocity $c$ is defined here as the time average velocity over the period during which the scattering element is viewed by the SAR. Normally, this is small compared with the wave period, so that, to first order, we may set $c$ equal to the instantaneous orbital velocity component in the range direction at the median time assigned to the SAR image

According to standard surface wave theory (cf. Phillips, 1977),

$$c = \sum_{\mathbf{k}} T_{\mathbf{k}}^v \zeta_{\mathbf{k}} \exp(i(\mathbf{k}r - \omega t)) + c.c. \tag{4.13}$$

where the range velocity transfer function is given by

$$T_{\mathbf{k}}^v = \omega - (\cos\theta - \sin\theta\, k_y / |k|), \tag{4.14}$$

and $\theta$, $k_y$ denote the radar incidence angle and the wavenumber component in the horizontal radar look direction, respectively

The smearing term $\delta x$ is normally represented as the sum of an acceleration term $\delta x_a$ and a velocity spread term $\delta x_v$ (cf. Hasselmann et al., 1985)

The acceleration term $\delta x_a$ is a second order term arising from the variation of the instantaneous orbital velocity component $c$ during the SAR viewing interval. This yields slightly different effective displacements $\xi$ for the beginning and the end of the viewing period. The term is generally smaller than the velocity spread term (cf. Alpers

and Rufenach, 1979, Alpers et al., 1981, Hasselmann et al., 1985) and, to simplify the analysis, will not be considered in the following.

The velocity spread term $\delta x_v$ is identical in physical origin to the azimuthal displacement term. It is distinguished in SAR theory from the displacement term only for formal reasons. In a combined microwave backscattering and SAR imaging theory, it is convenient to distinguish between two separate two-scale models, the hydrodynamic/backscattering and the SAR two-scale model (cf. Hasselmann et al., 1986). In the hydrodynamic/backscattering model, which we have been considering so far, the separation scale $L_{hyd}$ corresponds to the dimensions of the backscattering facets. This must be large compared with the wavelength of the Bragg scattering waves but small compared with the wavelength of the modulating long wave field. Typically, $L_{hyd}$ is of order 1 m. In the SAR two-scale model, on the other hand, the separation scale $L_{SAR}$ is defined as the SAR resolution scale, which is typically of order 20 m. The SAR is unable to distinguish between individual backscattering facets within a SAR resolution cell, and therefore maps the entire ensemble of backscattering facets within a resolution cell into a single image pixel. This is azimuthally displaced by an amount $\Delta x = \beta \bar{v}$ determined by the mean orbital velocity $\bar{v}$ of the facet ensemble. The deviations $\delta x = \xi - \bar{\xi}$ of the individual facet displacements from the mean value $\bar{\xi}$ for the resolution cell then results in a smearing of the image of the resolution cell. The rms value of this smearing is given by

$$\delta x_v = \beta \left( \overline{(v - \bar{v})^2} \right)^{\frac{1}{2}}$$

(4.15)

The term is essentially determined by the contribution to the rms orbital velocity from the region of the wave spectrum lying between the two separation scales $L_{hyd}$ and $L_{SAR}$.

In the present context it is important to note that the introduction of a velocity spread term is a formality, which in some cases has conceptual advantages, but is not a necessity. In our case it is more convenient to work entirely in the framework of the basic hydrodynamic/backscattering two-scale model, without invoking the velocity spread concept. In this picture we consider the SAR image as composed of a superposition of the independent images of individual basic backscattering facets, rather than of individual resolution cells.

Each backscattering facet experiences an azimuthal displacement in the image in accordance with (4.11) and some defocussing through the facet acceleration (which

−−

we ignore). In addition, the individual facet images will then be smeared by the finite resolution of the SAR. Thus we consider a pure 'velocity bunching' theory with 'explicit velocity spreading' To simplify the analysis, however, we ignore also the smearing by the finite SAR resolution and assume the SAR has infinite resolution. The effect of the finite SAR resolution can be easily taken into consideration, if necessary, as an additional filter at the end of the analysis Qualitatively, the acceleration smearing term can be similarly handled, although its rigorous inclusion in the theory is somewhat more complicated The effects we have retained do, in fact, represent the critical processes limiting the ocean wave imaging performance of a SAR in the nonlinear imaging regime.

Applying equ. (4.11) to a continuum of facets, we obtain then as the relation between the SAR image and the RAR image in the present 'velocity bunching' model

$$I^S(\mathbf{r}) = \int I^R(\mathbf{r'}) \delta(\mathbf{r} - \mathbf{r'} - \boldsymbol{\xi}(\mathbf{r'})) \, d\mathbf{r'} \tag{4.16}$$

where $\boldsymbol{\xi} = \mathbf{a}\xi$ and $\mathbf{a}$ denotes the unit vector in the azimuthal direction

Integrating over the $\delta$-function, equ. (4.16) yields

$$I^S(\mathbf{r}) = \left\{ I^R(\mathbf{r'}) \left| \frac{d\mathbf{r'}}{d\mathbf{r}} \right| \right\}_{\mathbf{r'} = \mathbf{r} - \boldsymbol{\xi}(\mathbf{r'})} \tag{4.17}$$

where the Jakobian

$$\left| \frac{d\mathbf{r'}}{d\mathbf{r}} \right| = \left| 1 + \frac{d\xi(\mathbf{r'})}{d\mathbf{r'}} \right|^{-1} \tag{4.18}$$

The 'velocity bunching factor' $|d\mathbf{r'}/d\mathbf{r}|^{-1}$ represents the variation in the effective density of backscattering elements in the image plane resulting from the compression or dilatation of the originally homogeneous distribution of facets through the spatial variations of the facet azimuthal displacement. This enables the SAR to image ocean waves even in the hypothetical situation in which the RAR transfer function vanishes, i.e. $I^R(\mathbf{r}) = const.$

For the case

$$\frac{\partial \xi(\mathbf{r}')}{\partial r'} \ll 1 \qquad (4.19)$$

the velocity bunching factor can be expanded in a geometrical series and truncated after the linear term. If it is furthermore assumed that the modulation of is small, as required for a linear RAR imaging theory, the dominant term in (4.17) is the linearized velocity bunching factor, and one obtains for the SAR image amplitude spectrum, in accordance with (4.4), (4.13):

$$\hat{I}_k = I_k^R + \left( T_k^b \zeta_k - \left( T_{-k}^b \zeta_{-k} \right)^* \right) \qquad (4.20)$$

where the velocity bunching modulation transfer function

$$T_k^b = -\beta k_s T_k^v \qquad (4.21)$$

Thus in the linear approximation

$$\hat{I}_k = T_k^s \zeta_k - \left( T_{-k}^s \zeta_{-k} \right)^* \qquad (4.22)$$

and the image variance spectrum is given by

$$P_k = \left| T_k^s \right|^2 \frac{F_k}{2} + \left| T_{-k}^s \right|^2 \frac{F_{-k}}{2} \qquad (4.23)$$

where the SAR imaging transfer function

$$T_k^s = T_k^R + T_k^b \qquad (4.24)$$

The condition (4.19) is generally satisfied for swell spectra. However, in many situations, for example for short windseas, the inequality does not hold or is even reversed (cf. Hasselmann et al., 1985, Bruning et al. 1988). In this case, equations (4.17), (4.18) represent a strongly nonlinear transformation and we must seek alternative methods for deriving the relation between the surface wave and SAR image spectrum

## 4.3 The nonlinear mapping from the surface wave to the SAR image spectrum

The relation describing the nonlinear transformation from the surface wave spectra to the SAR image spectra is derived in two steps. First a differential relation describing the effect of an infinitesimal perturbation in the surface wave spectrum on the SAR image spectrum is developed. This expression is then integrated to yield the final nonlinear transformation relation.

The Fourier component $I_k^S$ of the SAR image is obtained by taking the Fourier transform of (4.17).

$$I_k^S = \frac{1}{A} \int dr\, I^R(r) \frac{dr'}{dr}\, \exp(-i\mathbf{k}\cdot\mathbf{r}) = \frac{1}{A} \int dr'\, I^R(r')\exp[-i\mathbf{k}(\mathbf{r}' - \xi(\mathbf{r}'))] \tag{4.25}$$

Here $A$ denotes the finite area of the sea surface corresponding to our discrete Fourier reresentation (in the final result, we shall, of course, let $A \to \infty$).

Substituting the Fourier representation (4.4), (4.7) for $I^R$ in (4.25), this becomes

$$I_k^S = \frac{1}{A} \int dr' \left\{ 1 - \sum_{k'} \left( T_{k'}^R \zeta_k - T_{-k'}^{R*} \zeta_{-k'}^* \right) \exp[i\mathbf{k'}\cdot\mathbf{r}'] \right\} \left\{ \exp[-i\mathbf{k}\mathbf{r}' - i\mathbf{k}\xi(\mathbf{r}')] \right\} \tag{4.26}$$

We obtain then for the variation $\delta I_k^S$ induced by perturbing the set of Fourier components of the input wave field by the infinitesimal increments $\delta\zeta_k$

$$\delta I_k^S = \sum_{k'} \left( M_{kk'} \delta\zeta_{k'} - M_{-k-k'}^* \delta\zeta_{-k'}^* \right) \tag{4.27}$$

where

$$M_{kk'} = \frac{1}{A} \int dr' \left| \exp[i(\mathbf{k'} - \mathbf{k})\mathbf{r}' - i\mathbf{k}\xi(\mathbf{r}')] \right|$$

$$\left[ T_k^S - ik \cdot \beta \left( T_{k'}^R \right) \right] \left\{ 1 - \sum_{k''} \left( T_{k''}^R \zeta_{k''} - T_{-k''}^{R*} \zeta_{-k''}^* \right) \exp(i\mathbf{k''}\cdot\mathbf{r}') \right\} = \tag{4.28}$$

$$\frac{1}{A} \int dr' \left| \exp[i(\mathbf{k'} - \mathbf{k})\mathbf{r}' - i\mathbf{k}\xi(\mathbf{r}')] \right| \left[ T_k^S - ik \cdot \beta\, T_{k'}^R \sum_{k'} \left( T_{k''}^R \zeta_{k''} - T_{-k''}^{R*} \zeta_{-k''}^* \right) \exp(i\mathbf{k''}\cdot\mathbf{r}') \right]$$

The summation term in the second parentheses arises from the differentiation of the exponential factor $\exp[-ik\xi_k(\mathbf{r}^0)]$ in (4.26).

Consider now the perturbation of the variance spectrum $F_k^0$ arising from the perturbation (4.27). At this point we make the essential assumption, which will enable us to close the moment equations, that the perturbations $\delta c_k$ for different wavenumbers are statistically independent of each other and are also statistically independent of the existing wave field. The assumption is justified by the Gaussian property of a surface wave field, which may be regarded as a superposition of an infinite number of statistically independent infinitesimal wave components. We shall follow up this concept explicitly later by regarding the surface wave field as being gradually built up from a zero sea state through the continual addition of statistically independent spectral increments.

Under the stated statistical assumptions, we obtain immediately the differential relation:

$$\delta F_k = < |\delta f_k^S|^2 > = \sum_{k'} < |M_{kk'}|^2 > \left( \frac{\delta F_{k'}}{2} - \frac{\delta F_{-k'}}{2} \right) \tag{4.29}$$

Before turning to the integration of equ. (4.29), we must first evaluate $< |M_{kk'}|^2 >$. The essential nonlinear terms in this computation arise from exponential expressions of the form $< \exp(ik(\xi(\mathbf{r}') - \xi(\mathbf{r}''))) >$. Since $\xi$ is a linear functional of $c$, its probability distribution is Gaussian, and the expectation value of the exponentials can therefore be determined analytically. The computation of $< |M_{kk'}|^2 >$ is given in (4.5) (Appendix).

Let us now construct the prescribed surface wave field by building up the spectrum $F(k)$ from zero to the final state through a linearly increasing continuum of wave fields $\hat{F}_k(\lambda) = \lambda F_k$ where $0 \le \lambda \le 1$, and $\delta \hat{F}_k = F_k \delta \lambda$. Denoting the associated SAR image spectrum and matrix $M_{kk'}$ in the intermediate state $\lambda$ similarly as $\hat{F}_k^S(\lambda)$, $\hat{M}_{kk'}(\lambda)$, respectively, equ. (4.29) then becomes

$$\frac{\hat{F}_k^S}{\lambda} = \sum_{k'} < |\hat{M}_{kk'}(\lambda)|^2 > \left( \frac{F_{k'}}{2} - \frac{F_{-k'}}{2} \right) \tag{4.30}$$

This can immediately be integrated with respect to $\lambda$ to yield

$$F_k^S = \sum_{k'} T_{kk'} \left( \frac{F_k}{2} + \frac{F_{-k}}{2} \right)' \tag{4.31}$$

where the transformation matrix

$$T_{kk'} = \left\langle \left| \overline{M}_{kk'} \right|^2 \right\rangle = \int_0^1 \left\langle \left| \widehat{M}_{kk'} \right|^2 \right\rangle d\lambda \tag{4.32}$$

The computation of $T_{kk'}$ is also given in the Appendix.

The final mapping relation (4.31) between the RAR and SAR image spectra is seen to be a quasi-linear transformation. The transformation matrix $T_{kk'}$ is in general a nonlinear function of the wave spectrum. In the limit of a very small wave spectrum, the relation becomes linear: $T_{kk'}$ becomes independent of the wave spectrum and diagonal. As the wave spectrum is gradually increased, $T_{kk'}$ develops off-diagonal terms and the matrix elements with high azimuthal wavenumber components are attenuated (azimuthal high wavenumber cut-off). This is discussed in more detail in the following section.

## 4.4 Structure of the transformation matrix $T_{kk'}$

In Section 4.5 ( Appendix) it is shown that the transformation matrix consists of the sum of two terms,

$$T_{kk'} = T_{kk'}^i + T_{kk'}^b \tag{4.33}$$

namely the 'filter transformation matrix'

$$T_{kk'}^i = A_{k, k'-k} \left| T_k^S \right|^2 \tag{4.34}$$

and the 'background transformation matrix'

$$T_{kk'}^b = B_{k,k'-k} (\widehat{\overline{P}}(\mathbf{r}) + T_1(\mathbf{r})) + C_{k,k'-k} \cdot T_2(\mathbf{r}) \tag{4.35}$$

where the coefficient matrices $A_{k, k'-k}$, $B_{k, k'-k}$ and $C_{k, k'-k}$ depend on integral properties of the wave field (cf. eqs (A.20) - (A.22)

82

The structure of the transformation matrices becomes clearer when it is recognized that the functions $\phi_n(\gamma)$, $\phi_I(\gamma)$ and $\phi_0(\gamma)$ ... eqs (A.15) – (A.17)) act as high azimuthal wavenumber cut-off filter functions which control the form of the coefficient matrices $A_{k,k'\cdot k}$ and $B_{k,k'\cdot k}$.

Consider first the filter transformation matrix $T'_{kk'}$. For $\gamma \to 0$, $\phi_0(\gamma) \to 1$ and equ. (A.11) yields $A_{k,k'\cdot k} \to \delta_{k \cdot k'}$. Thus in the limit of a very small azimuthal wavenumber $k_x$ or very small orbital velocities, this term reduces to the linear SAR imaging expression (4.23). As $\gamma$ is increased, the function $A_{k,k'\cdot k}$ is broadened with respect to the second variable $k' - k$. The wave component $k$ is thereby spread in the image spectrum into a band around $k$, and the energy of the band is attenuated. The spreading and attenuation increases with increasing azimuthal wavenumber $k_x$ and increasing orbital velocity.

The second term, the background transformation matrix $T^b_{kk'}$, vanishes entirely as the orbital velocity approaches zero. Thus in this limit equ. (4.33) reduces to the RAR imaging relation, as, of course, it must. For finite orbital velocities, the term $T^b_{k,k'}$ yields a background continuum. For $\gamma \to 0$, $\phi_2(\gamma) \to 1$ and $B_{k,k'\cdot k} \to \delta_{k\cdot k'}$, $C_{k,k'\cdot k} \to \delta_{k\cdot k'}$, so that the continuum degenerates in this limit to the quadratic sum and difference wavenumbers of the wave field, as expected for the lowest order quadratic interaction of a nonlinear process. For finite $\gamma$, the function $B_{k,k'\cdot k}$ is broadened with respect to the second index variable, so that all wave components contribute to the continuum.

## 4.5 (Appendix) Computation of $<|\widehat{M}_{k,k'}|^2>$ and $T_{kk'}$

From equ. (4.28) we obtain:

$$
M_{kk'}\Big|^2 = \lambda^{-2} \left| \int \int dr' dr'' \exp[i(k'-k)(r'-r'') - ik(\xi(r') - \xi(r''))] \right.
$$

$$
\left\{ \left| T^a_k \right|^2 - ik\beta \sum_{k''} \ell^R_{k''} \cdot \left[ T^a_{k'} T_{k'}^{*} \exp(ik''r'') - T^a_{k'}{}^* T_{k'} \exp(ik''r') \right] \right. \tag{A.1}
$$

$$
\left. - k_r^2 \beta^2 \left| T^a_{k'} \right|^2 \sum_{k'',k'''} \ell^R_{k''} \cdot (\ell^R_{k'''})^* \exp(i(k''r' - k'''r'')) \right\}
$$

53

where $I^R_k$ as in equ. (4.7)

To determine the expectation value $<|M_{kk'}|^2>$ we expand the exponential factor $exp(-ik(\xi(r') - \xi(r'')))$ with respect to a given pair of infinitesimal Fourier amplitudes $\zeta_{k''}$, $\zeta_{k'''}$ and their complex conjugate amplitudes $\zeta^*_{-k''}$, $\zeta^*_{-k'''}$. We have first

$$\xi(r') - \xi(r'') = \Delta\xi = \beta T^v_{k''}\zeta_{k''}(exp(ik''r') - exp(ik''r'')) + \beta T^v_{k'''}\zeta_{k'''}exp(ik'''r') - exp(ik'''r'')$$

$$+ \beta T^{v*}_{-k''}\zeta^*_{-k''}(exp(ik''r') - exp(ik''r'')) + \beta T^{v*}_{-k'''}\zeta^*_{-k'''}(exp(ik'''r') - exp(ik'''r'')) + \Delta\zeta_{rest} \quad (A.2)$$

$$= \Delta\zeta + \Delta\zeta_{rest}$$

where $\Delta\zeta$ contains the four infinitesimal Fourier components of interest and $\Delta\zeta_{rest}$ is the remaining field which contains no components at these wavenumbers.

Thus

$$exp(-ik\Delta\xi) = exp(-ik\Delta\xi_{rest})(1 - ik_r\Delta\xi - k_r^2/2(\Delta\xi)^2 + \quad (A.3)$$

The correlation of this expression with the amplitudes $\zeta_{k''}$, $\zeta_{k'''}$, $\zeta^*_{-k''}$, $\zeta^*_{-k'''}$ occurring in (A.1) then yields

$$< |M_{kk'}|^2 > = A^{-1}\int dr\, exp(i(k'-k)r) \quad (A.4)$$

$$\cdot < exp(-ik\Delta\xi(r))>\cdot(T_0 + T_1 + T_2)$$

where

$$T_0(r) = T_k^2 - \hat{P}(r) \quad (A.5)$$

is independent of the expansion of the exponent

$$T_1(r) = |\hat{P}(-r)(T_k^2)(T_k^2)' - \hat{P}(r)(T_k^2)'(T_2)| \quad (A.6)$$

$$(r = r' - r'', \quad r'' = r_0)$$

34

is derived from the linear term in the expansion of the exponential function,

$$\Gamma_2(\mathbf{r}) = - \quad T_{\mathbf{k}'}^{v} \stackrel{2}{\cdot} \hat{P}(\mathbf{r}) \cdot \hat{P}(-\mathbf{r}) \qquad (A.7)$$

is derived from the quadratic terms in the expansion of the exponential function, and

$$\hat{\hat{P}}(\mathbf{r}) = - k_i^2 \beta^2 \left| T_{\mathbf{k}'}^{v} \right|^2 \cdot \sum_{\mathbf{k}''} P_{\mathbf{k}''}^{R} \exp(i\mathbf{k}''\mathbf{r}) \qquad (P_{\mathbf{k}}^{R} \text{ as in equ (4.10)})$$

$$(A.8)$$

$$\hat{P}(\mathbf{r}) = \frac{k_i^2 \beta^2}{2} \sum_{\mathbf{k}''} \left[ (T_{\mathbf{k}''}^{c})^* \cdot T_{\mathbf{k}''}^{R} \cdot F_{\mathbf{k}''} - (T_{-\mathbf{k}''}^{v}) \cdot (T_{-\mathbf{k}''}^{R})^* \cdot F_{-\mathbf{k}''} \right| \left| \exp(i\mathbf{k}''\mathbf{r}) - 1 \right|$$

In deriving (A.4) - (A.8) we have set $\mathbf{r} = \mathbf{r}' \quad \mathbf{r}''$ in (A.1) and carried out one integration over $\mathbf{r}'$ for fixed $\mathbf{r}$, noting that for a statistically homogeneous wave field the integrand depends only on $\mathbf{r}$. We have also replaced $<\exp - ik\Delta\xi_{rest}>$ by $<\exp - ik\Delta\xi>$, since $\Delta\xi_{rest}$ and $\Delta\xi$ deviate by an infinitesimal quantity

$\hat{M}_{\mathbf{k}\,\mathbf{k}'}$ is obtained from $M_{\mathbf{k}\,\mathbf{k}'}$ by replacing $\xi_{\mathbf{k}}, \zeta_{\mathbf{k}}$ by $\lambda^2 \cdot \zeta_{\mathbf{k}}$ and $\lambda^2 \cdot \xi_{\mathbf{k}}$, respectively:

$$- \quad \hat{M}_{\mathbf{k}\mathbf{k}}(\lambda) \Big|^2 > = A^{-1} \left| d\mathbf{r} \exp(i(\mathbf{k}' - \mathbf{k})\mathbf{r}) \cdot \exp(- ik\lambda^2 \Delta\xi(\mathbf{r}) > \right.$$

$$\left( \left| T_{\mathbf{k}}^{S} \right|^2 - \lambda(\hat{\hat{P}}(\mathbf{r}) + T_1(\mathbf{r})) + \lambda^2 T_2(\mathbf{r}) \right) \qquad (A.9)$$

We need to determine still the expectation value of the exponential function,

$$\phi(\mathbf{k}, \mathbf{r}, \lambda) = < \exp - ik\lambda^2(\Delta\xi) > = \exp - ik_i\lambda \cdot \eta > \qquad (A.10)$$

where

$$\eta = \beta[c(\mathbf{r}') - c(\mathbf{r}'')] \qquad (A.11)$$

The variable $\eta$ is Gaussian with zero mean and known variance

$$\langle \eta^2 \rangle = \beta^2 \sum_{\mathbf{k}} \left\{ \left| T_{\mathbf{k}}^c \right|^2 (F_{\mathbf{k}} + \left| T_{-\mathbf{k}} \right|^2 F_{-\mathbf{k}}) \right\} \left| 1 - \cos \mathbf{k r} \right| \tag{A.12}$$

so that the function $\phi$ can be readily evaluated:

$$\phi(\mathbf{k}, \mathbf{r}, \lambda) = exp\left(-k_z^2 \lambda \langle \eta^2 \rangle / 2\right) \tag{A.13}$$

All terms occurring in equ. (A.1) have now been expressed directly in terms of the surface wave spectrum.

To determine the matrix $\Gamma_{\mathbf{kk'}} = \int \langle |\hat{M}_{\mathbf{kk'}}|^2 \rangle d\lambda$ occurring in the final expression (4.31) we need now only to integrate equ. (A.9) with respect to $\lambda$. This yields

$$T_{\mathbf{kk'}} = \lambda^{-1} \int d\mathbf{r} \, exp \, i(\mathbf{k'} - \mathbf{k}) \cdot \mathbf{r} \cdot \left[ \phi_0(\mathbf{k}, \mathbf{r}) \cdot \left| T_{\mathbf{k}}^S \right|^2 \right.$$

$$\left. + \phi_1(\mathbf{k}, \mathbf{r}) \cdot (\hat{\overline{P}}(\mathbf{r}) + T_1(\mathbf{r})) + \phi_2(\mathbf{k}, \mathbf{r}) \cdot T_2(\mathbf{r}) \right] \tag{A.14}$$

where

$$\phi_0(\mathbf{k}, \mathbf{r}) = \phi_0(\gamma) = \int_0^1 \phi(\mathbf{k}, \mathbf{r}, \lambda) d\lambda = \gamma^{-1}\left| 1 - exp(-\gamma) \right| \tag{A.15}$$

$$\phi_1(\mathbf{k}, \mathbf{r}) = \phi_1(\gamma) = 2 \int_0^1 \lambda \phi(\mathbf{k}, \mathbf{r}, \lambda) d\lambda = 2\gamma^{-2}\left| 1 - (1 + \gamma)exp(-\gamma) \right| \tag{A.16}$$

and

$$\phi_2(\mathbf{k}, \mathbf{r}) = \phi_2(\gamma) = \int_0^1 \lambda^2 \phi(\mathbf{k}, \mathbf{r}, \lambda) d\lambda = \gamma^{-3}\left( 2 - (\gamma^2 - \gamma - 2) \, exp(-\gamma) \right) \tag{A.17}$$

with

$$\gamma = k_z^2 \langle \eta^2 \rangle / 2 \tag{A.18}$$

Equation (A.14) may be written more compactly in the form

36

$$T_{kk'} = A_{k,k'-k} \left[ T_k^S \right]^2 + B_{k,k'-k} [\hat{\vec{P}}(r) + T_1(r)] + C_{k,k'-k} \cdot T_2(r) \tag{A.19}$$

where

$$A_{k,k'-k} = A^{-1} \int d\mathbf{r} \exp\left[ i(\mathbf{k'}-\mathbf{k})\cdot\mathbf{r} \right] \cdot \phi_0(\gamma) \tag{A.20}$$

$$B_{k,k'-k} = A^{-1} \int d\mathbf{r} \exp\left[ i(\mathbf{k'}-\mathbf{k})\cdot\mathbf{r} \right] \phi_1(\gamma) \tag{A.21}$$

and

$$C_{k,k'-k} = A^{-1} \int d\mathbf{r} \exp[i(\mathbf{k'}-\mathbf{k})\mathbf{r}] \phi_2(\gamma) \tag{A.22}$$

5    Analysis of SAR spectra

In this section we carry out an intercomparison of SEASAT SAR image spectra with model hindcast wave spectra and SAR image spectra computed from the hindcast wave spectra. Most of the analysis of this section is based on a selection of 32 digitally analyzed SAR scenes, listed in Section 5.1. However, we present in Section 5.2 also a brief review of a previous analysis of a significantly larger set of optically processed SAR images for the same SEASAT orbits (Lehner, 1984).

Theoretical SAR spectra were computed using the linear transformation approximation described in Section 4.2 (Section 5.3) and by Monte Carlo simulations using the full nonlinear mapping relations described in Section 4.3 (Section 5.5). In addition, empirical transfer functions were determined by fitting the SEASAT SAR image spectra to the hindcast model spectra using a power-law frequency dependent transfer function for each wave propagation direction (Section 5.4). The conclusions drawn from these various analysis techniques are summarized in Section 5.6

5.1    SAR scenes analyzed

A total of 32 digitally processed 6.4 km × 6.4 km SAR scenes from 7 orbits were spectral analyzed. To test for a possible dependence on the SAR incidence angle, 22 of these scenes were selected as pairs from the near and far edges of the 100 km wide SAR swath. The variance spectrum was computed at 25 m resolution (50 m Nyquist wavelength) to the full image wavelength limit and then subsequently averaged in the wavenumber domain with a top-hat weighting function extending over 5 × 5 wavenumber components (yielding 50 degrees of freedom)

The geographical positions and relevant characteristics of the scenes are given in Fig. 5.1 and Table 7, respectively. Orbits 757, 762, 785, and 791 correspond to the same meteorological period, while the remaining orbits correspond to essentially uncorrelated meteorological situations. It is apparent from the nonlinearity ('velocity bunching') parameters and principal wave propagation directions listed in the table (inferred from the model hindcast spectra) that the scenes cover a wide variety of imaging situations

| Image | Orbit | Scene | Time | LAT | LONG | WAM $H_s$ | ALT $H_s$ | nonlinearity vel.bunch. parameter | wave direction | azimuthal cut-off |
|---|---|---|---|---|---|---|---|---|---|---|
| 1 | Aug. 18 757 | 902 | 22:36 | 62°22' N | 6°57' W | 4.11 | 1.90 | strong 1.5 | azimuthal | SAR image mis-located |
| 2 | | 15601 N | 22:42 | 53°57' N | 17°5' W | 5.56 | 4.26 | strong 3.6 | azimuthal | strong |
| 3 | | 15604 F | 22:42 | 53°57' N | 17°5' W | 5.38 | 4.26 | | azimuthal-range | strong |
| 4 | | 15501 N | 22:43 | 50°59' N | 19°44' W | 4.01 | 3.91 | strong 1.4 | azimuthal-range | strong |
| 5 | | 15504 F | 22:43 | 50°59' N | 19°44' W | 4.01 | 3.91 | | range | |
| 6 | | 15301 N | 22:44 | 46°57' N | 22°55' W | 3.23 | 3.61 | strong 1.2 | range | strong |
| 7 | | 15304 F | 22:44 | 46°57' N | 22°55' W | 3.23 | 3.61 | | range | |
| 8 | | 9904 | 22:47 | 38°53' N | 27°47' W | 1.64 | 2.44 | medium 1.1 | range | medium |
| 9 | Aug. 19 762 | 523 | 05:40 | 60°12' N | 6°41' W | 3.98 | | strong 1.4 | range | weak |
| 10 | | 20401 N | 06:49 | 61°42' N | 9°30' W | 5.37 | | | azimuthal-range | ? |
| 11 | | 20404 F | 06:49 | 61°42' N | 9°30' W | 5.37 | | | azimuthal-range | |
| 12 | Aug. 20 785 | 6403 | 21:40 | 48°1' N | 3°43' W | 1.73 | 2.36 | 0.6 | | |
| 13 | | 7704 | 21:41 | 47°27' N | 4°10' W | 1.73 | 2.36 | 0.6 | | |

Table 7

89

| Image | Orbit | Scene | Time | LAT | LONG | WAM $H_s$ | ALT $H_s$ | nonlinearity vel.bunch. parameter | | wave direction | azimuthal cut-off |
|---|---|---|---|---|---|---|---|---|---|---|---|
| 14 | | 11004 | 21:41 | 46°44' N | 4°39' W | 1.73 | 2.36 | weak | 0.6 | range | weak |
| 15 | | 7601 | 21:41 | 46°26' N | 4°52' W | 1.66 | 2.36 | weak | 0.3 | | |
| 16 | | 7604 | 21:41 | 46°7' N | 5°30' W | 1.66 | 2.36 | | 0.3 | | |
| 17 | | 8006 | 21:43 | 40°7' N | 9°37' W | 1.94 | 2.40 | | 0.8 | | |
| 18 | | 8004 | 21:43 | 39°58' N | 9°4' W | 1.94 | 2.40 | | 0.8 | | |
| 19 | Aug. 21 791 | 2604 | 07:29 | 55°9' N | 8°37' W | 2.51 | 2.90 | medium | 1.6 | range | weak |
| 20 | | 701 | 07:25 | 59°8' N | 11°50' W | 2.75 | 2.97 | | 1.7 | | |
| 21 | Sept. 8 1044 | 1505 | 00:19 | 59°31' N | 14°13' W | 2.77 | | medium | 1.3 | azimuthal | weak |
| 22 | Sept. 19 1149 | 401 | 08:24 | 59°50' N | 1°25' W | 4.44 | 4.00 | strong | 2.2 | range | weak |
| 23 | Sept. 30 1359 | 25101 N | 01:16 | 63°55' N | 1°0' E | 4.02 | 4.00 | | 1.1 | | |
| 24 | | 25104 F | 01:16 | 63°55' N | 1°0' E | 4.02 | 4.00 | | 1.1 | two peaks 90° apart | strong |
| 25 | | 11204 F | 01:17 | 62°16' N | 1°13' W | 4.02 | 4.00 | medium | 1.1 | | |
| 26 | | 11204 N | 01:17 | 62°16' N | 1°13' W | 4.02 | 4.00 | | 1.1 | | |

Table 7

90

| Image | Orbit | Scene | Time | LAT | LONG | WAM $H_s$ | ALT $H_s$ | nonlinearity vel bunch. parameter | wave direction | azimuthal cut-off |
|---|---|---|---|---|---|---|---|---|---|---|
| 27 | | 29101 N | 01:18 | 60°02' N | 5°01' W | 3.52 | 3.23 | weak 0.98 | two peaks | ? |
| 28 | | 29104 F | 01:18 | 60°02' N | 5°01' W | 3.52 | 3.10 | | 180° apart | ? |
| 29 | | 13603 F | 01:19 | 58°33' N | 7°31' W | 4.14 | 3.50 | medium 1.1 | two peaks | |
| 30 | | 13603 N | 01:19 | 58°33' N | 7°31' W | 4.14 | 3.23 | | 180° apart | strong |
| 31 | | 29001 N | 01:19 | 55°56' N | 9°58' W | 5.9 | 2.46 | strong 2.84 | range | strong |
| 32 | | 29004 F | 01:19 | 55°56' N | 9°58' W | 5.9 | 2.46 | | | |

Table 7

91

## 5.2  General comparison with SEASAT SAR image spectra

A detailed comparison of the global wave hindcast with the 32 digitally processed SEASAT SAR images, including a discussion of SAR ocean wave imaging problems and the nonlinear surface wave-SAR image spectral mapping relations, is given in the following sections.

For a first overview we show in this section, in Figs 5 2 - 5 5, a comparison of the principal wave propagation directions inferred from the variance spectra of a larger number of analog processed SAR images (Lehner, 1984) with the Custer diagrams for the total sea, windsea and swell of the wave model hindcast. The SAR wave propagation rays (panels a) represent the propagation directions of the peak wavenumbers of the SAR spectra. The principal wave propagation directions inferred for the SAR image spectra show some general agreement with the wave model hindcast. However, a number of systematic deviations, to be discussed later, are also clearly evident: the SAR tends to detect long swell components more readily than the short windsea components, the SAR wave propagation direction is often strongly rotated towards the range direction (the SAR look direction orthogonal to the satellite flight direction), and range travelling waves are more easily detected than waves travelling in the azimuthal (satellite flight) direction.

One of the difficulties to be faced in using SAR wave data in a combined wind and wave data assimilation system will clearly be to decide whether discrepancies which are found between the SAR image spectra and the model wave spectra are due to the SAR imaging process or to errors in the input wind field (or the wave model itself) In the case of the altimeter, the situation is considerably simpler, as altimeter wave height measurements are relatively free of distortion and calibration uncertainties The effective use of SAR wave data will therefore be critically dependent on the development of reliable mapping relations defining the transformation of the surface wave spectrum to the SAR image spectrum. The inverse mapping, i e. the transformation from the SAR spectrum to the wave spectrum, has as yet not been addressed  The inverse transformation may be expected to be non-unique and probably singular Inversion techniques will need to be developed, using general inverse modelling methods, employing iterative corrections of the forward mapping relation. These questions will be discussed in more detail in Section 6  It is shown there that the SAR inversion problem may not need to be solved explicitly but can be imbedded in the more general inversion problem of determining the wind field modifications required to correct errors between predicted and observed wave data in a combined wind/wave

data assimilation system. However, it can be concluded already from Figs 5 2 - 5 5 that SAR image spectra clearly cannot be interpreted directly but only by comparison with SAR spectra computed from a wave model forecast, and that the assimilation of SAR spectra in models will require the development of rather sophisticated inverse modelling techniques.

## 5.3 Comparison with linear theory

Linear theory should be applicable if the nonlinearity parameter $C = C^{max} \cos\theta$ $\leq 1$. ($C$ is proportional to the ratio of the rms azimuthal displacement induced by the long wave orbital velocity to the dominant wavelength, cf. Section 4 2). Table 7 lists a number of cases for which this criterion is satisfied.

However, in practice it was found that linear theory gave unrealistic SAR spectra in all cases, analyzed, including cases with quite small values of $C$. Figs 5 6, 5 7 show two examples, corresponding to a strongly nonlinear situation (scene 15601, $C = 3\,6$) and the most 'linear' case of the set (scene 11004, $C = 0.6$). The image spectra are plotted in polar coordinates as frequency direction spectra $F(f, \theta)$, in accordance with the usual wave spectrum format, rather than as wavenumber spectra $E(\mathbf{k}) = F(f, \theta)\,f/2k^2$

In both cases the theoretical SAR spectrum shows a generally monotonic increase of the spectrum with increasing frequency, without a distinct spectral peak as found in the observed SAR spectra. The origin of this behaviour is readily identified: The theoretical velocity bunching SAR MTF is proportional to $f^3$ (cf. Section 4 2) Thus $F_{SAR}(f, \theta)/F_{wave}(f, \theta) \sim f^6$ Since the wave model hindcast spectra typically exhibit a high frequency dependence $\sim f^{-4}$, the SAR spectra increase monotonically as $f^2$ for high frequencies. A SAR peak is visible at low frequencies only if the wave spectral peak is sufficiently sharp that it overrides the $f^6$ factor, i.e. if

$$f\,\frac{\partial F_{wave}}{\partial f}(f, \theta) < -6F_{wave}(f, \theta) \tag{5 1}$$

for some frequency on the rear slope of the peak. This is seldom observed, even for swell spectra (Bruning et al , 1988, computed such cases for theoretical swell spectra represented by the JONSWAP formula with very high peak enhancement factors $\gamma = 10$).
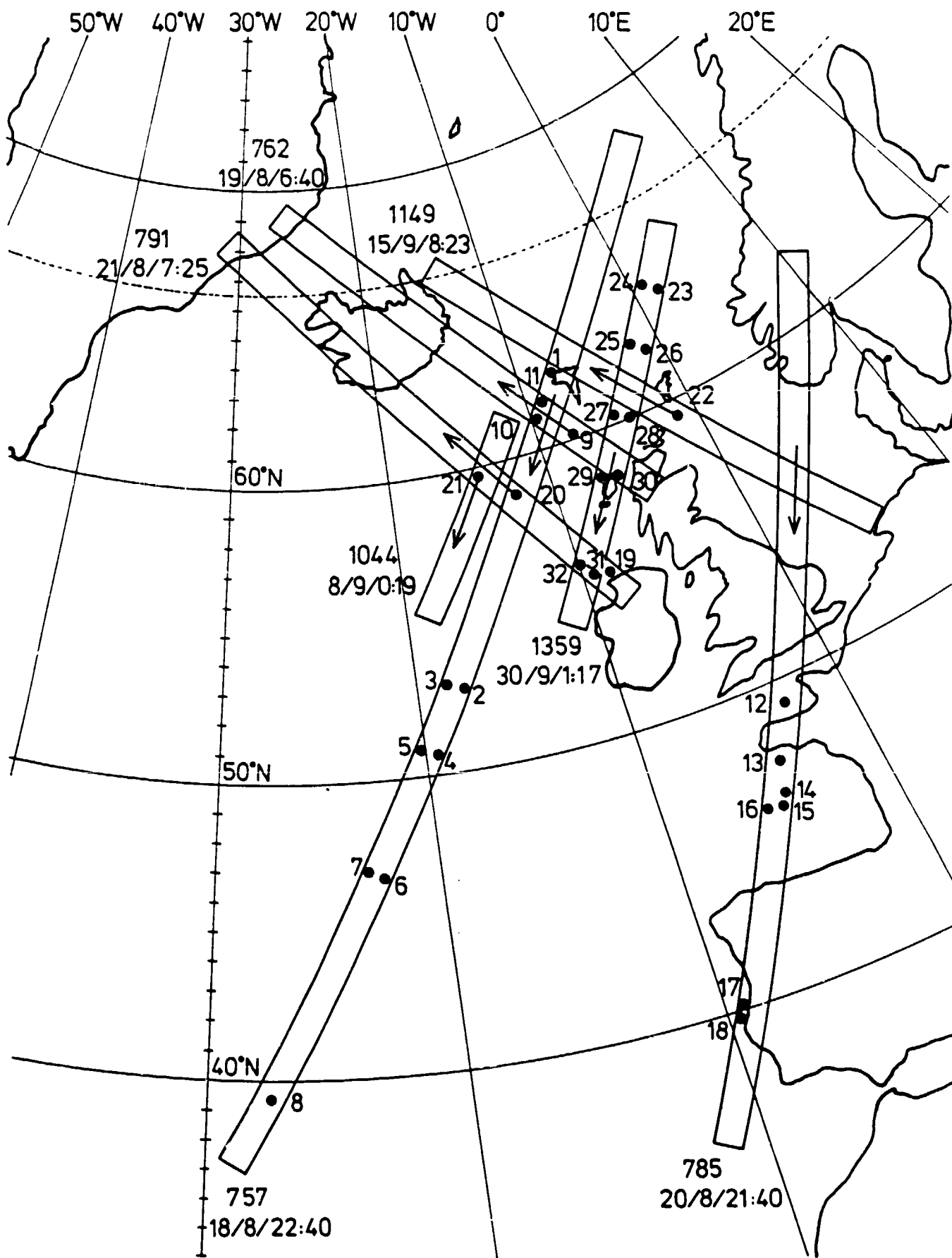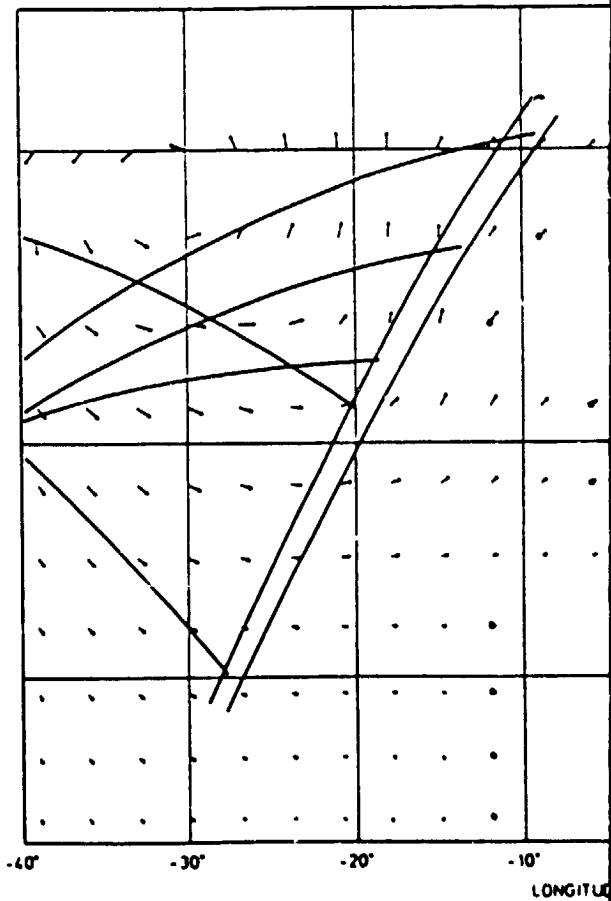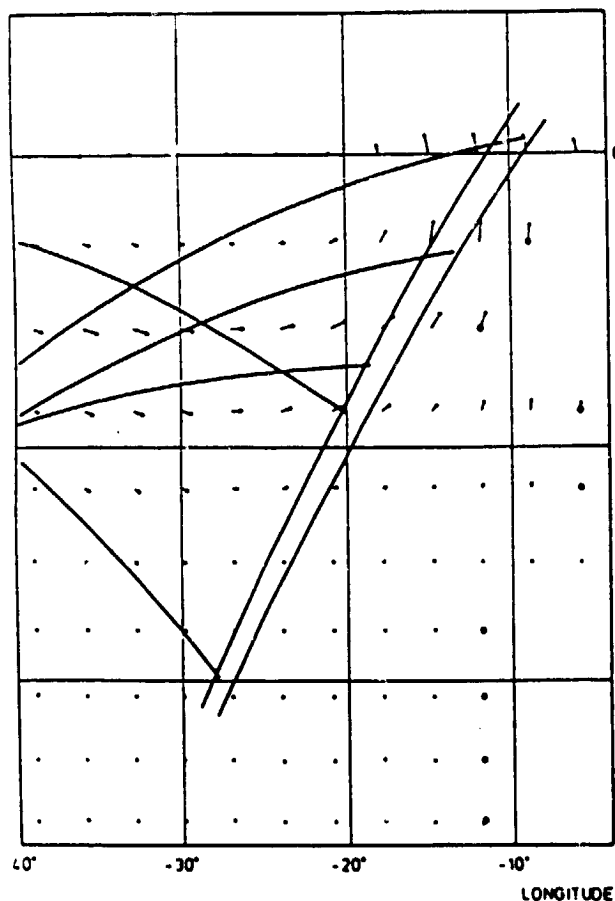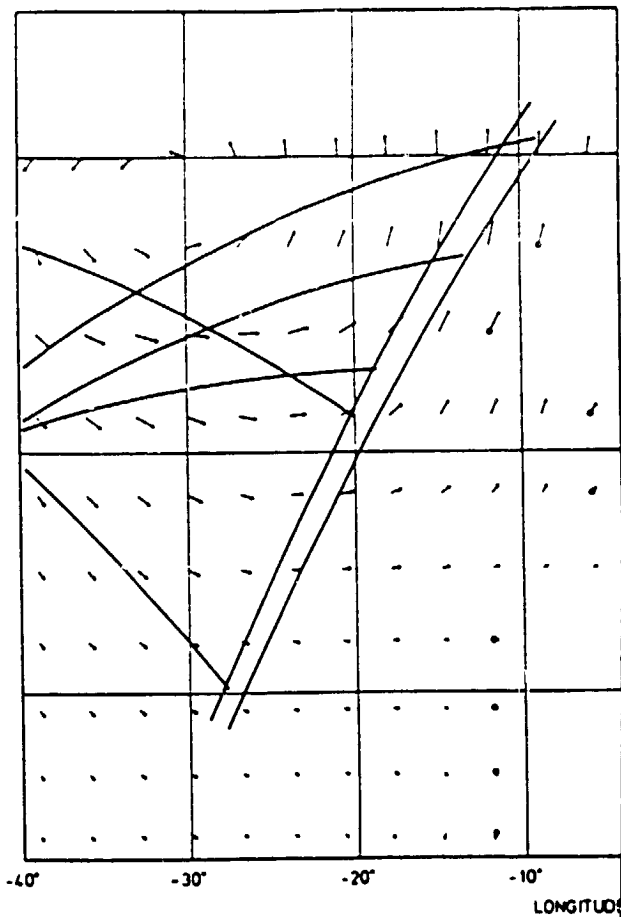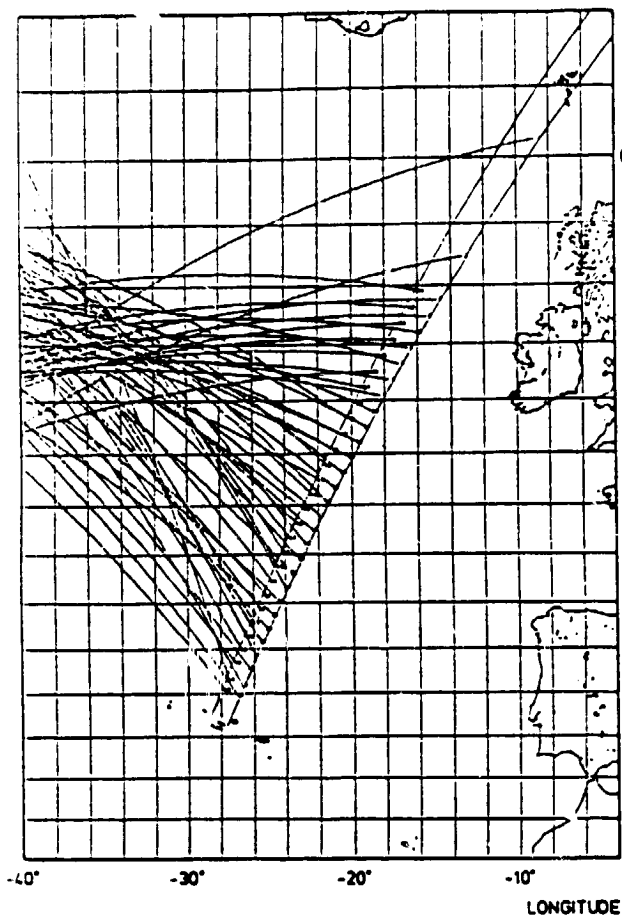
Fig. 5.2    Ray diagram (panel (a)) constructed by Lehner (1984) from peak wave-
numbers of SEASAT SAR image spectra along orbit 757, August 18, 1978,
22:40, with superimposed Custer diagrams of wave model hindcast for total
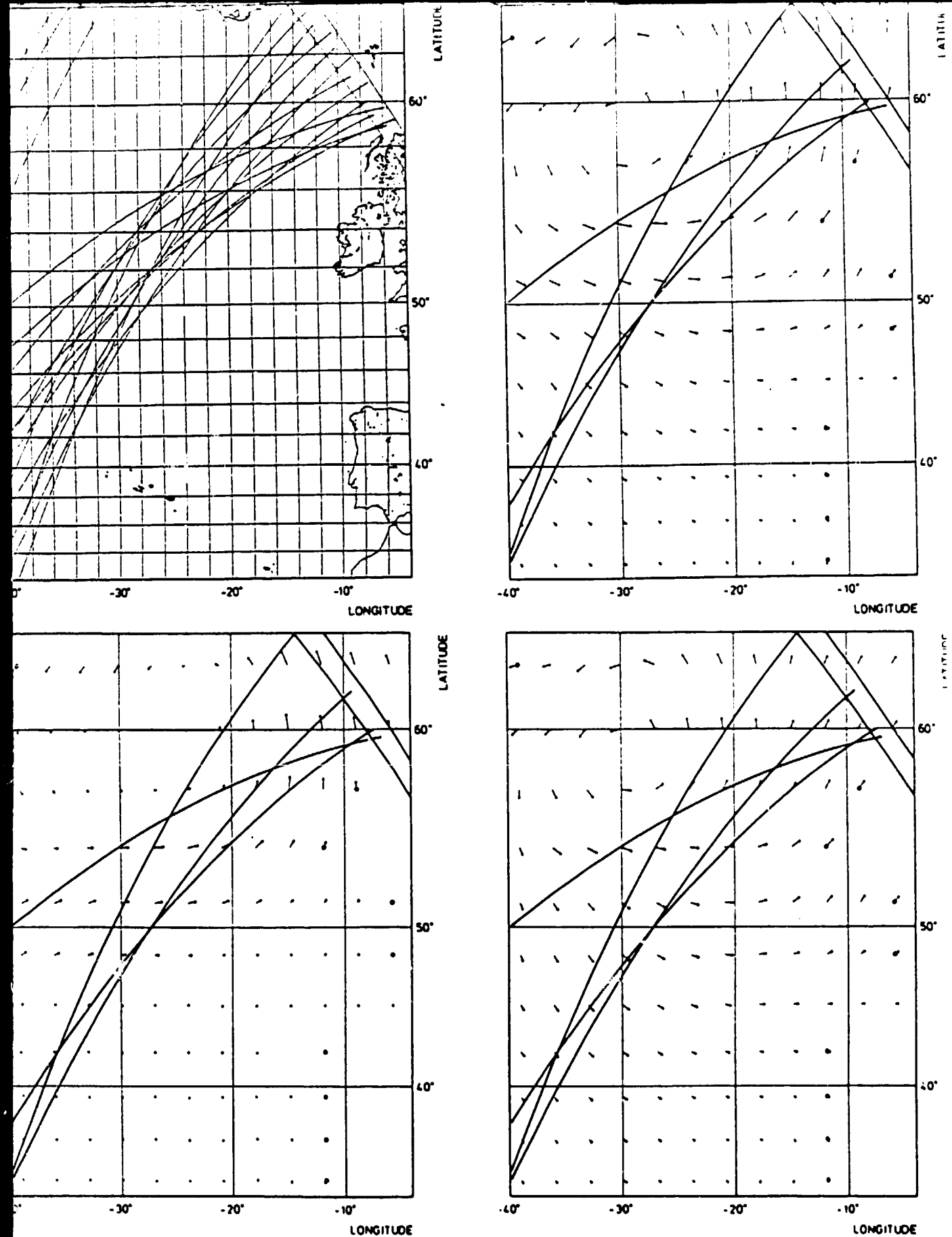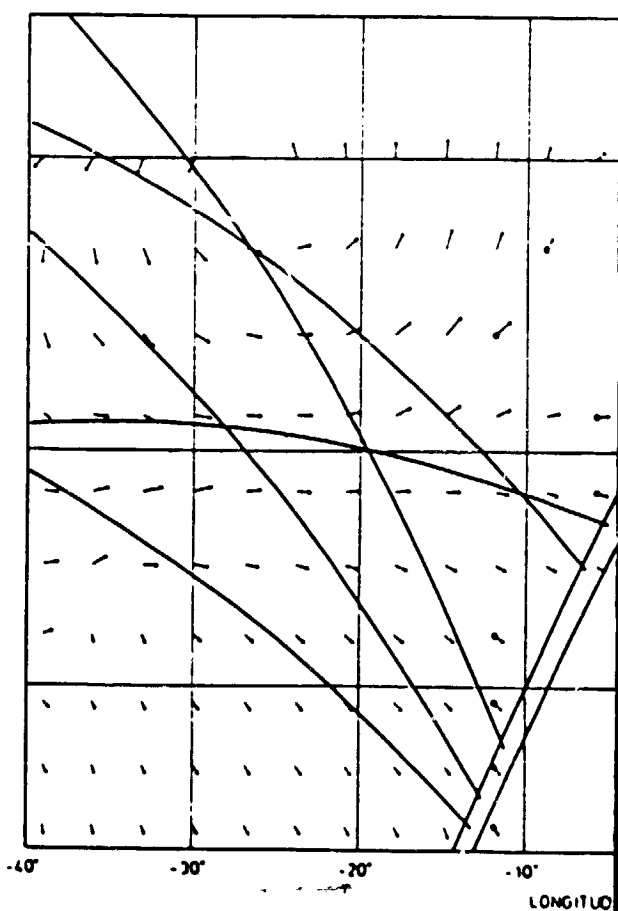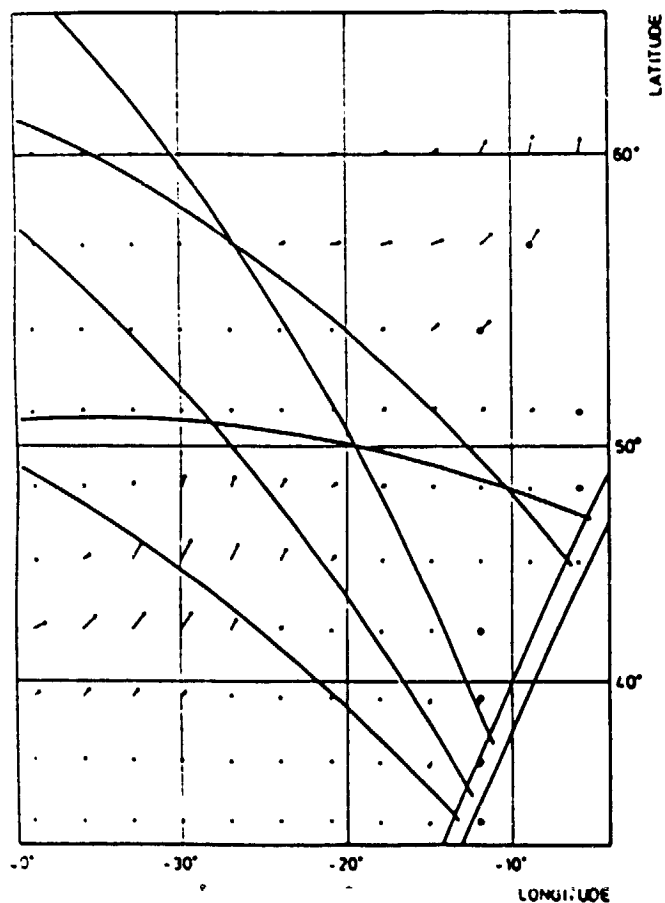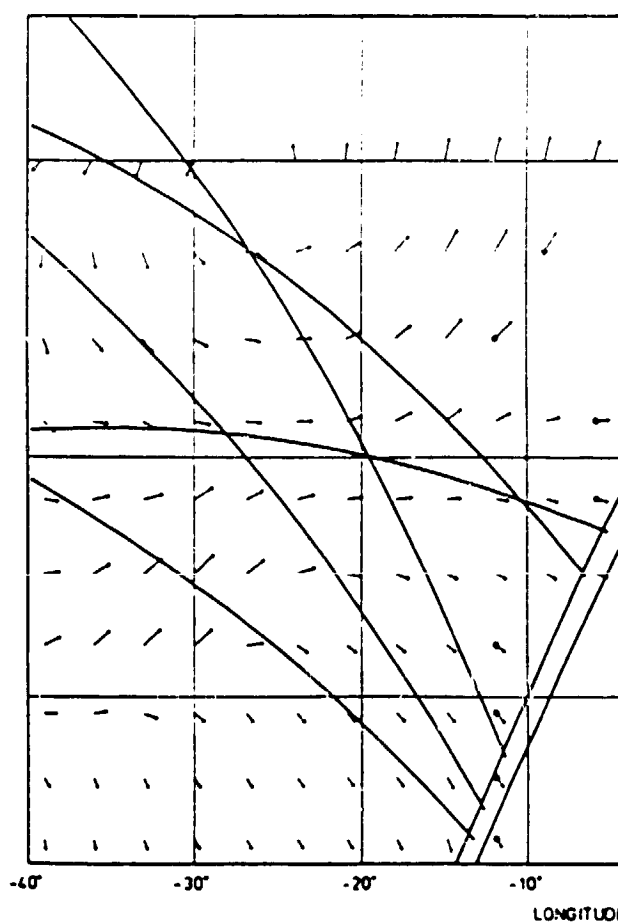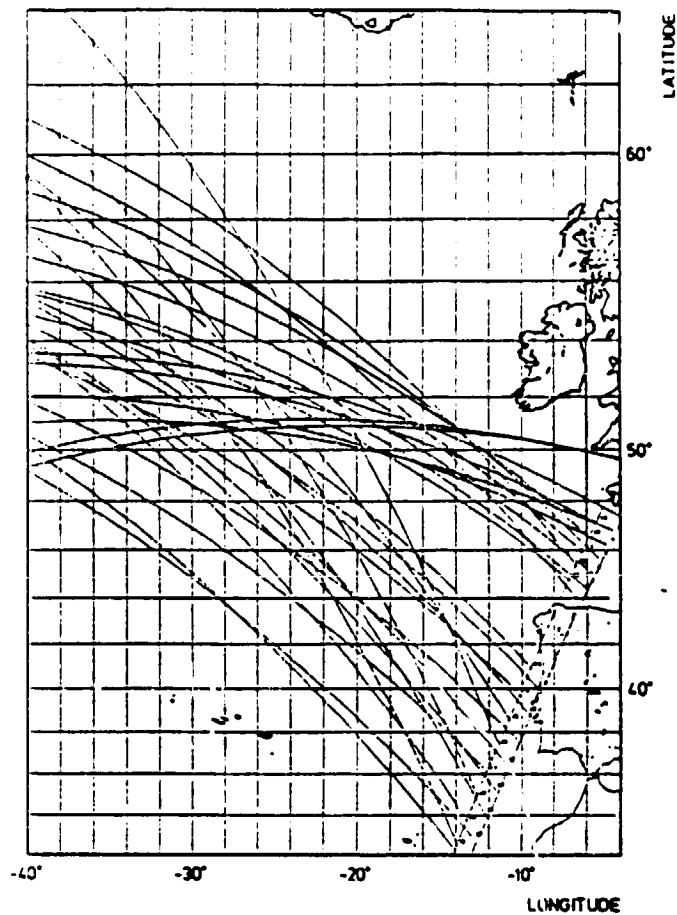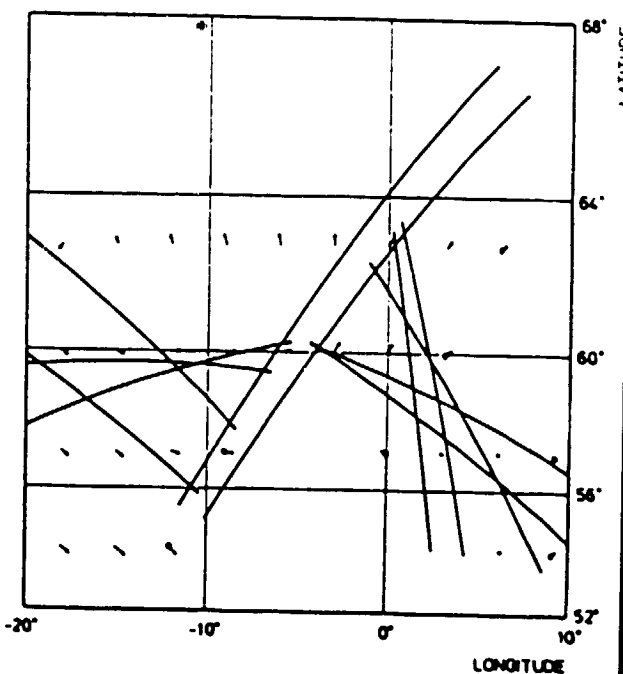wave field (panel (b)), windsea (panel (c)), and swell (panel (d))

Fig. 5.3    Ray diagram (panel (a)) constructed by Lehner (1984) from peak wave-
numbers of SEASAT SAR image spectra along orbit 762, August 19, 1978,
06 40, with superimposed Custer diagrams of wave model hindcast for total
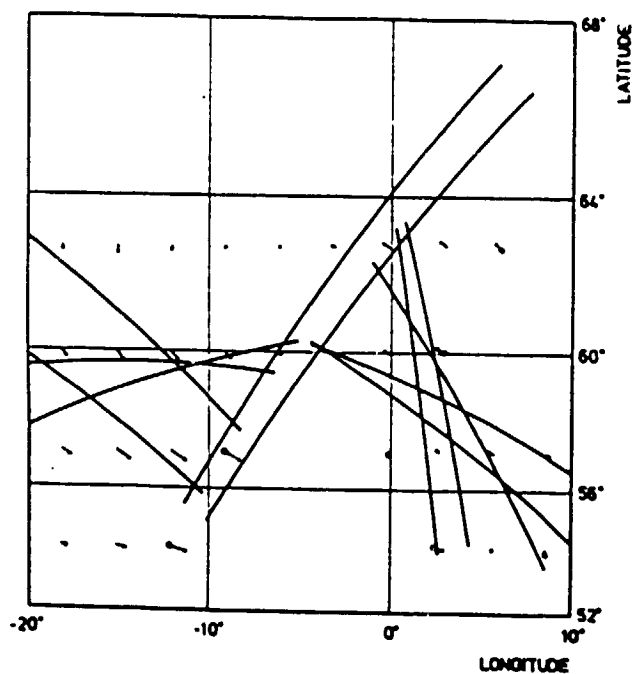wave field (panel (b)), windsea (panel (c)), and swell (panel (d)).
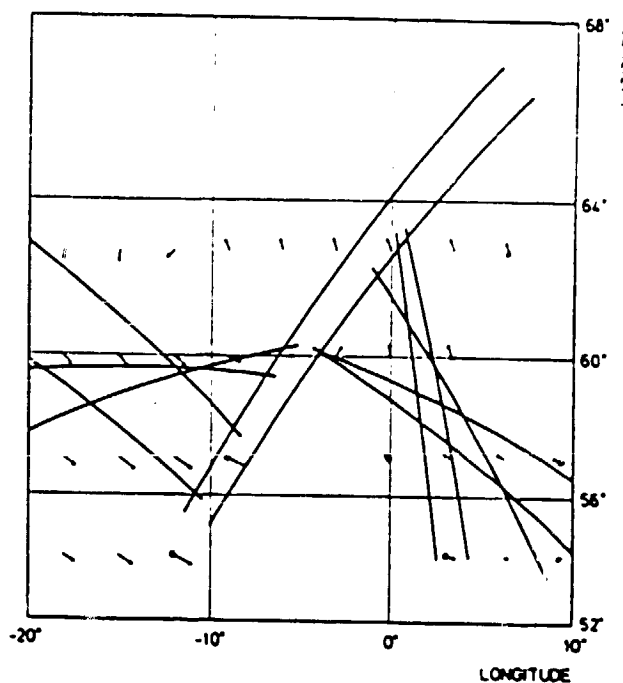
96

Fig. 5.4      Ray diagram (panel (a)) constructed by Lehner (1984) from peak wave-
             numbers of SEASAT SAR image spectra along orbit 785, August 20, 1978,
             21:40, with superimposed Custer diagrams of wave model hindcast for total
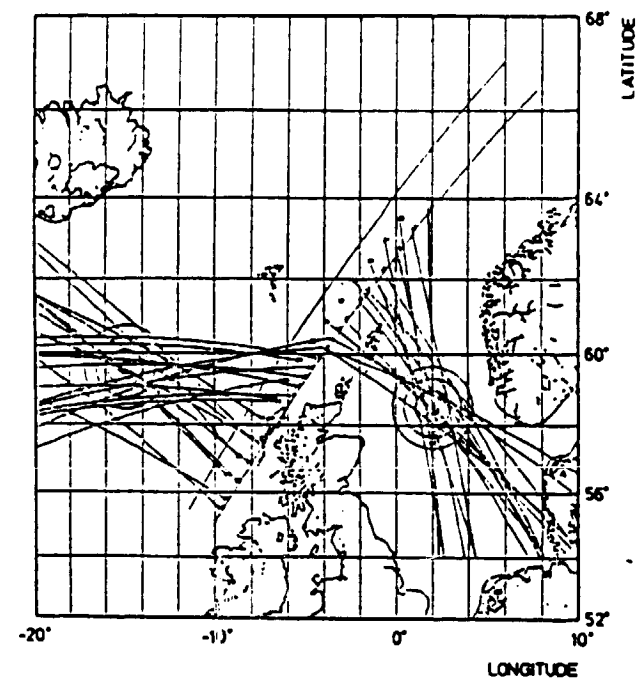             wave field (panel (b)), windsea (panel (c)), and swell (panel (d)).

97

**Fig. 5.5**     Ray diagram (panel (a)) constructed by Lehner (1984) from peak wave-
numbers of SEASAT SAR image spectra along orbit 1359, September 30, 1978,
01:17, with superimposed Custer diagrams of wave model hindcast for total
wave field (panel (b)), windsea (panel (c)), and swell (panel (d))

WAM MODEL SPECTRUM
DATE 78./08./18. 22:20.
LOCATION : LATITUDE 54.0°N LONGITUDE 342.0°E
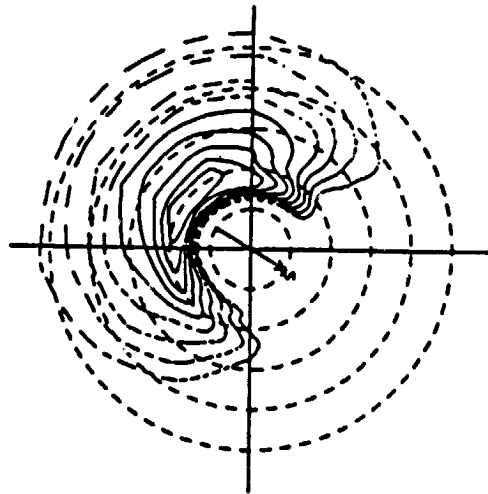
SAR SPECTRUM: ORBIT 757. SCENE 15601.
DATE 78./08./18. 22:42.
LOCATION : LATITUDE 53.°57.'N LONGITUDE 17.°).'W
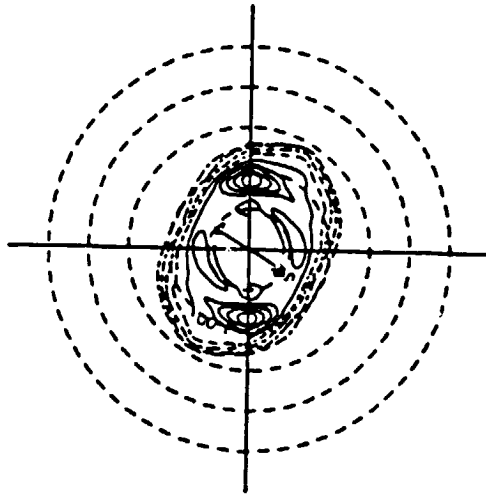
TRANSFORMED MODEL SPECTRUM
DATE 78./08./18. 22:20.
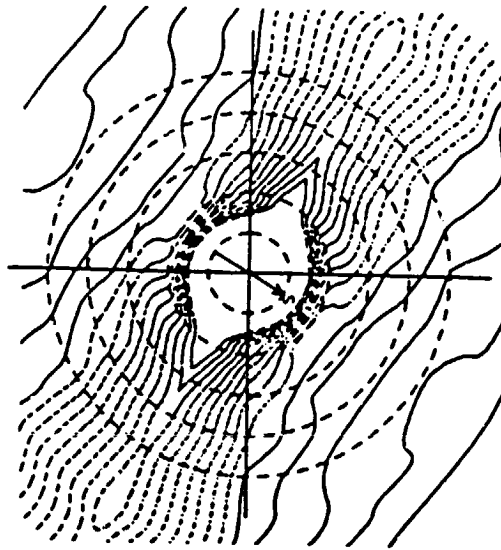LOCATION : LATITUDE 54.0°N LONGITUDE 342.0°E

Fig 5 6     Observed SAR spectrum, wave hindcast spectrum and theoretical linear
imaged SAR spectrum for SAR scene 15601 (strongly nonlinear, $r = 3.6$)

TRANSFORMED MODEL SPECTRUM
DATE 78./08./20. 21.:40.
LOCATOIN : LATITUDE 48.0°N LONGITUDE 354.0°E

SAR SPECTRUM: ORBIT 785. SCENE 11004.
DATE 78./08./20. 21.:41.
LOCATION : LATITUDE 46.°44.'N LONGITUDE 4.°39.'W

WAM MODEL SPECTRUM
DATE 78./08./20. 21.:40.
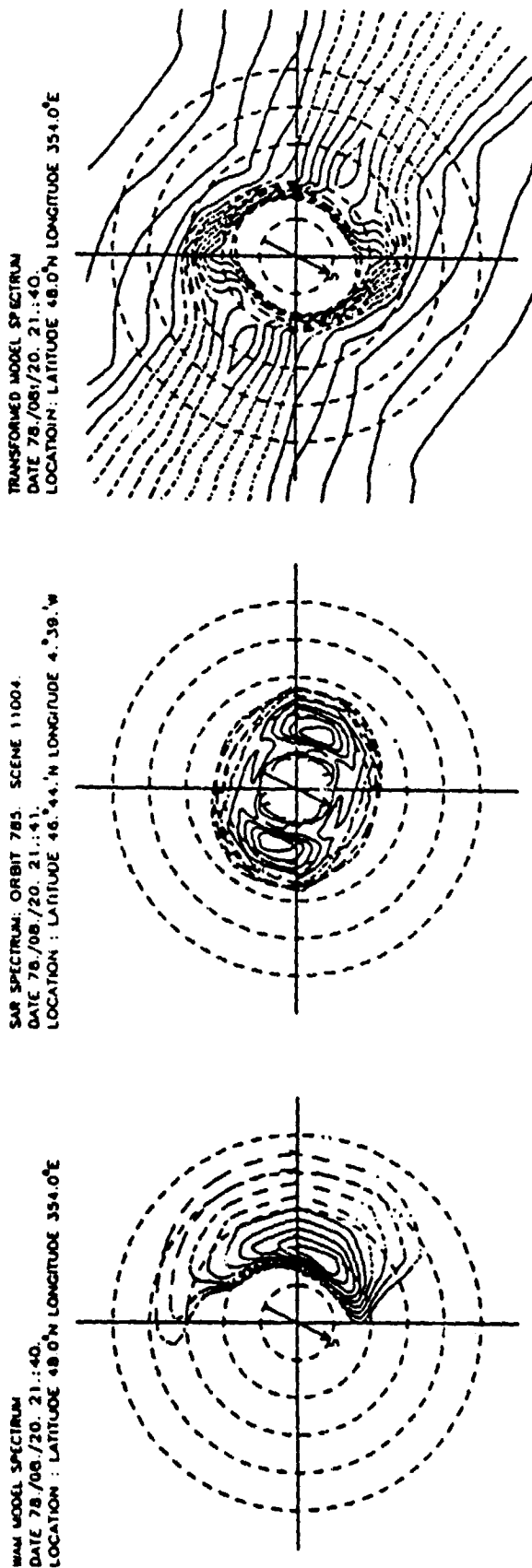LOCATION : LATITUDE 48.0°N LONGITUDE 354.0°E

Fig 5.7    Observed SAR spectrum, wave hindcast spectrum and theoretical linear
imaged SAR spectrum for SAR scene 11004 (linear, $r = 0.6$)

The failure of linear theory to reproduce the observed shape of the spectrum is not in contradiction with the theoretical range of validity of the theory. Linear theory breaks down for short wave lengths of the same scale as the rms azimuthal displacement. The azimuthal displacements associated with these components become smeared out by the superimposed displacements of the dominant long waves, which shift the small scale velocity bunching pattern back and forth relative to the phase of the short waves. The peak occurs in the SAR spectrum in the region of transition from the linear to the nonlinear regime. On the low frequency side of the peak, linear theory is still applicable. However, to test the linear theory quantitatively in this regime would require an investigation with calibrated images, which was not attempted in the present study. (This would not require an absolute calibration of the SAR, as the SAR image is defined as the modulation image with respect to the background white noise clutter image. However, it would require a more detailed investigation of the reference clutter spectrum than was undertaken here.)

## 5 4 Empirical transfer function fits

It is of interest to investigate whether the SAR image spectrum can be related to the surface wave spectrum through an empirical linear transfer function. Although we have seen that the purely linear theory is generally inapplicable for the full spectrum, it has been argued that the principal effect of the orbital motion is the velocity spread term, which can be represented by a linear azimuthal cut-off filter function (cf Beale, 1983). Also, the exact nonlinear transformation expression (4 2) derived in Section 4 has a quasi-linear (although non-diagonal) form

Accordingly, empirical MTFs were determined for a set of 26 SAR spectra (six of the cases listed in Table 7 could not be analysed as the scenes were received too late) by least square fitting the free parameters $A$ and $n$ in a power-law ansatz of the form

$$F_{SAR}(f, \theta) = A(\theta) \left( \frac{f}{f_i} \right)^{n(\theta)} \left| F_{cute}(f, \theta) + F_{cons}(f, \theta - 180) \right|$$ (5 2)

where the reference frequency $f_0$ was held fixed at 0 1 Hz

Figs 5 8, 5 9 show two typical examples of the observed and fitted SAR spectra, together with wave model hindcast spectra and the directional dependence of the fitted parameters $A(\theta)$, $n(\theta)$ In nearly all cases quite satisfactory fits were obtained The exponents $n(\theta)$ of the power laws were negative throughout, typically varying

between - 5 and - 10, in contrast to the predictions of the purely linear theory. This is presumably due to the smearing of the modulation of the shorter waves by the superimposed azimuthal displacements induced by the longer waves, as discussed above, which produces an attenuation of the shorter waves. This velocity bunching effect generally produces a significant attenuation of the spectrum already in the intermediate scale range shortly to the right of the wave spectrum peak, whereas the azimuthal cut-off due to the velocity spread term becomes effective only at higher wavenumbers (cf. Section 4).

Fig. 5.10 shows the dependence on wave propagation direction $\theta$ relative to the satellite flight direction of the mean values and the standard deviation of the exponent $n(\theta)$ for the 26 cases studied. The ratio of the standard deviation to the mean (the scatter index) is clearly too great for these empirical MTF fits to be applied in practice as a method for predicting the SAR spectrum. However, they do summarize in a single form the main characteristics of the shape of the SAR spectrum in the energy containing range relative to the wave spectrum.

A closer inspection of the data indicated that the scatter seen in Fig. 5.10 cannot be significantly reduced by a stratification of the data with respect to the nonlinearity parameter $C$ or other spectral parameters. We conclude from this and the previous section that a reliable interpretation of SAR image spectra must be based on realistic computations of the full nonlinear mapping of the two-dimensional wave spectrum into the SAR image spectrum.

## 5.5 Monte Carlo computations

The numerical computation of the closed nonlinear integral transform expression (4.31) relating the surface wave spectrum to SAR image spectrum could not be implemented within the present project. This is planned for a follow-up study project. It is anticipated that the technique, when implemented, will be more accurate and efficient than the Monte Carlo methods used hitherto. For the present project numerical computations of the nonlinear spectral transformation based on the same general SAR imaging expression (4.20) were carried out using the existing Monte Carlo technique (Alpers and Brüning, 1986; Brüning et al., 1988).

WAM MODEL SPECTRUM: ORBIT 757.   SCENE 15601.
DATE 78./08./18. 22.:20.
LOCATION : LATITUDE 54.°N LONGITUDE 342.°W
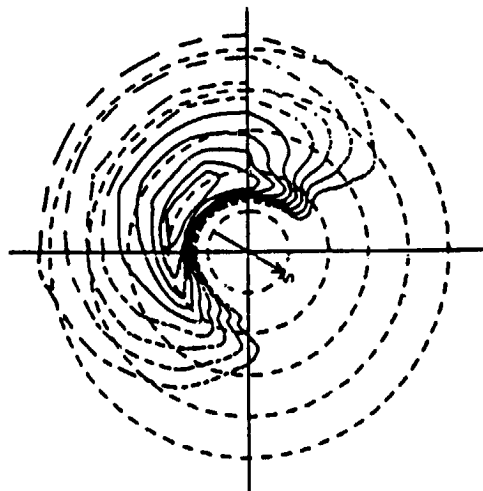
SAR SPECTRUM: ORBIT 757.   SCENE 15601.
DATE 78./08./18. 22.:42.
LOCATION : LATITUDE 53.°57.'N LONGITUDE 17.°5.'W
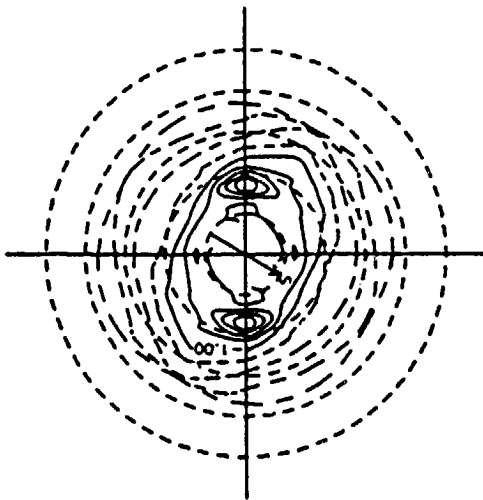
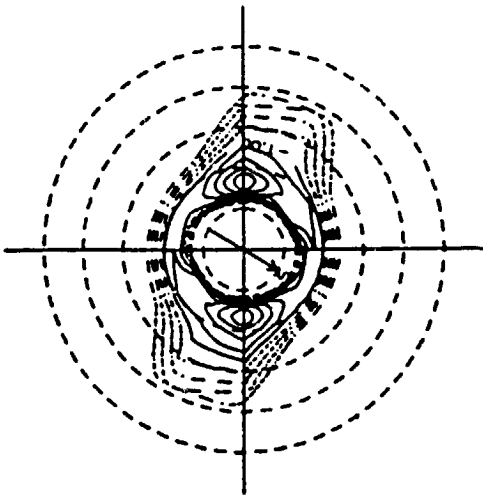TRANSFORMED MODEL SPECTRUM:ORBIT 757.   SCENE 15601.

Fig 5.8 a       Observed and empirically fitted SAR spectra, together with wave spectrum
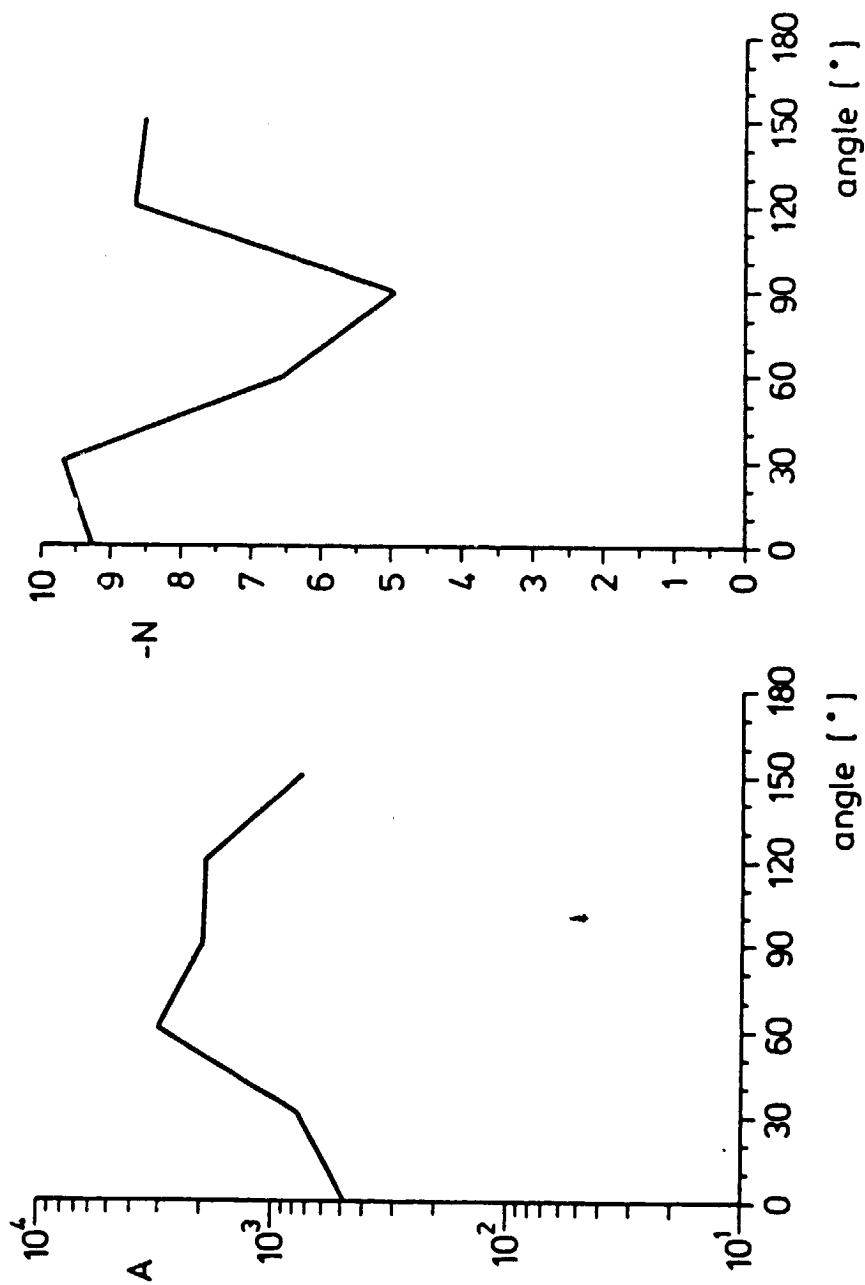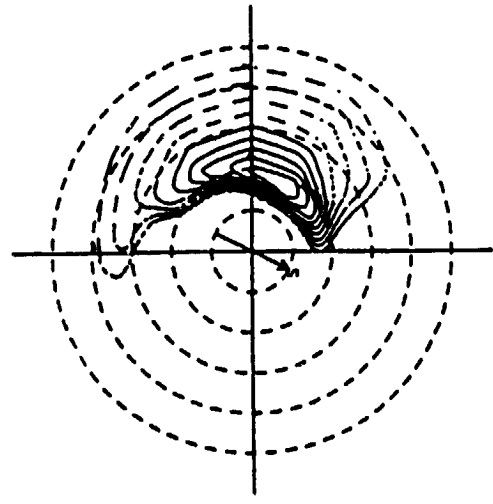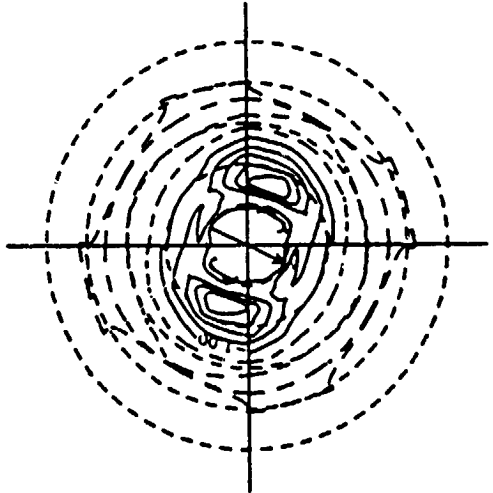                for SAR scene 15601.

103

Fig. 5.8 b    Observed and empirically fitted SAR spectra, together with fitting parameters
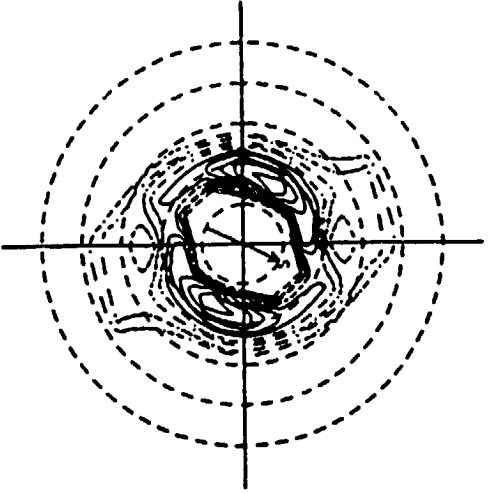$A(\theta)$, $n(\theta)$ for SAR scene 15601

WAM MODEL SPECTRUM: ORBIT 785.   SCENE 11004.
DATE 78./08./20. 21.:40.
LOCATION : LATITUDE 48.°N LONGITUDE 354.°W

SAR SPECTRUM: ORBIT 785.   SCENE 11004.
DATE 78./08./20. 21.:41.
LOCATION : LATITUDE 48.°44.'N LONGITUDE 4.°39.'W

TRANSFORMED MODEL SPECTRUM : ORBIT 785.   SCENE 11004.

Fig 5 9 a          Observed and empirically fitted SAR spectra, together with wave spectrum
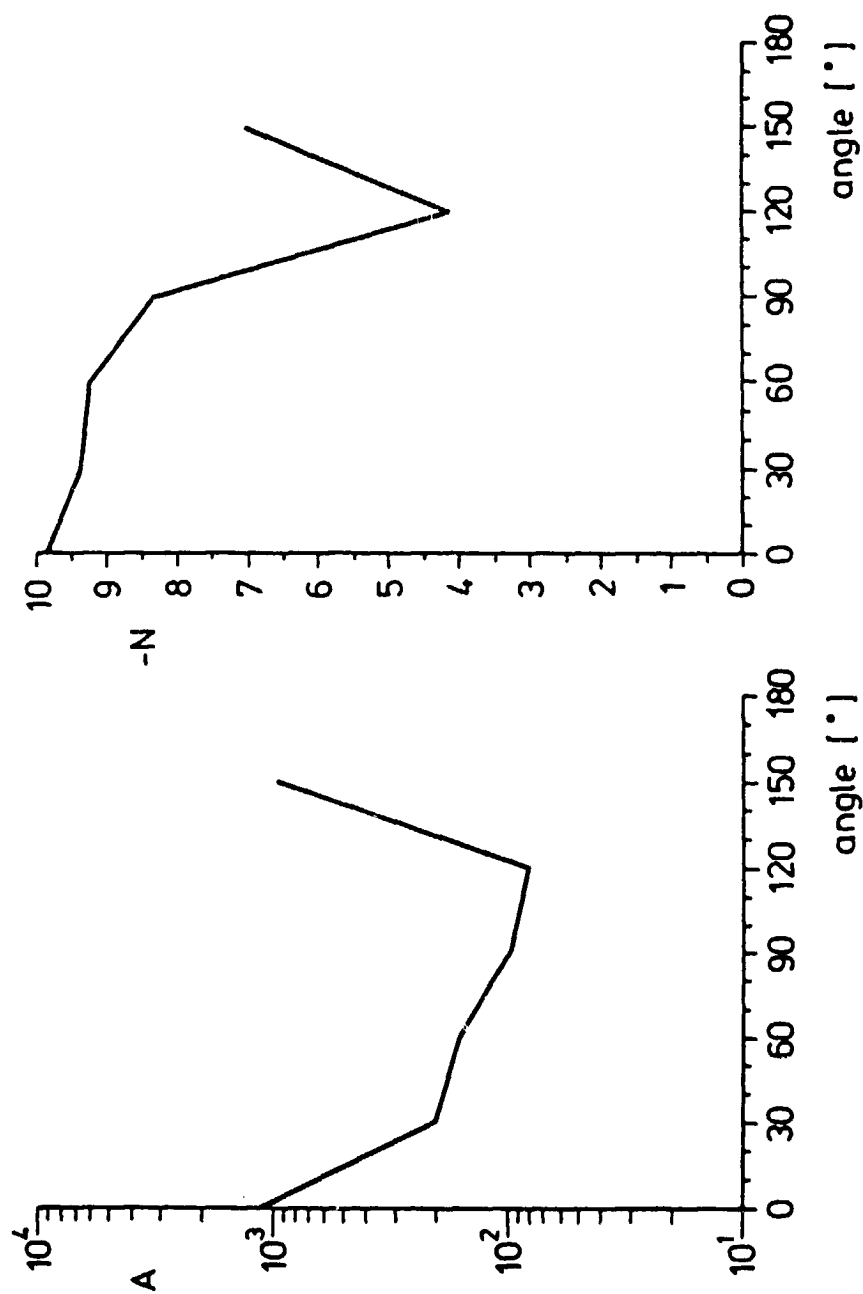                   for SAR scene 11004

105

Fig 5.9.b    Observed and empirically fitted SAR spectra, together with fitting parameters
$A(\theta)$, $n(\theta)$ for SAR scene 11004
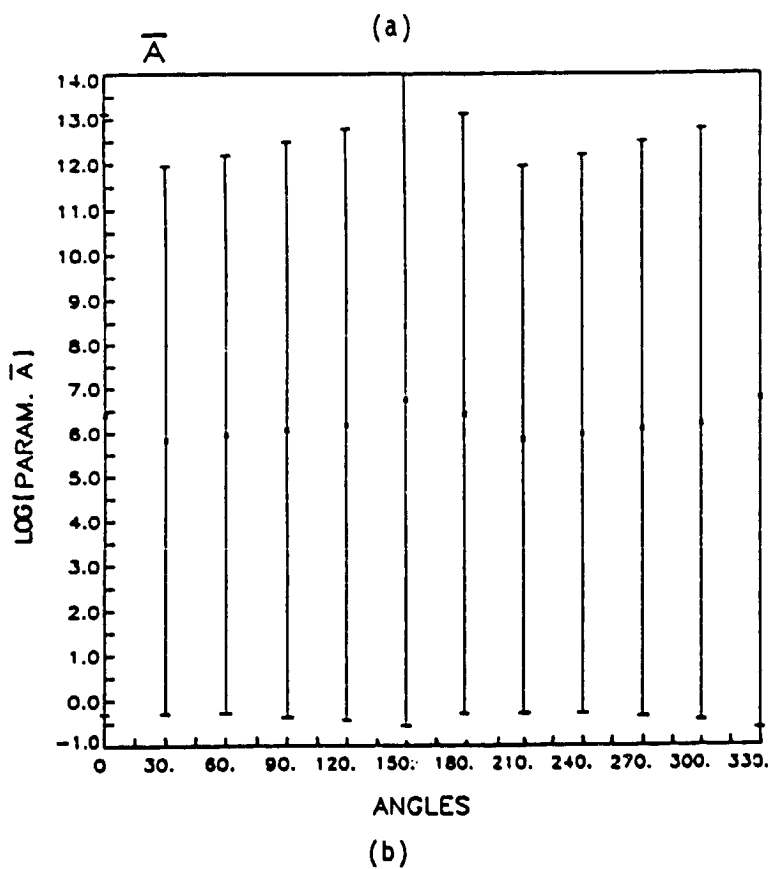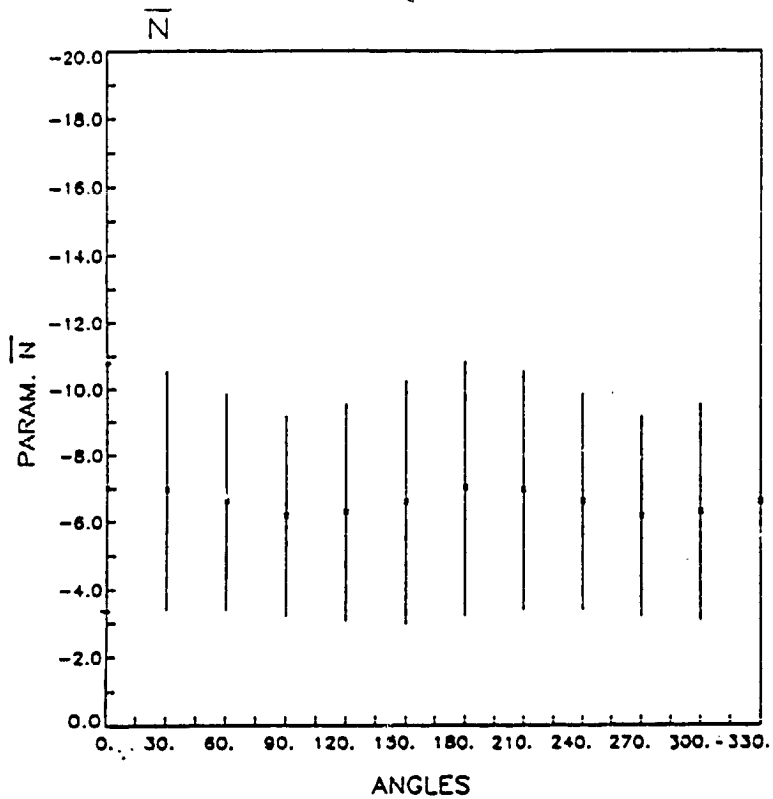
<u>Fig. 5.10</u>         Mean value and standard deviation of the empirical MTF exponent $n(\theta)$ as function of the wave propagation direction $\theta$ relative to the satellite flight direction for the 25 cases studied.

Fig. 5.11a-j shows a comparison of observed and computed SAR spectra, together with the wave model hindcast spectra used for the Monte Carlo computations. The selected set of SAR spectra covers a representative cross-section of the 26 cases studied (cf. Tabel 7). The examples include range and azimuthally travelling waves, weakly and strongly nonlinear imaging regimes and single and multiple peaked spectra.

The agreement between the observed and simulated spectra is generally quite remarkable. The significant distortions of the original wave spectrum appearing in the SAR spectrum, in particular the pronounced azimuthal cut-off, is well reproduced in the simulations. The propagation directions and wavelengths of the peaks in the simulated and observed SAR spectra also agree quite well. A somewhat earlier azimuthal cut-off is generally found in the simulated spectra than in the observed SAR spectra This could indicate a rather too high energy level in the high frequency region of the wave model spectrum.

The sequence Fig. 5.11, panels a, b, c, and d, give a good example of the change in character of the spectral distortion as one progresses through a region of azimuthally travelling waves to a region of range travelling waves along orbit 757 (cf. Figs 5.1 and 5.2). The discrepancies seen in Fig. 5.2 between the mean propagation directions of the model wave hindcast and the propagation rays inferred by Lehner (1984) from the peak wavenumbers of the SAR spectra are clearly due to the azimuthal cut-off in the SAR spectrum of the predominantly azimuthally travelling waves along the north-eastern segment of the orbit

Although it is encouraging that the nonlinear SAR imaging theory is able to reproduce the principal features of the observed SAR spectra, Fig 5 11 also illustrates the problems one faces in assimilating SAR image spectra in wave models: the loss of information for azimuthally travelling waves, the $180°$ directional ambiguity (Fig 5 11, panel j, gives a good example of two wave fields propagating in opposite directions which are merged together in the SAR spectrum), and the pronounced distortion of the spectrum. None the less, the potential information content of the two-dimensional SAR spectrum is clearly greatly superior to a single scalar number, such as the significant wave height, for example, or even a one-dimensional frequency spectrum, if effective techniques for the appropriate exploitation of this information can be developed. (It should be noted in this context that SAR wave image spectra are independent of absolute SAR calibration uncertainties: The spectra are 'self-normalized' by the clutter background level.)
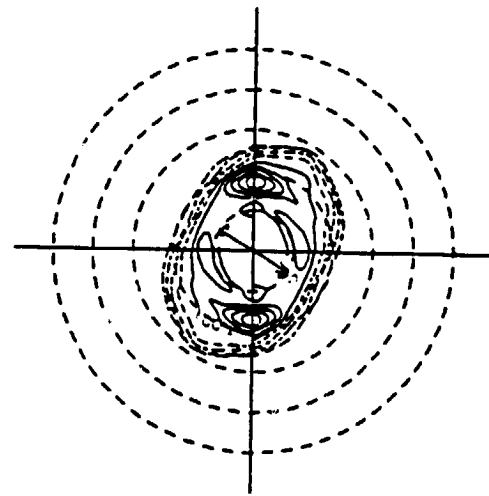
SIMULATED SAR SPECTRUM
DATE 78./08./18. 22.:20.
LOCATION : LATITUDE 54.0°N LONGITUDE 342.0°E
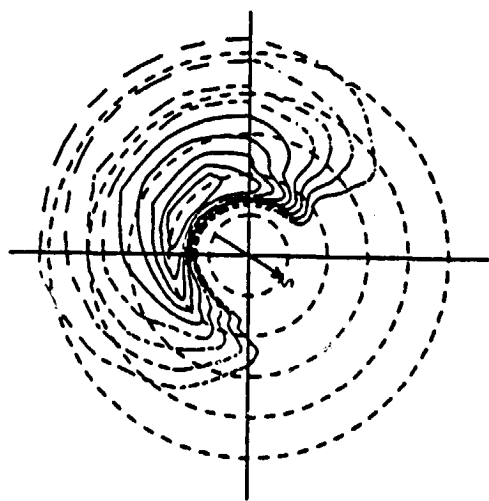
SIMULATED SAR SPECTRUM
DATE 78./08./18. 22.:20.
LOCATION : LATITUDE 51.0°N LONGITUDE 339.0°E
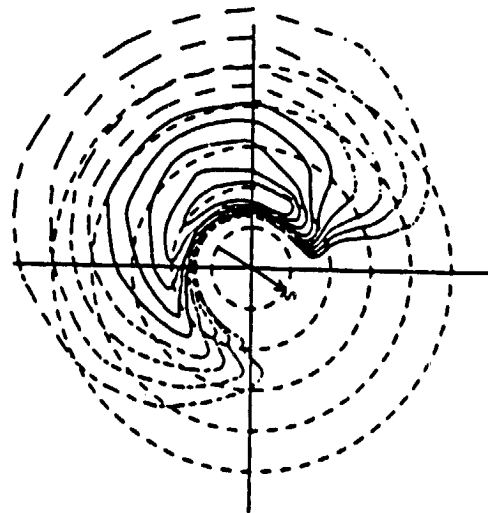
SAR SPECTRUM: ORBIT 757. SCENE 15601.
DATE 78./08./18. 22.:42.
LOCATION : LATITUDE 53.°57.'N LONGITUDE 17.°5.'W

SAR SPECTRUM: ORBIT 757. SCENE 15501.
DATE 78./08./18. 22.:41.
LOCATION : LATITUDE 50.°59.'N LONGITUDE 19.°44.'W

WAM MODEL
DATE 78./08./18. 22.:20.
LOCATION : LATITUDE 54.0°N LONGITUDE 342.0°E

WAM MODEL
DATE 78./08./18. 22.:20.
LOCATION : LATITUDE 51.0°N LONGITUDE 339.0°E

(a)

(b)

Fig 5.11    Examples of observed SAR spectra, wave model hindcast spectra and SAR spectra derived from the wave spectra by Monte Carlo computations
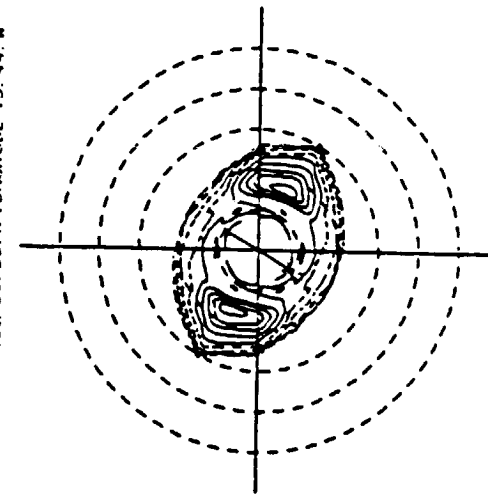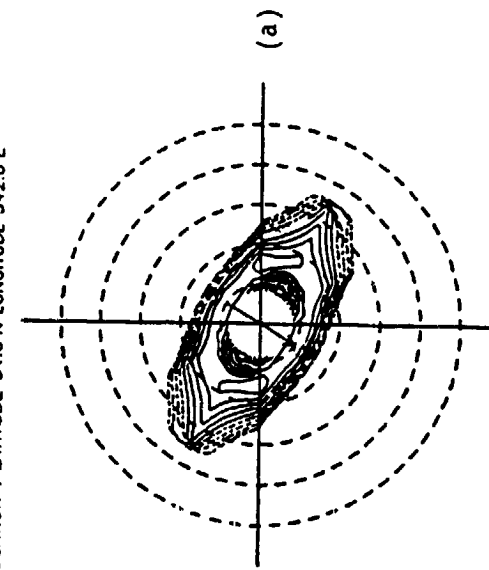
109

(c)

(d)

SIMULATED SAR SPECTRUM
DATE 78./08./18. 22.:20.
LOCATION : LATITUDE 39.0°N LONGITUDE 333.0°E

SAR SPECTRUM: ORBIT 757.    SCENE 9004.
DATE 78./08./18. 22.:47.
LOCATION : LATITUDE 38.°53.'N LONGITUDE 27.°47.'W

WAVE MODEL
DATE 78./08./18. 22.:20.
LOCATION  LATITUDE 39.0°N LONGITUDE 333.0°E

**Fig 5.11**    Examples of observed SAR spectra, wave model hindcast spectra and SAR
spectra derived from the wave spectra by Monte Carlo computations

110

Fig 5.11    Examples of observed SAR spectra, wave model hindcast spectra and SAR spectra derived from the wave spectra by Monte Carlo computations.
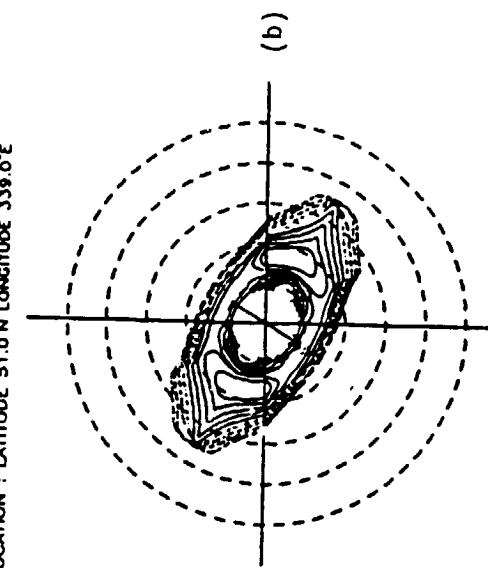
111
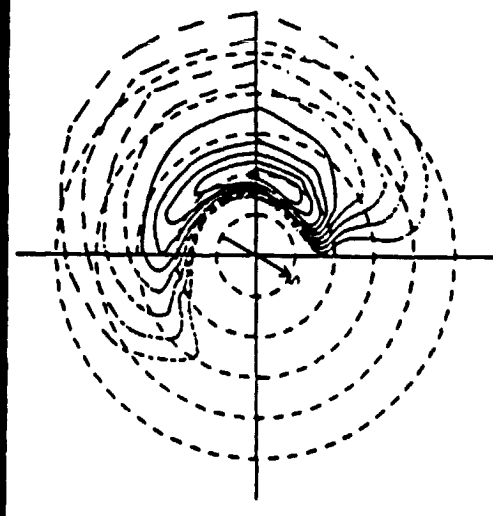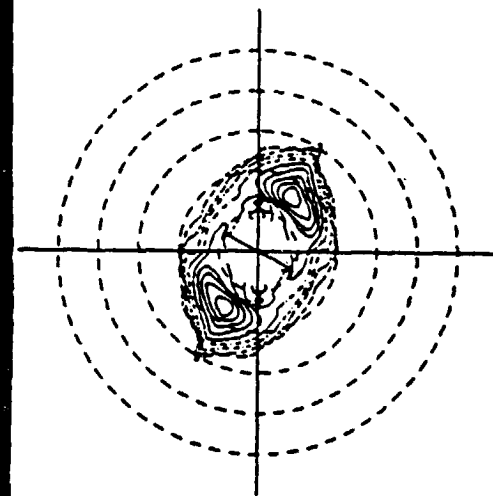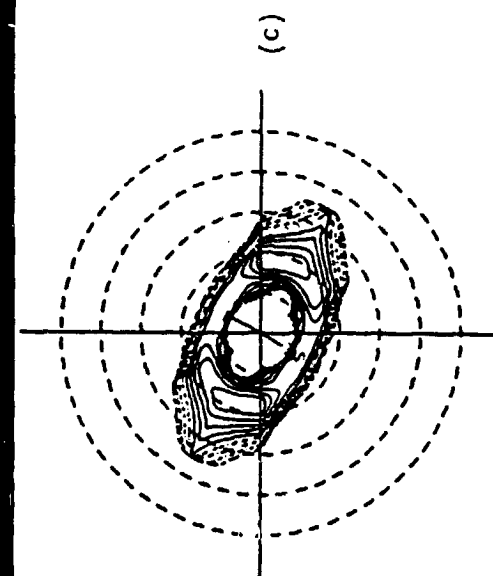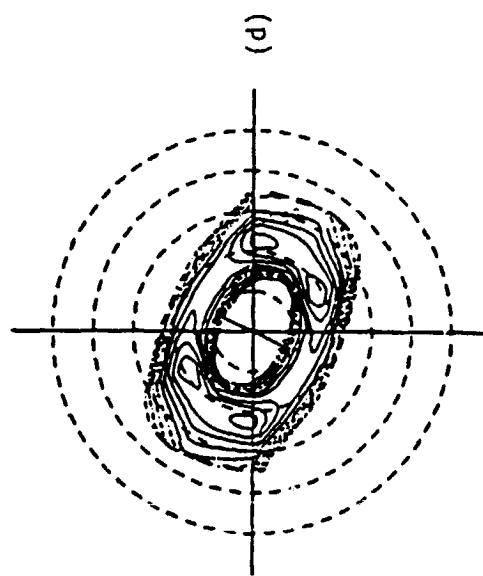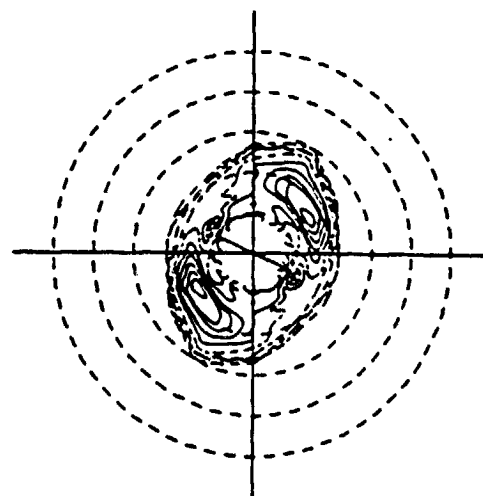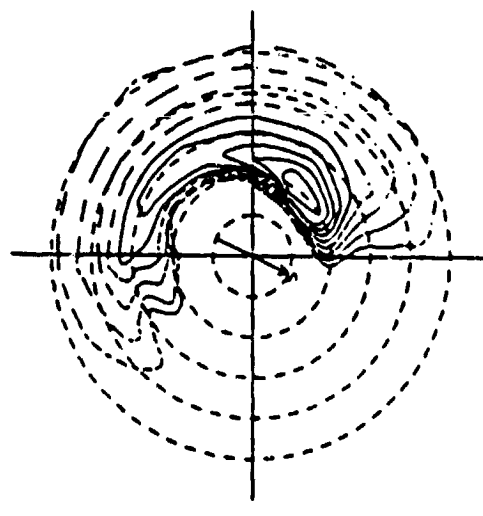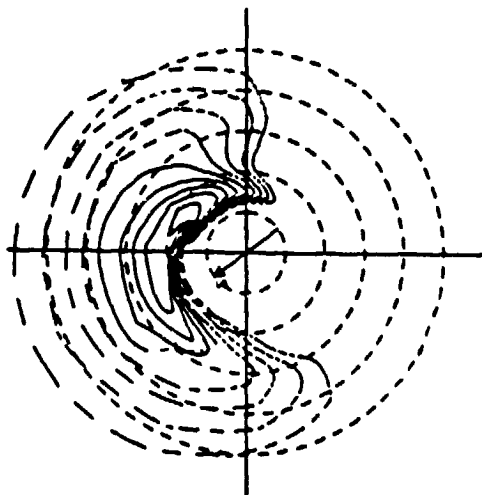
Fig 5.11    Examples of observed SAR spectra, wave model hindcast spectra and SAR
spectra derived from the wave spectra by Monte Carlo computations

112

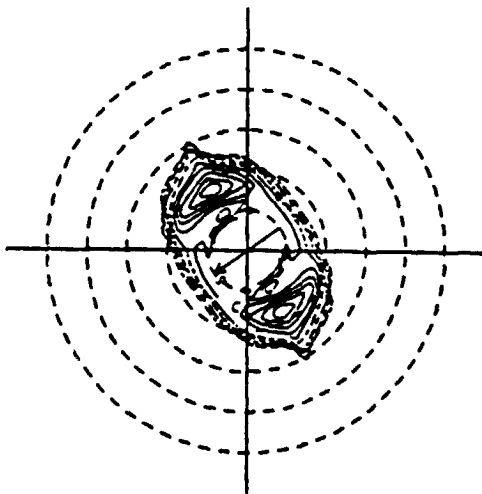Fig 5.11    Examples of observed SAR spectra, wave model hindcast spectra and SAR spectra derived from the wave spectra by Monte Carlo computations

113

## 5 6  Conclusions

The principal conclusion to be drawn from our SAR studies may be summarized as follows:

(1)  The linear SAR imaging theory is not able to reproduce the shape of the observed SAR image spectrum, even for low energy sea states. This is due to the unrealistic amplification of short waves by the linear theory, which results in a monotonically increasing SAR spectrum. In reality, the higher wavenumbers (often beginning shortly after the spectral peak) are attenuated by nonlinear interactions with the motion induced azimuthal displacements of the longer waves For low energy sea states with small nonlinearity parameter $C_{max}$, the observed peak in the SAR spectrum represents the transition from the linear to the nonlinear imaging regime

(2)  In nearly all cases, the observed SAR spectra can be well reproduced by applying individually fitted, directional dependent power law MTFs to the hindcast wave spectrum. However, the parameters derived from individual fits show considerable scatter from case to case. Thus this method does not appear suitable as a general empirical tool for relating wave spectra to SAR image spectra

(3)  SAR spectra computed from hindcast wave spectra using Monte Carlo simulation techniques showed a remarkable agreement with observed SAR spectra  Since the nonlinearly distorted SAR spectrum can differ significantly from the original wave spectra, and the distortions depend critically on the detailed structure of the wave spectrum, a meaningful interpretation of SAR wave image spectra can be based only on numerical computations of the exact nonlinear transformation relations

(4)  Starting from the well tested theory describing the nonlinear mapping of the ocean wave scene into the SAR image plane which was applied in the Monte Carlo simulations, a closed nonlinear integral expression was derived for the transformation of the wave spectrum into the SAR image spectrum  Since Monte Carlo computations are too time consuming to be applied operationally for the analysis of all ERS-1 SAR wave mode data (approximately 1 minute computing time per spectrum on a CRAY X-MP), the numerical implementation of the new expression should be pursued and tested with high priority as a possible alternative for application to ERS-1

(4)   The problem of the inverse transformation from the SAR image spectrum to the
      surface wave spectrum has not yet been addressed. Since different backscattering
      elements can be mapped on to the same image pixel, the inversion is in general
      non-unique and singular. The inversion problem must therefore presumably be
      treated locally in the form of a perturbation about a given forward
      transformation. This implies that the operation of a wave model, which can
      provide the first guess wave field needed as input for the forward
      transformation, is an essential pre-requisite for the extraction of useful wave
      information from SAR image spectra. The optimal implementation of the
      inversion procedure will depend on the form in which the SAR wave data is
      assimilated in the overall wind and wave data assimilation system in development
      for ERS-1, which is discussed further in the following section.

## 6.  Data assimilation

As outlined in the introduction, the present study represents a first step towards the
planned implementation of a comprehensive wind and wave data assimilation system for
ERS-1. A characteristic feature of this system is the joint analysis of both wind and wave
data, with consideration of the cross coupling between wind and wave information in the
different ERS-1 sensor systems and in the assimilation procedure itself. In this study only a
small sub-set of the questions to be addressed in the implementation of the full system will
be considered. In the following sub-section 6.1 we discuss briefly the general problem of
assimilating wave data in wave models and the information which can be extracted from
wave data, via a wave model, for the wind field. In Section 6.2 we present a simple example
of the improvement in a wave forecast obtained by assimilating SEASAT altimeter wave
height data.

### 6.1  General considerations

In contrast to atmospheric data assimilation, which has a fairly long history
beginning with the introduction of numerical weather prediction, wave modellers
have only recently begun to address the problem of assimilating wave data in wave
models (cf studies by Thomas (1988), Komen (1985), Janssen et al. (1988). This is partly
due to the lack of sufficient wave data in the past to significantly affect the wave field
analysis. Here ocean satellites will, of course, radically change the situation. But wave
modellers have also not viewed data assimilation with the same urgency as atmo-
spheric modellers, since wave forecasting, as opposed to weather forecasting, is not
essentially an initial value problem, but a boundary value problem. the wave field is
forced by the given wind field, and the initial wave field at some far past time when
the model was first spun up is irrelevant. Wave data is used not to initialize the wave
field, but simply as a running correction or update of the model simulation. In fact, it
could be argued that the main interest in wave data assimilation is not so much in the
improvement of the wave forecast but in the opportunity it provides for improving the
wind field analysis. For the wave field is a highly sensitive indicator of the quality of
the wind field, as demonstrated in Sections 2 and 3.

The difference in the nature of wave data assimilation compared with standard
meteorological data assimilation techniques carries a number of implications (cf
Hasselmann, 1985):

116

(i) The continuous assimilation of wave data during the running of the model creates no 'dynamical shock' problems. The local update information simply propagates into the forecast in the same way as a change in the external wind forcing.

(ii) If the modified wave field consists primarily of swell (as in most regions of the ocean, cf. Section 2), the updated swell will continue to propagate at its corrected value throughout the rest of the forecast: the correction 'sticks' However, if the wave field represents a windsea, and the (incorrect) wind field responsible for the wave field error is not modified simultaneously with the wave spectrum, the updated wave field will rapidly relax back to its original incorrect state in response to the uncorrected wind field.

(iii) Wave data is typically incomplete. The model requires the field of two-dimensional wave spectra, which are estimated today at only relatively few locations with directional buoys. ERS-1 will provide data on a global scale, but only in the form of the altimeter significant wave heights and azimuthally clipped, nonlinearly distorted and 180° ambiguous two-dimensional SAR image spectra. The assimilation procedure must therefore address the problem of translating this incomplete information into optimal spectral updates.

(iv) The region of influence of a measurement at a given point cannot be taken as approximately constant, as in the atmospheric case, but depends strongly on the type of spectrum and the spectral component. Swell which was generated in a far distant source may be associated with a region of influence of several thousand kilometers, while windsea generated by a local intense storm will have a much smaller characteristic correlation scale of the dimension of the wind field We show in the following that the proper treatment of this problem automatically follows from a consistent coupled wind and wave data assimilation approach.

## 6.2  Optimal wave data assimilation

The general task of wave data assimilation is to optimally modify the total wave field $F(f, \theta; \mathbf{x}, t)$ predicted by the model up to the time $t$ for all points $\mathbf{x}$ on the global ocean (or some selected area, in the case of regional applications) on the basis of a finite set of measurements $d_i = \phi_i(F)$, $i = 1, \ldots, n$.

The data $d$, can represent single numbers (e.g. $H_s$) or a full SAR spectrum, for example. It will be assumed that the wave data are assimilated continuously, so that we assimilate only wave data given at the time $t$.

'Optimal' implies here that the modified wave field should be consistent both with the data $d$, and the dynamical constraints of the wave model. In addition, the wave field is normally required to satisfy some additional 'æsthetic' quality or plausibility criterion, such as smoothness or minimal least square deviation from the predicted wave field. The dynamical model constraint implies that a consistent modification of the wave field can be achieved only if the wind field (at some earlier period) is also modified. The quality criterion will therefore be extended to include the requirement that the modification of the wind field should also be kept as small as possible.

### 6.2.1 General formalism

Satellites and conventional wave instruments yield various types of wave data $d_i(\mathbf{x}_p, t_p)$ at a given set of measurement positions $\mathbf{x}_p$ and times $t_p$ which are related to the two-dimensional wave spectrum $F(\mathbf{x}_p, t_p)$ through functions

$$\widehat{d}_i = D_i(F) \tag{6.1}$$

The goal of wave data assimilation is to modify the wave spectrum $F(\mathbf{x}_p, t_p)$ predicted by the model in such a manner that the wave data error function

$$\varepsilon_u = \sum_{i,j} (\widehat{d}_i - d_i) M_{ij} (\widehat{d}_j - d_j) \tag{6.2}$$

defined with respect to some suitably chosen (normally diagonal) positive definite matrix $M_{ij}$, is minimized, while maintaining the internal dynamical consistency of the overall wave field.

The latter condition requires that the wave spectrum modifications $\Delta\widehat{F}$ should be induced through modifications $\Delta u$, in the driving surface stress field,

$$\Delta\widehat{F}(\mathbf{x}_p, t_p) = \int_{-\infty}^{t_p} dt' \int d\mathbf{x}' \, G(\mathbf{x}_p, t_p; \mathbf{x}', t') \, \Delta u(\mathbf{x}', t') \tag{6.3}$$

or $\Delta\widehat{F} = G(\Delta\mathbf{u})$

Here $G(\mathbf{x}_p, t_p; \mathbf{x}', t')$ represents the (Green function) response of the wave field to small perturbations of the surface stress field. It is assumed in (6.3) that the wave field perturbations are small, so that the relation between $\Delta F$ and $\Delta u$, can be linearized.

In general, the modified stress field will not be uniquely determined by the condition $\varepsilon_{u} = minimum$. We therefore add an additional constraint: we seek a modification of the wind stress field which minimizes $\varepsilon_{u}$, while at the same time keeping the changes in $\mathbf{u}$, as small as possible. This can be achieved by minimizing the net error function (taking now for simplicity diagonal weighting functions $w_t$ and $w_u$)

$$\varepsilon = \sum_{i,p} w_i \left( (\Delta \widehat{d}_i + \widehat{d}_i - d_i) \right)^2_{\mathbf{x}_p, t_p} + \int dt' \int d\mathbf{x}' \left( \Delta \mathbf{u}_*(\mathbf{x}', t') \right)^2 \cdot w_u(\mathbf{x}', t') \tag{6.4}$$

with respect to $\Delta \mathbf{u}_*$, where $\Delta \widehat{d}_i = D_i(G(\Delta \mathbf{u}_*))$.

The minimization of $\varepsilon$ is to be carried out continuously as a function of $t$, equation (6.4) containing at any time $t$ all measurement points $t_p$ with $t_p \leq t$. In practice, the minimization of $\varepsilon$ at a given time $t$ will be able to benefit from the previous minimization at time $t - \Delta t$, where $\Delta t$ is the time increment for the insertion of new data (in the simpler example considered in the following sub-section, $\Delta t$ is the 20 minute propagation time step of the global wave model)

The full problem of minimizing $\varepsilon$ as given by equ. (6.4) is clearly a formidable task. First, the Green function $G$ has to be determined. This can be avoided by applying the adjoint technique, which is based on iterative integrations of the wave transport equation and its adjoint equation (cf. Thacker and Long, 1988) Secondly, $\varepsilon$ has to be minimized by some iteration procedure with respect to the field $\mathbf{u}$, $(\mathbf{x}, t$ depending on two space and one time dimension. For a system with a large number of degrees of freedom, this will normally require many iterations Since the integration of the adjoint wave transport equation alone requires a computational effort comparable to the integration of the wave model itself, the adjoint technique does not appear very promising without introducing additional simplifications. We shall follow instead the direct approach of inverting the wave transport equation and develop a very simple approximation for $G$

## 6.2.2 Approximate treatment of the Green function $G$

The relation between a perturbation $\delta u_*$ of the surface stress field and the resulting perturbation induced in the wave spectrum is obtained by perturbing the basic wave model transport equation (cf. WAMDIG, 1988)

$$\left( \frac{\partial}{\partial t} + \mathbf{v}\nabla \right)F = S_{in} + S_{nl} + S_{ds} = S \tag{6.5}$$

where $\mathbf{v}$ denotes the group velocity and $S_{in}$. $S_{nl}$. $S_{ds}$ represent the input, nonlinear transfer and dissipation source function, respectively. (For simplicity, we here used cartesian rather than the spherical coordinates of the global WAM model.)

One obtains

$$\left( \frac{\partial}{\partial t} + \mathbf{v}\nabla \right)\delta F = \Lambda\delta F + F \frac{\partial\beta}{\partial u_*} \delta u_* \tag{6.6}$$

where the linear operator $\Lambda$ represents the functional derivative of the nonlinear source function $S_{rest} = S_{tot} \cdot S_{in}$, excluding the wind input term

$$\Lambda = \frac{\partial}{\partial F} S_{rest})$$

and the second term on the right-hand side represents the derivative of the linear input source function $S_{in} = \beta F$ with respect to $u_*$.

The operator $\Lambda$ has been discussed in WAMDIG (1988), since it arises in the implicit source function integration scheme used in the WAM model. Because of the nonlinearity of the source functions $S_{nl}$ and $S_{ds}$, it is in general non-diagonal. This implies that a $\delta$-function perturbation $\delta u_*$ introduced at a given grid point and time generates not only wave spectrum perturbations propagating away from the disturbance point with their appropriate group velocities (as described by the diagonal propagation operator on the left-hand side of equ. (6.6)), but also a secondary perturbation field produced by scattering from the primary rays into a continuum of non-focussed secondary rays.

This greatly complicates the computation of the Green function. The same scattering process arises and is properly computed, of course, in the integration of

the fully nonlinear wave model. However, to avoid having to carry out a similar computation to determine the Green function, the matrix operator $\Lambda$ may be simplified by retaining only the diagonal part $\lambda$. The same approximation was used in the implicit integration scheme of the WAM model and was shown to be quite satisfactory for that application. In this case, equ. (6.6) can be immediately integrated to yield the Green function

$$\Delta F = G(\Delta u_*) = \int_{-o}^{t} dt' \left\{ F\left( \frac{\partial \beta}{\partial u_*} \right) \Delta u_* \right\}_{x',t'} exp \left[ \int_{t'}^{t} dt'' \, \lambda(x'',t'') \right] \tag{6.7}$$

where the integrations with respect to $t'$ and $t''$ represent path integrations along the individual wave group propagation paths

$$\mathbf{x'} = \mathbf{x} + \mathbf{v} \cdot (t' - t) \tag{6.8}$$

$$\mathbf{x''} = \mathbf{x'} + \mathbf{v} \cdot (t'' - t')$$

terminating in $\mathbf{x}$ and $\mathbf{x'}$, respectively.

An inspection of (6.7) reveals that for any given spectral component $G$ has a pronounced maximum at a position along the ray corresponding to the last point at which the wave component received a significant input from the wind, i.e. in the transition region from windsea to swell. For earlier times, the impact of a variation $\delta u_*$ is lost through the interaction with the rest of the spectrum, expressed by the large (windsea) value for $\lambda$. In the swell region, after the windsea has been transformed into a swell component, the exponential damping vanishes, but the wind input factor $\partial \beta / \partial u_*$ itself also vanishes. The most effective region for modifying a spectral component is therefore essentially identical to the 'region of origin' of the wave component as defined heuristically through the 'wave age' $\tau$ (cf. Booij and Holthuijsen, 1987).

To a resonable first approximation the Green function may therefore be represented as a $\delta$-function:

$$G(\mathbf{x}, t; \mathbf{x'}, t') = \delta(\mathbf{x'} - \mathbf{x} + \mathbf{v}\tau)\delta(t' - t - \tau)A \tag{6.9}$$

where $A = A(\mathbf{k}, \mathbf{x}, t)$ is a weighting factor determined by the speed of transition from windsea to swell.

The relatively simple structure of the approximate Green function and the reduction of its effective 'region of dependence' to a geometrically well defined, limited region governed by the wave age suggests further simplifications in the next step of determining the $\Delta u$. field which minimizes $\varepsilon$.

### 6.2.3 Implementation

We have established linear relationships between the three sets of data consisting of the perturbations of the wind stress field $\delta u$. $\equiv (\mu_a)$, perturbations of the wave spectra $\delta F \equiv (\phi_a)$ and perturbations $\delta(\widehat{d_i} - d_i) \equiv (D_v)$ of the deviations between predicted and observed wave data:

$$\phi_a = \sum_a M^{(1)}_{aa} \mu_a \tag{6.10}$$

$$D_v = \sum_a M^{(2)}_{va} \phi_a \tag{6.11}$$

where $M_{aa}^{(1)}$ represents the Green function (equ. 6.9) and $M_{va}^{(2)}$ represents the derivative of the predicted data $\widehat{d_i}$ with respect to the predicted spectrum $F$. The indices of the vectors $\phi_a$, $D_v$ and $\mu_a$ run through the entire data set involved in a given data assimilation cycle, including the spatial and temporal dependence and the individual components of the fields (e.g. the set of spectral components in the case of wave or SAR image spectra, or the two vector components in the case of the wind stress vector)

In terms of the present notation, the variational problem (6.4) we wish to solve takes the form

$$\varepsilon = \sum_v w_v |D_v - D^o_v|^2 + w_o \sum_a \mu_a^2 = min \tag{6.12}$$

where

$$D^o_v = \widehat{d}_v - d_v \tag{6.13}$$

represents the deviation between the predicted and observed wave data for the unperturbed wave spectra (prior to data assimilation) and $w_o$, $w_v$ are weighting factors

Substituting the linear relations (6.10), (6.11) into (6.12) we obtain

$$\varepsilon = \sum_{v} w_v \left( D_v^0 - \sum_{\alpha} M_{v\alpha}^{(3)} \mu_\alpha \right)^2 + w_0 \sum_{\alpha} \mu_\alpha^2 = min \qquad (6.14)$$

$$M_{v\alpha}^{(3)} = \sum_{\alpha} M_{v\alpha}^{(2)} M_{\alpha\alpha}^{(1)} \qquad (6.15)$$

The minimum of (6.12) is given by the solution of the linear system of equations

$$\sum_{\beta} M_{\alpha\beta}^{(4)} \mu_\beta = C_\alpha \qquad (6.16)$$

where

$$M_{\alpha\beta}^{(4)} = \sum_{v} w_v M_{v\alpha}^{(3)} M_{v\beta}^{(3)} + w_0 \delta_{\alpha\beta} \qquad (6.17)$$

and

$$C_\alpha = \sum_{v} w_v D_v^0 M_{v\alpha}^{(3)}$$

In practice, the minimum of $\varepsilon$ may be obtained more rapidly by applying direct minimization methods (e.g. conjugate gradient techniques, cf. Navon and Legler, 1987) to the relatively simple quadratic form (6.12) rather than solving the system (6.14).

The solution of the minimization problem yields the entire wind stress correction field $\delta u_*$, but the corrected wave field only at points where measurements exist. (The matrix multiplication (6.15) runs over only those indices for which $M_{v\alpha}^{(2)} \neq 0$, i.e. only those spectral values which impact the data values $\hat{d}_i$.) To update the entire correction field for the wave spectrum the Green function relation (6.10) must be applied for the wave spectra at all grid points.

We note that the approach outlined here avoids the need for an explicit inversion of the wave spectrum → SAR spectrum transformation relation. The inversion for SAR wave data is considered automatically within the framework of the complete inversion problem. We note furthermore that the derivative matrix $M_{v\alpha}^{(2)}$ for SAR image spectral data was derived in Section 5 in the course of the

derivation of the general nonlinear spectral transformation relation for SAR image spectra.

Since effective numerical procedures have been developed for minimizing quadratic forms of the type (6.14) for systems with several thousand degrees of freedom (cf. Navon and Legler, 1986), it appears feasible to implement the approach outlined here in operational framework.

## 7. An example of altimeter wave data assimilation for August, 1978

As a first step towards the development of a complete wind and wave data assimilation system we have investigated the simpler decoupled problem of assimilating wave data into the wave model without modifying the wind field. This differs from the approach of Thomas (1988) and Janssen et al. (1988), who modify both the wind and wave field. As outlined above, our ultimate goal is to modify only the wind field directly, the wave field changes being tied to the wind field modifications through the wave model. The present decoupled study was carried out as a reference to establish the direct impact of the wave data on to the wave model. It may also be interpreted as an implicit wind field modification exercise in which only the past wind field (which has no influence on the current wave field development) is altered. The study provides insight into the characteristic region of influence of wave measurements, and the typical relaxation time of new information inserted into the model. The assimilated data were the global SEASAT altimeter wave height data obtained during the month of August, 1978. This month was chosen as it contained relatively few data gaps.

The data were inserted into the wave model at each propagation time step, i e every forty minutes. This corresponds to an orbit segment of about 17,000 km, or up to 85 data points separated by 200 km. For each wave height data point the model wave spectrum was modified over a finite set of surrounding model grid points. Experiments were carried out with different scales $L$ for the region of influence

Within a region of influence, an updated wave spectrum $F_{new}(f, \theta)$ was formed by applying a correction factor $c$ to the predicted spectrum $F_{pred}(f, \theta)$,

$$F_{new}(f, \theta) = c F_{pred}(f, \theta) \tag{7 1}$$

where

$$c = \begin{cases} \left(1 + \left(1 - c_{max}\right) \cdot \left(\frac{1}{2} \cdot \left[\frac{|\Delta\phi|^2}{L_\phi^2} - \frac{|\Delta\lambda|^2}{L_\lambda^2}\right]\right)^{3/2}\right) & \text{for } |\Delta\phi| < L_\phi, \ |\Delta\lambda| < L_\lambda \\ \\ 1 & \text{for } |\Delta\phi| > L_\phi \quad \text{or} \quad |\Delta\lambda| > L_\lambda \end{cases}$$

and

125

$$c_{max} = H_s^{alt} / H_s^{mod} \qquad (7.3)$$

Here $H_s^{alt}$, $H_s^{mod}$ denote the altimeter wave height and the interpolated model wave height at the measurement point, respectively, and $\Delta\phi$, $\Delta\lambda$ represent the distances in degrees latitude and longitude respectively, of the model grid point from the measurement point (cf. Fig. 7.1) Close to the measurement point, $c \approx c_{max}$, and the model spectrum is adjusted to reproduce the observed wave height. The correction factor relaxes bi-linearly to unity at the edge of the rectangular region of influence.

Assimilation experiments were carried out with $L_\phi$, $L_\lambda$ = 9, 9 and 15, 15 degrees, corresponding to 3 × 3 and 5 × 5 grid points in a region of influence. The best results, shown in Figs 7.2 - 7.5, were obtained for the case $L$ = 15. This scale is compatible with the time-space sampling density of the satellite and ensures that essentially all points on the model grid have received significant impact from the altimeter wave height measurements within a 3 day sampling period.

To remove spin-up effects from the August analysis period, the assimilation run was started on July 28, the assimilation run itself being restarted from the run without assimilation beginning July 7, 1978. The GLA surface stress field was used as input.

Figs 7. 2 a - c show the mean wave heights for August, obtained with the assimilation run. A comparison with Figs 2 2 b - 2 4 b and 2.5 b showing the previous results for the run without data assimilation and the significant wave heights derived from the SEASAT altimeter demonstrates the significant improvement achieved through data assimilation.

The relaxation time of the assimilation procedure was tested in a further experiment in which the assimilation process was switched off in the middle of the (3-point) assimilation run, on August 15. The characteristic relaxation time for the global model bias error (the global mean deviation of the model and altimeter wave height) is of the order of 6 days (Fig. 7 3b). In this period the error has grown back to the same magnitude as in the original hindcast without data assimilation.

We note that the characteristic relaxation times found for the present assimilation switch-off experiment are generally larger than those found by Janssen et al. (1988) in a similar switch-off experiment. This is due to the larger region of influence chosen in the present assimilation scheme. If the region of influence is smaller than the orbit spacing corresponding to the satellite repeat period (or characteristic time scale of weather patterns, in the case of windsea) only part of the model grid is updated during the

assimilation procedure. The propagation of the non-corrected wave field from the missed regions into the neighbouring, corrected wave field regions then degrades the update in the corrected regions on the relatively short time scale of the wave propagation time from non-updated to updated regions.
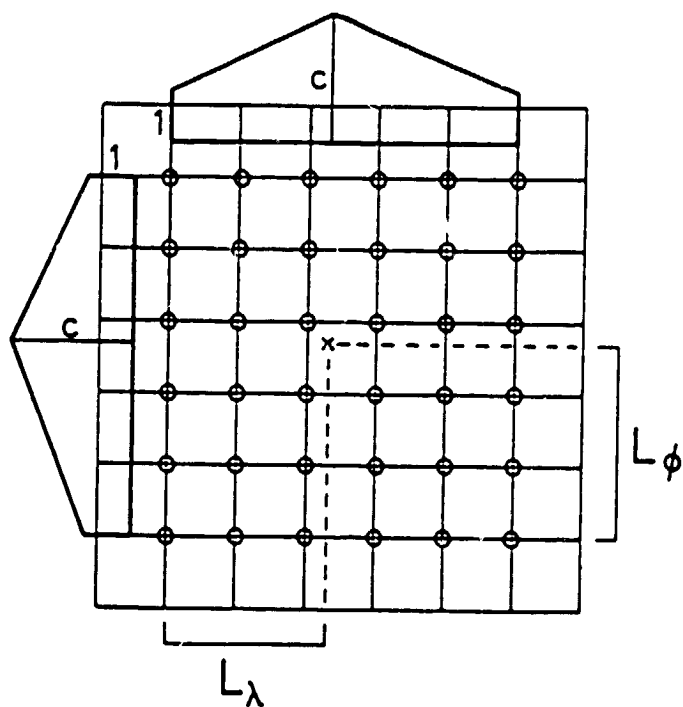
Fig. 7.1 Region of influence and correction factor c used in altimeter wave height assimilation experiments.
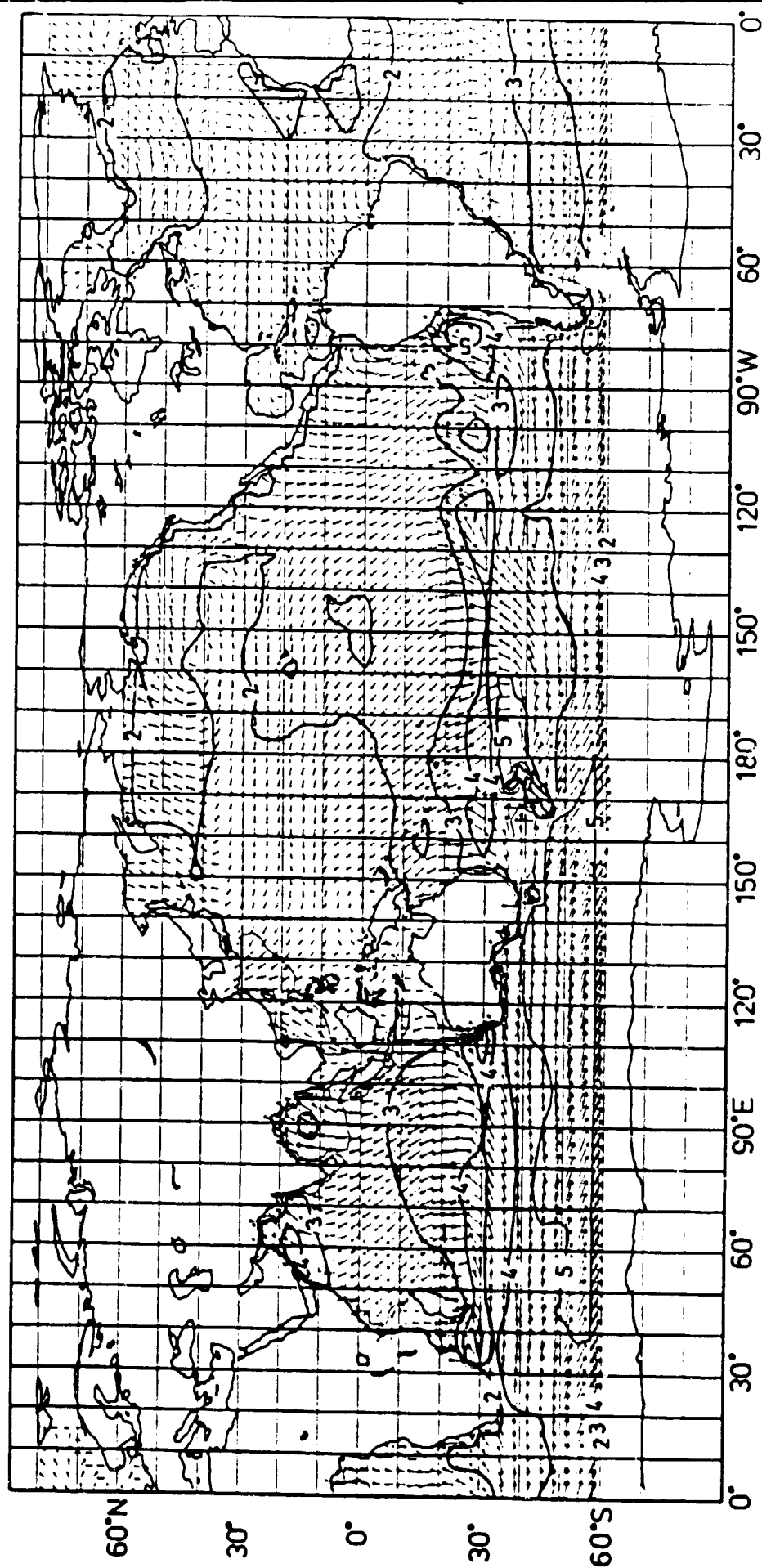
Fig 7.2 a    Mean significant wave heights for model hindcast with assimilated altimeter
wave heights for August, 1978. total wave field

129
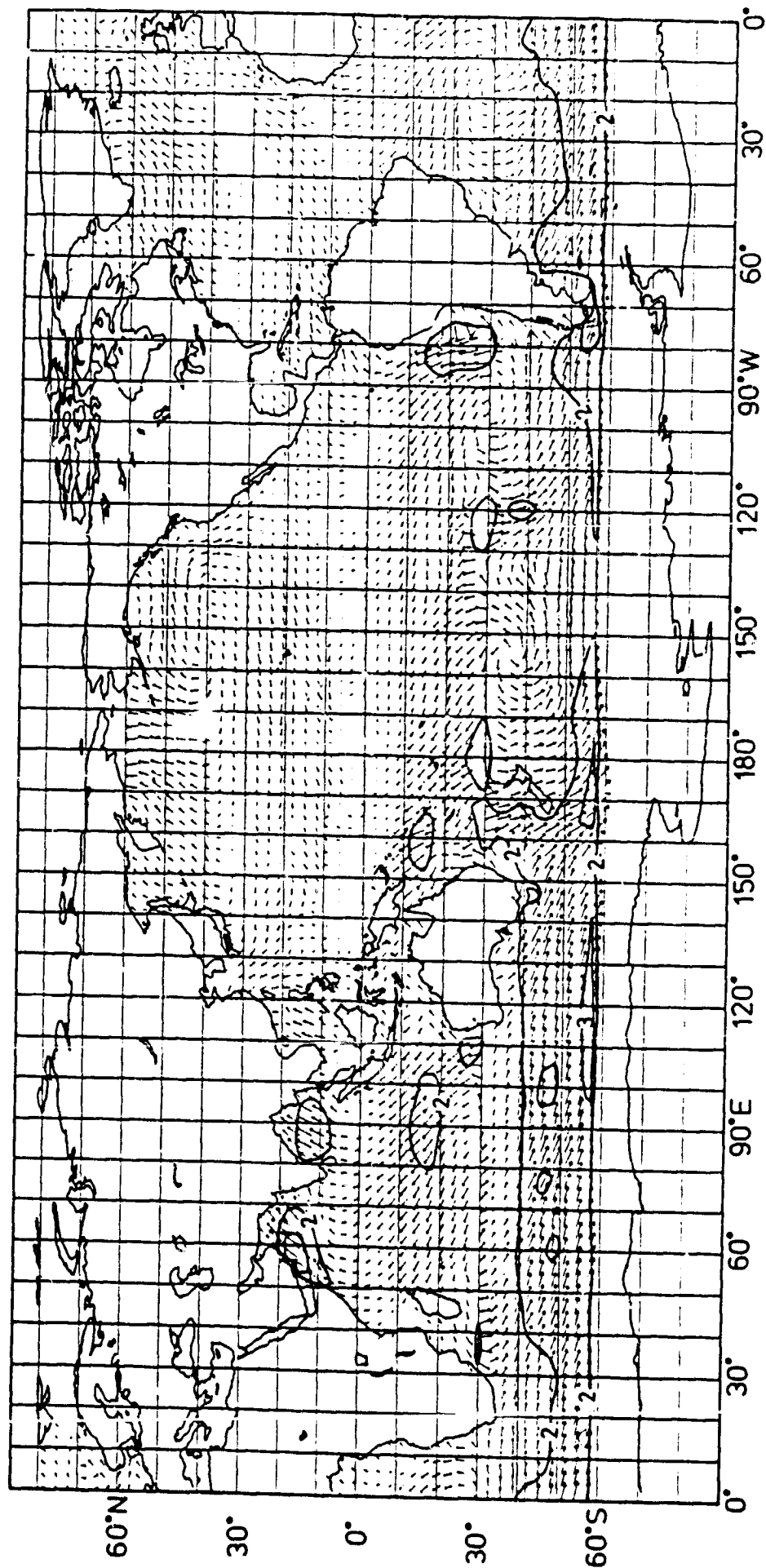
Fig 7.2.b    Mean significant wave heights for model hindcast with assimilated altimeter
            wave heights for August, 1978 windses
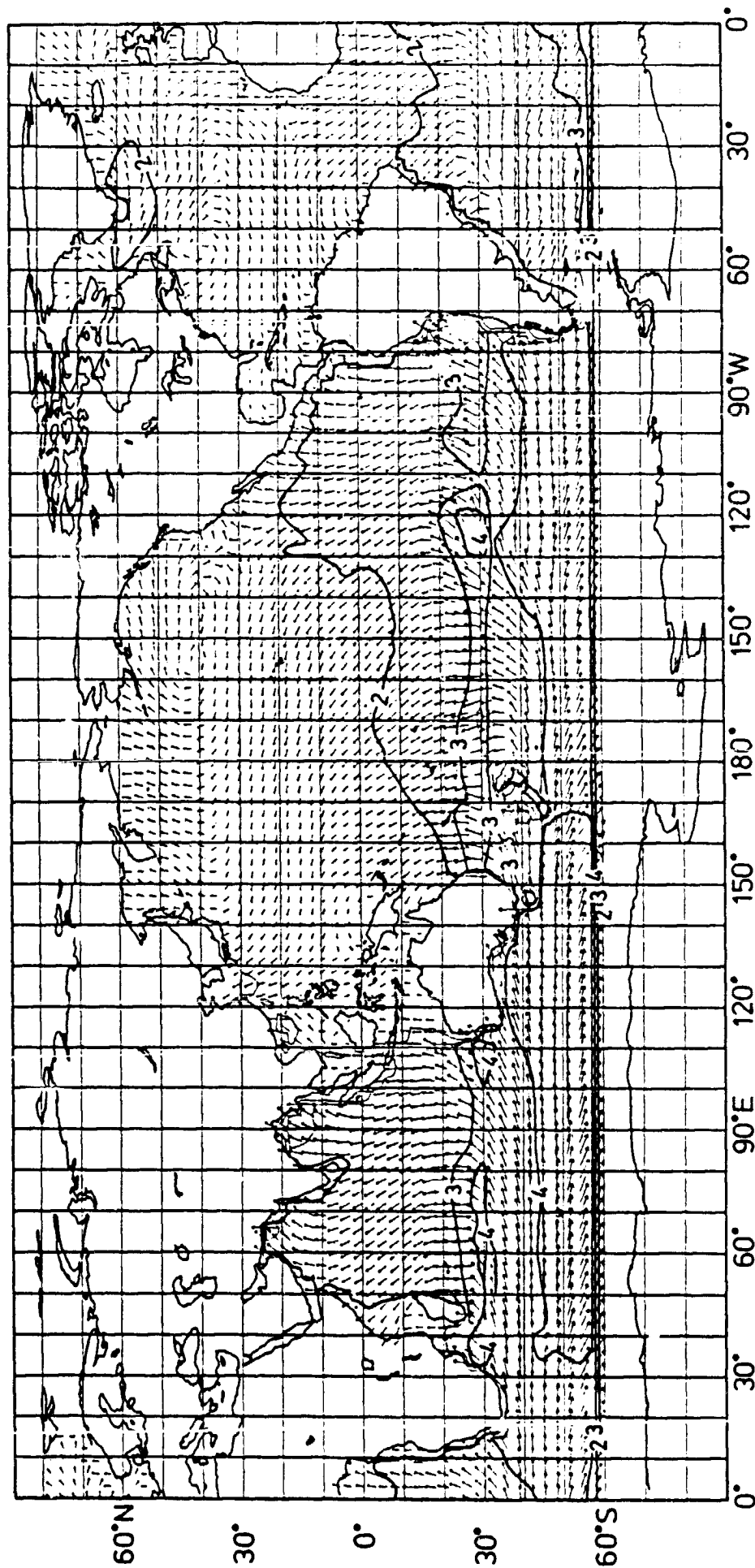
Fig 7 2c       Mean significant wave heights for model hindcast with assimilated altimeter
wave heights for August, 1978: swell
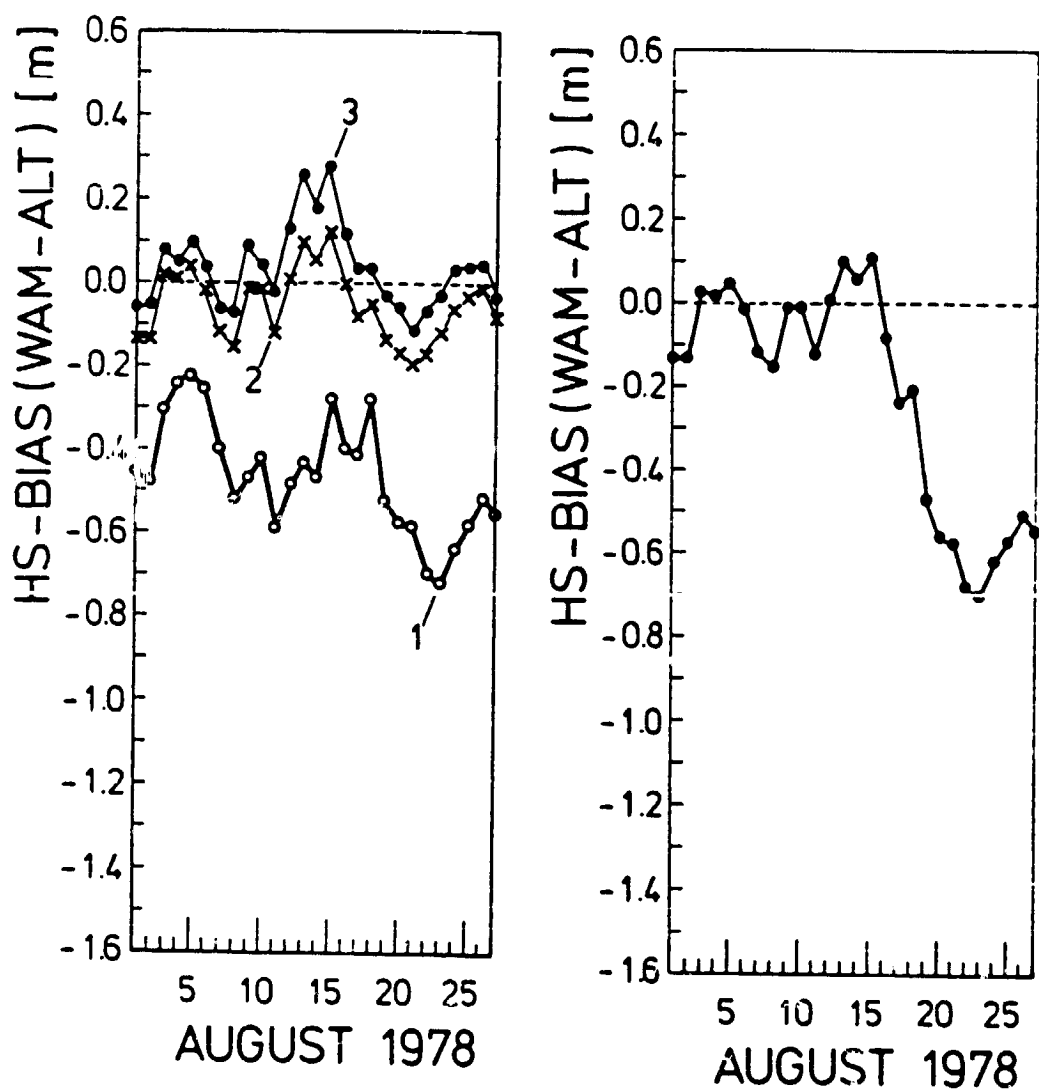
Time histories of global daily mean bias deviations of model and altimeter wave height fields for: original hindcast (curve (1)) and two assimilation runs with different regions of influence scales $L = 9°$ (curve (2)), and $L = 15°$ (curve (3)) (panel (a)), assimilation switched off for $L = 9°$ on August 15 (panel (b)).

8. Conclusions

Our investigations of SEASAT altimeter and SAR wave data using a global wave model driven by wind fields derived from assimilated scatterometer data have provided valuable insight into the quality and application of ocean satellite wind and wave data. This SEASAT exercise is particularly relevant for ERS-1, which will be carrying a similar suite of sensors We may summarize the principal conclusions of this study, which we regard as a first step towards the development and implementation of a comprehensive wind and wave data assimilation system for ERS-1, as follows:

1) Wave models represent an excellent data validation tool, providing a sensitive natural consistency check of wind and wave data. The shortcomings of the GLA 6 hourly averaged surface stress fields derived by data assimilation from scatterometer and conventional meteorological data were immediately revealed by comparing the hindcast wave heights with altimeter wave heights This technique is particular valuable in data sparse regions such as the Southern Ocean, when the altimeter wave height data may represent the only independent verification of the wind field analysis

2) A number of further data validation tests and wave hindcast intercomparisons with other wind field products suggested that these shortcomings were not directly related to the wind field data assimilation method as such, but resulted from the time averaging involved in producing the stress fields But it is also possible that inconsistencies in the scatterometer algorithm (Woiceshyn et al , 1987. Anderson et al , 1987) contributed to the discrepancies. A combination of the data validation procedures described in Anderson et al (1987), Janssen et al (1988) with those in the present report would provide a valuable operational system for real time monitoring of the performance of the wind and wave sensors of ERS-1

3) The direct assimilation of altimeter wave height data in wave models has a significant positive impact on the skill of the wave forecast. This applies particularly for the swell field The average relaxation time of the wave update information is of the order of six days

4) For windseas, wave data assimilation has little impact on the quality of the longer term wave forecast unless the wind field is modified together with the wave field By improving the wind field, this requirement also increases the skill of the weather forecast and provides improved air-sea flux fields required for climate research

133

5)  The development of a fully interactive wind and wave data assimilation system represents a formidable task, since wave field errors imply errors in the wind field not only at the same time level, but also at early levels which can extend back one or two weeks. A general variational approach for constructing simultaneously optimized wind and wave fields was developed. The models and numerical techniques for implementing such a system are now largely available, and it is recommended that work in this area is pursued with high priority in order to provide a viable operational system in time for the launch of ERS-1. The modifications of the wind field induced by wave data in such a system would represent a quantitative, constructive version of the wind and wave data mutual consistency tests summarized in 1) above.

6)  SAR wave image spectra normally represent strongly nonlinearly distorted transformations of the wave spectra. This applies for both windsea and swell spectra. SAR image spectra cannot be usefully interpreted unless supported by computations of the nonlinear transformation from the wave spectrum to the SAR spectrum. This implies, in practice, that SAR wave spectra can be used operationally only in conjunction with a realistic (third generation) wave model which can provide a good first guess wave spectrum. This will be available only in an operational forecasting environment, i.e. in weather forecasting centres.

7)  Monte Carlo computations of the nonlinear transformation of the wave spectrum into the SAR image spectrum, using the hindcast wave model spectrum as input, were in excellent agreement with the SEASAT SAR spectra for a set of 32 different scenes. This indicates that the long debated theory of the SAR imaging of a moving ocean wave surface is now well understood and can be used confidently.

8)  A new closed expression relating the SAR image spectrum to the surface wave spectrum was derived. This opens the possibility of computing the nonlinear spectral transformation directly, without reverting to the pixel-to-pixel mapping of individual scene realizations using Monte Carlo simulation techniques. The Monte Carlo technique suffers from statistical sampling errors and is relatively costly in computer time (~ 1 minute CRAY X-MP per spectrum). It cannot be used for the routine processing of the many SAR image spectra generated globally by the ERS-1 SAR in the wave mode. Computations of the nonlinear spectral transformation using the newly derived relation were not foreseen and could not be included within the framework of this study contract, but should be carried out with high priority in a follow-up study to determine whether this approach has operational potential for ERS-1

9)    Methods need to be developed for inverting the transformation wave spectrum → SAR
      spectrum. This question should be approached within the general context of imple-
      menting a joint wind and wave data assimilation system as summarized under 5)
      above. The goal of such an interactive assimilation system is to modify only the wind
      field directly, the wind field modifications being chosen such that both the wind field
      and the resultant wave field are optimized with respect to the wind and wave
      observations. In this context a SAR image spectrum can be treated in the same manner
      as any other derived wave information, such as altimeter wave heights or one-
      dimensional wave spectra. It follows that the inversion of the transformation wave
      spectrum → SAR image spectrum need not be carried out explicitly, the general
      inversion procedure being based on iterative corrections including only forward
      transformations.

      In summary, we have found encouraging results with respect to the potential of wave
models for the routine validation of wind and wave data and the assimilation of altimeter
wave data. Most of these could be readily implemented in an operational system. However,
we have also identified (and in some cases made some progress in theoretically resolving) a
number of fundamental issues with respect to the simultaneous, interactive assimilation of
wind and wave data and the application of SAR wave image data. These questions will need
to be addressed with high priority within the next two years if ERS-1 is to realize the high
expectation placed by the scientific community in this satellite

# References

Alpers, W., and C.L. Rufenach (1979): The effect of orbital motions on synthetic aperture radar imagery of ocean waves. IEEE Trans. Antennas Propag. AP-27, 685-690.

Alpers, W., D.B. Ross, and C.L. Rufenach (1981): On the detectability of ocean surface waves by real and synthetic aperture radar. J.Geophys. Res. **86**, 6481-6498.

Alpers, W., and C. Brüning (1986): On the nonlinearity of synthetic aperture radar response to moving ocean surface waves. IEEE Trans. Geosci. Remote Sensing, Vol. GE-24, No 6, 873-885

Alpers, W., C. Brüning, and K. Richter (1986): Comparison of simulated and measured Synthetic Aperture Radar Image spectra with buoy-derived ocean wave spectra during the Shuttle Imaging Radar B Mission. IEEE Trans.Geosci. Remote Sensing, Vol. GE-24, No. 4, 559-566.

Anderson, D., A. Hollingsworth, S. Uppala, and P. Woiceshyn (1987): A study of the feasibility of using sea and wind information from the ERS-1 satellite. Part 1: Wind Scatterometer Data, ECMWF Contract Report to ESA.

Atlas, R., A.J. Busalachi, M. Ghil, S. Bloom, and E. Kalnay (1987): Global surfacewind and flux fields from model assimilation of SEASAT data. J Geophys Res **92**, 6477-6487.

Bass, F.G., I.M. Fuks, A.I. Kalinykov, I.E. Ostreowsky, and A.D. Rosenberg (1968): Very high frequency radio wave scattering by a disturbed sea surface. IEEE Trans. Antennas Propag., AP-16, 554-568.

Beale, R.C. (1983): Large and small scale spatial evolution of digitally processed ocean wave spectra from SEASAT Synthetic Aperture Radar. J.Geophys. Res **88**, 1761-1778

Booij, N., and L.H. Holthuijsen (1987): Propagation of ocean waves in discrete spectral wave models. J.Comp.Phys. **68**, No. 2.

Brüning, C. (1987): Untersuchung der Abbildung von Ozeanoberflachenwellen durch ein Synthetic Aperture Radar. Hamburger Geophysikalische Einzelschriften No. 84.

Bruning, C., W. Alpers, and K. Hasselmann (1988): On the nonlinearity of synthetic aperture radar imaging of ocean surface waves studied by two-dimensional Monte Carlo simulation techniques. (submitted to Int. J. Remote Sensing).

Charnock, H. (1955): Wind stress on a water surface. Q.J.R. Meteorol. Soc., 81, 639-640.

Fedor, L.S., and D.E. Barrick (1978): Measurement of ocean wave heights with a satellite radar altimeter. EOS Trans AGU, 59, 84.

Fedor, L.S., T.W. Godbey, J.F.R. Gower, R. Guptill, G.S. Hayne, C.L. Rufenach, and E.J. Walsh (1979): Satellite altimeter measurements of sea state - An algorithm comparison. J. Geophys. Res. 84, 3991-4002.

Fedor, L.S., and G.S. Brown (1982): Wave height and wind speed measurements from the SEASAT radar altimeter. J Geophys. Res. 87, 3254-3260.

Hasselmann, K. (1974): On the spectral dissipation of ocean waves due to white capping. Boundary-Layer Met. 6, 107-127.

Hasselmann, K. (1985): Assimilation of microwave data in atmospheric and wave models in the use of satellite data in climate models. Proc Conf Alpbach, 47-52 (ESA-244)

Hasselmann, K., and J I Collins (1968): Spectral dissipation of finite-depth gravity waves due to turbulent bottom friction. J Marine Res. 26, 1-12.

Hasselmann, K., R.K. Raney, W.J. Plant, W Alpers, R.A. Shuchman, D R. Lyzenga, C.L. Rufenach, and M.J. Tucker (1985): Theory of Synthetic Aperture Radar Ocean Imaging: A MARSEN View. J.Geophys Res. 90, 4659-4686.

Hasselmann, S. (1987): The WAM Wave Model System Rep Max-Planck-Institut fur Meteorologie, Hamburg

Hasselmann, S., and K. Hasselmann (1981) A symmetrical method of computing the nonlinear transfer in a gravity-wave spectrum Hamburger Geophys Einzeischriften, Reine A: Wiss. Abhand. 52, 138 pp

Hasselmann, S., and K. Hasselmann (1985): A global wave model. WAM Report, Max-Planck-Institut für Meteorologie.

Hasselmann, S., and K. Hasselmann (1985): Computations and parameterizations of the
    nonlinear energy transfer in a gravity wave spectrum (1985): Part 1: A new method for
    efficient computation of the exact nonlinear transfer integral. J.Phys. Oceanogr. **15**,
    1369-1377.

Hasselmann, S., K. Hasselmann, J.H. Allender, and T.P. Barnett (1985): Computations and
    parameterizations of the nonlinear energy transfer in a gravity-wave spectrum. Part 2:
    Parameterizations of the nonlinear energy transfer for application in wave models.
    J.Phys.Oceanogr. **15**, 1378-1391

Hayne, G.S. (1977): Initial development of a method of significant wave height estimation for
    GEOS-3. NASA Rep., NASA-2520.

Janssen, P., P. Lionello, M. Reistad, A. Hollingsworth, (1988): A study of the feasibility of using sea
    and wind information from the ERS-1 satellite. Part 2: Use of Scatterometer and
    Altimeter Data in Wave Modelling and Assimilation, ECMWF Contract Report to ESA

Komen, G.J. (1985): Introduction to wave models and assimilation of satellite data in wave model
    in the use of satellite data in climate models. Proc. Conf. Alpbach, 21-26 (ESA), 244 pp

Komen, G.J., S. Hasselmann, and K. Hasselmann (1984): On the existence of a fully developed
    windsea spectrum. J.Phys Oceanogr. **14**, 1271-1285

Lehner, S. (1984): The use of SAR for large scale wind measurements over the ocean. Hamburger
    Geophys. Einzelschr., Reihe A, No. 68.

Mognard, N.M., W.J. Campbell, R.E. Cheney, and J.G. Marsk (1983): Southern ocean mean
    monthly waves and surface winds for winter 1978 by SEASAT radar altimeter.
    J.Geophys.Res. **88**, 1736-1744

Navon, I.M., and D.M. Legler (1987): Conjugate-gradient methods from large-scale
    minimization in meteorology. Monthly Weather Review, 1479-1502

Phillips, O.M. (1977): Dynamics of the Upper Ocean. 2nd edition. Cambridge Univ. Press

Raney, R.K. (1981): Wave orbital velocity, fade and SAR response to azimuth waves. IEEE
    J. Oceanic Eng. OE-6, 4.

Snodgrass, F E , G.W. Groves, K.F. Hasselmann, G.R. Miller, W.H. Munk, and W.H. Powers (1966): Propagation of ocean swell across the Pacific. Philos.Trans.R.Soc. (A), 259, 431

The SWAMP Group (1985): Sea Wave Modelling Project (SWAMP), An intercomparison study of wind wave prediction models. Part 1: Principal results and conclusions. Ocean Wave Modeling, Plenum Press, New York, 256 pp.

Swift, C.F., and L.R. Wilson (1979): Synthetic aperture radar imaging of moving ocean waves. IEEE Trans.Antennas Propag. AP-27, 725-729

Thacker, W.C., and R.B Long (1988): Fitting dynamics to data (Submitted for publication)

Thomas, J. (1988): Retrieval of energy spectra from measured data for assimilation into a wave model. (To be published).

Valenzuela, G.R. (1980): An asymptotic formulation for ʳ     nages of the dynamical ocean surface. Radio Science 15, 105-114

The WAMDI-Group (1988): The WAM Model - a third generation ocean waveprediction model J.Phys.Oceanogr (in print)

Woiceshyn, P A., M.G Wurtele, D.H. Boggs, L.F McGoldrick, S Peteherych (1987) The necessity for a new parameterization of an empirical model for wind/ocean scatterometry J.Geophys.Res. 91, 2273-2288

Wright, J.W. (1968): A new model for sea clutter IEEE Trans Antennas Propag., AP-16, 217-223

Wu, J. (1982): Wind-stress coefficients over sea surface from breeze to hurricane J.Geophys Res., 87, N° C12, 9704-9706.

## Tables

# GLOBAL DATA ASSIMILATION PROGRAMME FOR AIR-SEA FLUXES

JSC / CCCO Working Group on Air-Sea Fluxes

## Summary

The JSC/CCCO Working Group on Air-Sea Fluxes was formed by the Joint Scientific Committee (JSC) of the World Climate Research Programme (WCRP) and the Committee on Climatic Changes and the Ocean (CCCO) to develop a programme for producing, on a continuous basis, global fields of air-sea fluxes ,making use, in particular, of the new data which will become available with the next generation of ocean satellites. These fields are an essential input for many climate studies, including the major WCRP/CCCO projects TOGA (Tropical Ocean/Global Atmosphere) and WOCE (World Ocean Circulation Experiment)

The goal of the proposed Global Data Assimilation Programme for Air-Sea Fluxes (GDAP) is to provide continuous, 6 hourly, 1° resolution, global fields of the air-sea fluxes of momentum, sensible and latent heat, water, and solar and infra-red radiation beginning 1991.

To achieve this goal, comprehensive data assimilation systems need to be implemented at operational global weather centres capable of processing the many different forms of input data which enter into to the flux field analysis. These include data from oceanographic and meteorological satellites, ships, buoys and the weather station network. It is proposed that at least one such data assimilation system be established in Europe (at the European Centre for Medium Range Weather Forecasts) and in the U.S (at the National Meteorological Center). Additional assimilation systems at other weather centres could usefully augment the programme.

The 1991 target date set for the operational implementation of the system at ECMWF and NMC corresponds to the estimated start of the operational phase of ERS-1, the first of a series of planned oceanographic satellites. Before the operational phase the system will be run in a research and validation mode, with no direct interaction with operational analyses and forecasts

A number of projects are defined to develop and implement the system within this time frame. These include:

- the incorporation of ocean satellite sensor algorithms within the assimilation system,
- the quasi real-time provision of calibrated physical sensor data from ocean satellites,
- the extension of existing data quality control systems to include the new kinds of data available from oceanographic satellites,
- the inclusion of surface wave data and global wave models in the sensor algorithms, data assimilation system and flux parameterisation, and
- the improvement of assimilation procedures for the insertion of two-dimensional surface data into three-dimensional fields

In addition to the near real-time data assimilation programme carried out within the framework of the routine forecasting operations, provision should be made through an effective archiving and retrieval system for a possible reanalysis of the entire input data set at a later time. Although costly, this could prove to be desirable after a few years operational experience in order to provide a temporally homogeneous flux data set based on the latest improved algorithms and assimilation systems

Proposals are also made for upgrading the in situ ocean data collection system. In situ data are important both as valuable input data and for calibration purposes. Organizational measures are suggested which could significantly enhance the quality and quantity of data from these sources.

## 1. Goals

The fluxes of momentum, heat, radiation and water at the air-sea interface drive the ocean circulation and determine the coupling between the atmosphere and the ocean. A reliable determination of these flux fields is therefore essential for understanding the role of the oceans in climate. The goal of the Global Data Assimilation Programme (GDAP) is to develop practical oceanographic satellite data retrieval and appropriate data assimilation schemes which could be applied routinely in producing optimal global air-sea flux data sets.

This activity has been formally constituted as part of the WMO/ICSU World Climate Research Programme (WCRP) by the Joint Scientific Committee (JSC) for the WCRP and the Committee on Climatic Changes and the Ocean (CCCO), under the guidance of the joint JSC/CCCO Working Group on Air-Sea Fluxes (WG-ASF members are listed in Appendix 1). This step was taken in view of the requirement in the WCRP, especially the WOCE and TOGA components (as described in Section 2.1) for continuous global gridded air-sea flux fields exploiting the entire range of available input data including, in particular, the new sources of ocean satellite data (e.g. scatterometer winds and altimetric information) that are expected to become available operationally in the next two or three years

Although ocean satellites can provide important data on fields at the sea surface as input for the flux computations, the derivation of valid geophysical data from the sensor signals of these satellites is not straightforward. Normally, auxilliary meteorological or oceanic data are needed. The satellite data therefore needs to be combined with conventional meteorological and sea surface data in a comprehensive data assimilation system. This combination should be performed within the physical constraints of an atmospheric general circulation model, and the expertise for this activity resides at the global weather centres.

In addition to ocean satellite data, an important data base for air-sea flux computations are conventional in situ ocean surface data, which provide a calibration reference for ocean satellites and meteorological analyses. The

GDAP therefore also includes recommentations for upgrading the conventional surface data set obtained from ships, buoys and other sources.

The principal goals of the GDAP may be thus summarized, in accordance with the terms of reference of the WG-ASF (cf. Appendix 2), as

1.  the development and implementation of comprehensive data assimilation systems for the operational computation of global air-sea flux fields at global weather centres and

2.  the upgrading of the in situ air-sea flux data collection system.

## 1.1  Data assimilation

The data required for computing global air-sea flux fields originates from a variety of sources (satellites, ships, buoys, weather stations) with widely differing characteristics regarding coverage, sampling density, accuracy and type of variable measured. The reconstruction from these data of optimally estimated flux fields which are dynamically consistent with the overall atmospheric circulation requires the application of a sophisticated data assimilation system based on a high resolution global atmospheric model. In view of the known impact of sea state on the microwave sensor signals of oceanographic satellites, and also on the air-sea transfer processes themselves, it is furthermore desirable to incorporate wave data and a global wave model within the assimilation system.

The data assimilation requirements for climate research and operational weather and wave forecasting are essential identical. It therefore appears logical to develop a single comprehensive data assimilation system for both applications. Fig. 1 (from Hasselmann, 1985) shows an outline of the proposed structure of such a data assimilation system in relation to the ocean satellite receiving stations and off-line data processing and archiving facilities. The plan foresees two main extensions of existing operational data assimilation systems: the incorporation of the sensor algorithms within the data assimilation system and the inclusion of a global wave model (GWM).
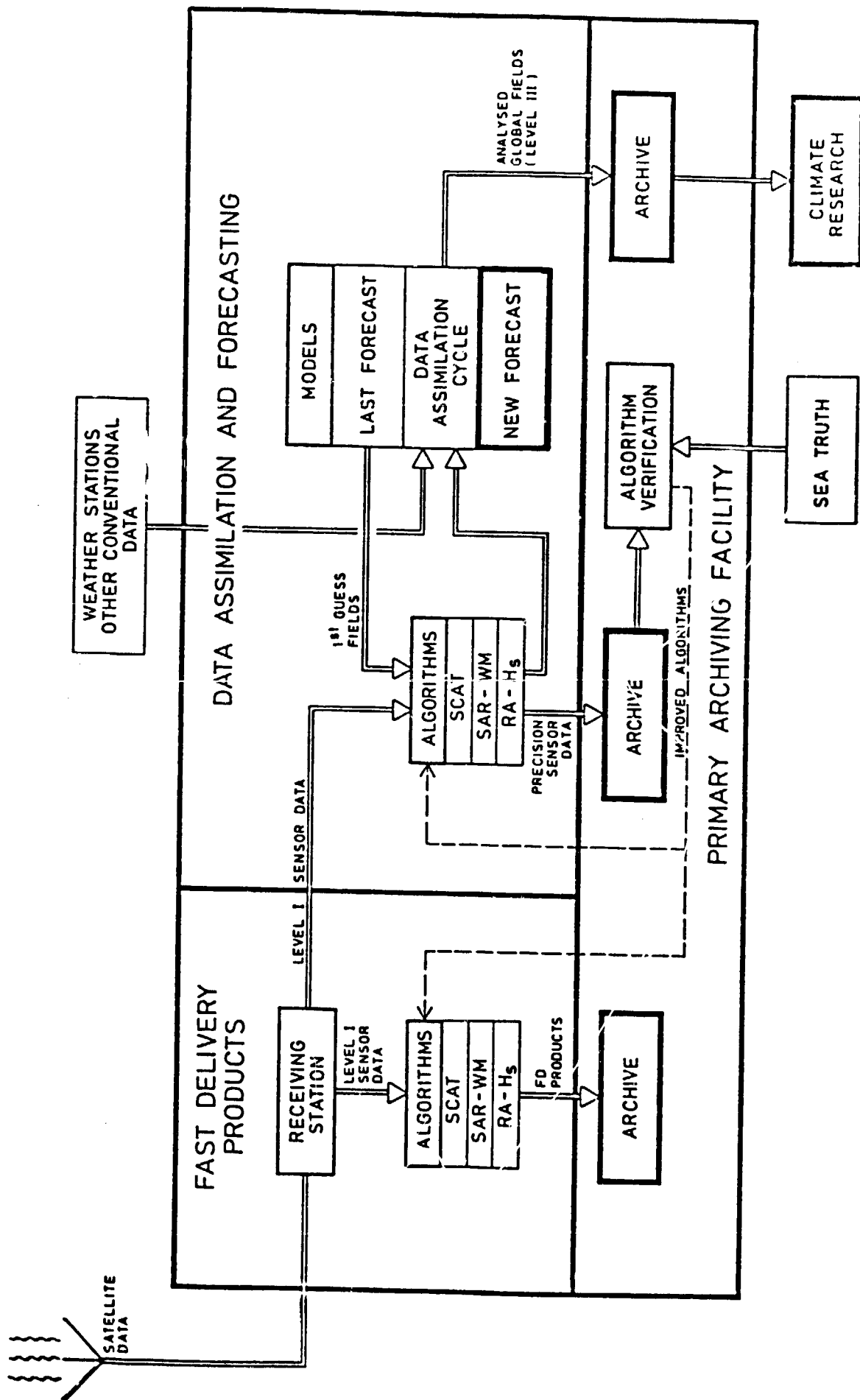
145

Fig. 1: General structure of wind and wave data assimilation system including ocean satellite data (from Hasselmann, 1935).

146

A quasi real-time, operational data assimilation system offers a number of advantages:

–   The system can provide sophisticated continuous data quality control, with the possibility of immediate feedback to operational centres of satellites or other data collection systems if data errors are detected. Experience ɔws that a comprehensive data assimilation system encompassing a diverse data set is significantly more effective in detecting subtle errors in individual system components than quick-look testing of separate sub-systems

–   The system can provide continuous statistical evaluation of the performance of satellite sensor algorithms, again offering a rapid feedback if algorithm improvements are needed.

–   The assimilation system can be applied during measurement campaigns, e.g. in the initial calibration and validation phase of a satellite, yielding data which can be fed back in quasi real-time into the campaign operation. In this way it is possible to continually monitor the performance of the satellite or other measurement systems during the campaign.

–   More efficient satellite sensor algorithms can be developed which make use of first guess wind and wave fields provided by the models. This is particularly important if the cross coupling of different sensor signals (e.g wind and waves) is to be properly incorporated in the algorithms.

–   Since the analysis system is designed to cope with the complete data flux in quac real-time, it must process the data at least at the same rate as it is produced. This avoids one of the recurrent problems of off-line processing systems: a continuously increasing processing delay, or, as the only alternative, the restriction of the data analysis to limited time periods.

Although a quasi real-time data assimilation system clearly has considerable advantages, a basic shortcoming of an operational system is that the homogeneity of the data set is endangered through

147

inevitable changes in the analysis procedure as improved assimilation systems and sensor algorithms are developed. For applications in which data homogeneity is essential, it may therefore be desirable to reanalyze the entire past data set with the latest assimilation system. Thus, although the major thrust of the GDAP is directed to an operational system, the option of a later re-analysis should be kept open. This requires the establishment of efficient archiving and retrieval mechanisms for all input data. A re-analysis would clearly be a costly undertaking, but this may appear less forbidding when more powerful computers become available later in the programme.

The programme required to develop and implement a comprehensive air-sea flux data assimilation system is extensive and can be carried through successfully only with wide international collaboration. For this reason it is proposed that efforts should be concentrated on the implementation of assimilation systems at the two major global forecasting centres supported by larger scientific communities, namely the European Centre for Medium Range Weather Forecasts (ECMWF) and the US National Meteorological Center (NMC). However, efforts by individual nations to develop similar systems at their national weather centres should also be encouraged, since the intercomparison of different products from several centres will provide a broader base for assessing the reliability of the methods.

## 1.2   In situ data

The second task of the Working Group is to recommend and initiate measures to improve the data base of in situ reference measurements which are needed for the validation of flux estimates inferred from satellite data or derived from global meteorological analysis. The Working Group considers that implementation of improvements in the quality, and efficiency of utilization, of existing measurement programmes would significantly upgrade the available data base. However, where there are potential deficiencies these must be identified and, where necessary, the initiation of new scientific field programmes to produce in situ reference measurements should be encouraged.

The operational in situ systems, which include moored and drifting buoys, the Voluntary Observing Ships (VOS), and island and land meteorological stations, are the responsibility of the World Weather Watch (WWW) of WMO. Recognizing that it is of primary importance that the in situ observational systems required for initialization of the atmospheric GCMs be continued, and where possible, improved, the Working Group strongly supports actions aimed at fulfilling the WCRP requirements for WWW systems as defined in the First WCRP Implementation Plan (WMO, 1985).

A specific Working Group project, described in Section 4.12, will identify data from previous scientific field programmes suitable for use in verifying the model derived surface fields. The project will also assess the quality of available in situ data, and determine any additional quality control procedures which may be required. The results will enable the Working Group to assess the need for further research field experiments, and the degree to which, with improvements, the existing operational in situ data can be used for verification purposes.

## References

Hasselmann, K., 1985: Assimilation of microwave data in atmospheric and wave models. Proceedings of a Conference on the Use of Satellite Data in Climate Models. Alpbach, Austria, June 10 - 12, 1985. ESA SP-244, Sept. 1985

WMO, 1985  First Implementation Plan for the World Climate Research Programme, WCRP Publication Series, N° 5, 123 pp.

3.  Overview of Work Plan

    The work plan of the GDAP may be divided into two stages:

    –   a preparatory phase, from 1988 until 1990, and

    –   a full implementation phase, from 1991 onwards.

3.1  Preparatory phase, 1988 - 1990

    During this phase a series of investigations need to be carried out on
    methods of assimilating data from different sources, addressing in
    particular the new forms of data which will become available from
    oceanographic satellites. Methods of assimilating single level data (i e
    surface data) will require special attention. Other questions which
    need to be addressed include the dependence of the numerical
    satellite sensor algorithms on the assimilation scheme, the incorpo-
    ration of the algorithms within the assimilation system itself and the
    interdependence of wind and wave data in both the sensor algorithms
    and the assimilation scheme.

    Alternative flux parameterisations need to be tested with regard to
    their impact on oceanographic models (tropical and global ocean
    circulation models and surface wave models). The appropriate
    numerical experiments will be carried out in collaboration with the
    WOCE and TOGA Numerical Experimentation Groups and the Wave
    Modelling Group (WAM).

    In preparation for a possible later reanalysis project (see Section 4.13),
    investigations will also need to be carried out on different methods of
    reconstructing improved surface flux fields from past data, including
    techniques which do not necessarily require the full data assimilation
    cycle.

    In addition, work will continue on a number of projects initiated
    before the begin of the preparatory phase of the present programme.
    These include:

- An ECMWF project requested by the TOGA Scientific Steering Group to compute all air-sea flux fields beginning 01.01.1985, applying the present data analysis schemes of ECMWF to the Centre's archived data set (see also Section 2.2 and Appendix III).

- A joint WAM-ECMWF project for the development and testing of an ocean satellite data assimilation and quality control system using SEASAT altimeter, scatterometer and SAR data in conjunction with conventional meteorological data.

## 3.2 Full implementation phase, 1991 onwards

At the end of the preparatory phase, continuous, operational data assimilation systems should be implemented at ECMWF, NMC and possibly other centres. The assimilation schemes should provide 6-hourly flux fields at the resolution of the then operational global forecast models ($\sim 1° \times 1°$). The assimilation scheme should encompass all relevant oceanographic microwave sensor data, including both wind and wave information, and should also include the ocean satellite sensor algorithms. The full operational phase will be preceded by a test phase which could coincide with the calibration/validation phase of ERS-1.

Table 1: Time Table for Global Data Assimilation Programme
for Air/Sea Fluxes
-----------------------------------------------------------------

| | | Preparatory Phase | | | Full Implementation Phase | | |
|------|------------------------------------|------|------|------|------|------|------|
| no. | project | 1988 | 1989 | 1990 | 1991 | 1992 | 1993 |
| 4.1 | data archival | | minor modification of data sets archival specifications: definition of wave data subsets | | Operational implementation | | |
| 4.2 | Scatterometer data | Development of algorithm suitable for data assimilation, incorporation of algorithm in assimilation system | | | Operational implementation | | |
| | | | Test of system against SEASAT and synthetic data | | | | |
| 4.3 | Coupled wind and wave sensor algorithms | Development of coupled algorithms for scatterometer, SAR and altimeter | | | Operational implementation, improvement of algorithms | | |
| | | | Test against SEASAT data | | | | |

| 4.4 Wave data assimilation | Development of methods for assimilating SAR altimeter and buoy wave data in wave models | Operational implementation |
|---|---|---|
| | Test of techniques using SEASAT data | |
| | Pre-operational test in global wave model | |
| 4.5 Quality control for new .ocean satellite and sur-face data | Development of techniques | Operational implementation |
| | Test against SEASAT and existing sur-face data | |
| 4.6 Imple-menta-tion of wave dependent flux parameteri-zations (in particular surface stress and energy flux) | Pre-operational implementation | △1 Operational imple-mentation of agreed upon parameteriza-tion |
| 4.7 Improve sensible and latent heat and fresh water flux parameterisations (atmospheric model experiments) | Test alternative flux parameterisations (WGNE project and (operational diagnostic) (see also project 3.9) | △2 Operational imple-mentation of agreed upon flux parameter-izations for sensible and latent heat and fresh water flux. |

| 4.8 Assessment of operational model radiation flux computations | Comparison with results of JSC radiation flux group | △3 | Operational implementation of agreed upon radiation flux parameterisation |
|---|---|---|---|
| 4.9 Assessment of air-sea fluxes in ocean circulation experiments | Numerical model experiments to contribute to (1), (2) and (3) (TOGA and WOCE-NEGs) | | Further numerical experiments for general TOGA and WOCE objectives (indirect quality control) |
| 4.10 Assessment of stress parameterisation in global wave models | Quasi-operational quality control as contribution to (1) | | Continual operational quality control |
| 4.11 Computation of SST | Improvement of SST computations using improved satellite sensor algorithms and ocean model data assimilation techniques | △4 | Operational implementation of recommendation SST analysis method |
| 4.12 In situ data | Upgrading of in situ data collection system | △5 | Implementation of upgraded in situ data system |
| 4.13 Reanalysis project | Assessment of homogeneity of operational flux computations | | |
| | 6a | | 6b |

△ : Decision points

---

Recommended procedures to be used in operational implementation phase:

△1 Momentum (stress) and (mixing) energy flux

154

△2 Sensible heat, latent and fresh water flux

△3 Solar and infra-red radiation

△4 SST computations

△5 in situ data collection and quality control system

△6a . △6b  Possible begin of flux reanalysis projects (start of project and period of past data to be analysed to be decided later depending on experience with real-time operational system).

REPORT No. 1
January 1987

A flux correction method for removing the climate drift of coupled atmosphere-ocean models.
Robert Sausen, Knut Barthel, Klaus Hasselmann

REPORT No. 2
January 1987

A coupled one-dimensional sea ice-ocean model.
Peter Lemke

REPORT No. 3
January 1987

Recurrence analysis of climate sensitivity experiments
Hans von Storch, Francis W. Zwiers

REPORT No. 4
January 1987

The Southern Oscillation: Sensitivity to SST anomalies in the region of the South Pacific convergence zone.
Hans von Storch, Harry van Loon, George N. Kiladis

REPORT No. 5
July 1987

PIPs and POPs - A general formalism for the reduction of dynamical systems in terms of Principal Interaction Patterns and Principal Oscillation Patterns.
Klaus Hasselmann

REPORT No. 6
April 1987

The response of a coupled ocean-atmosphere general circulation model to wind bursts
Mojib Latif, Joachim Biercamp, Hans von Storch

REPORT No. 7
August 1987

Principal Oscillation Pattern analysis of the 30-60 day oscillation in a GCM equatorial troposphere.
Hans von Storch, Thomas Bruns, Irene Fischer-Bruns, Klaus Hasselmann

REPORT No. 8
April 1987

A statistical comparison with observations of control and El Niño simulations using the NCAR CCM.
Hans von Storch

REPORT No. 9
August 1987

The WAM Wave Model System.
Susanne Hasselmann

Development of a Satellite SAR Image Spectra and
Altimeter Wave Height Data Assimilation System for
ERS-1.

Klaus Hasselmann, Susanne Hasselmann, Eva Bauer,
Claus Brüning, Susanne Lehner, Hans Graber, Piero Lionello